SENSORS FOR ULTRASONIC BONDING PROCESS CONTROL

SUBMITTED BY

CHIU SIU SAN

FOR THE DEGREE OF MASTER OF PHILOSOPHY IN APPLIED PHYSICS

AT

THE HONG KONG POLYTECHNIC UNIVERSITY

IN

2000

Abstract

The main objective of this project is to develop a sensor system that can be used to monitor important parameters in ultrasonic wire bonding, namely, ultrasonic amplitude, impact force and bonding time. These parameters can be used to distinguish the bond quality and to provide real-time feedback signals for in-process control.

Chapter one gives background information relating to ultrasonic wire bonding and highlights the importance of measuring different bonding parameters. Chapter two presents a review of the working principle and describes the characteristics of ultrasonic wedge transducer used in the present study. Chapter three describes an innovative way of placing a polyvinylidene fluoride (PVDF) polymer sensor between the piezoelectric driver and the concentrator horn. Different electrode patterns are evaluated for use in detecting the ultrasonic amplitude and the impact force. The most suitable electrode configuration is being evaluated further in Chapter four. Chapter five describes how the sensor is calibrated and Chapter six relates the bond quality to the sensor output. A short conclusion and suggestions for future work are given in Chapter seven.

The placement and calibration of sensor for bond quality monitoring described in this thesis is an original work with practical application that has not been reported before. We have filed a United State Patent based on the present work.

Acknowledgements

First and foremost I would like to express my sincerest thanks to my chief supervisor Prof. Helen L. W. Chan, whose gave me advice and guidance that made this study possible.

Moreover, my special thanks to Dr. Peter C. K. Liu, the Technical Director of ASM, for setting up this Teaching Company Scheme which gave me this golden opportunity to broaden my knowledge.

I also would like to thank Dr. Y. M. Cheung and Mr. C. W. Yuen, my current and former project supervisors from ASM Assembly Automation Ltd, who helped me a great deal in this project.

I owe particular thanks to each of the following people in the Department of Applied Physics at the Hong Kong Polytechnic University: Dr. Bernd Ploss, Dr. Beatrix Ploss, Prof. F. G. Shin, Mr. S. W. Or and Dr. K. W. Kwok. I thank them for giving me their invaluable suggestions, advice and comments.

I also would like to thank the QC department of ASM, who have taught me the bond quality testings. To people in ASM and in the Applied Physics Department who have given me their help, I thank them.

I gratefully acknowledge the financial support from ASM Assembly Automation Ltd. and the Industrial Department of the Hong Kong Government. Finally, I would like to thank my family for their understanding and patience during these years.

Table of Contents

Chapter 2 Characteristics of an ultrasonic wedge transducer for wire bonding

Chapter 3 Selection of sensor material and its location

Chapter 4 Analysis of sensor signals

List of Figures

Chapter 1

Introduction

1.1 Background

Wire bonding packaging has a wide application in microelectronics industry. There are three commonly used wire bonding methods, namely, thermocompression, ultrasonic, and thermosonic. Ultrasonic wedge bonding was introduced to the microelectronics industry at about 1960 and became dominant in device production until gold-ball thermosonic autobonders took over. Ultrasonic wedge bonding is performed at room temperature (if heated, it is thermosonic). It is primarily used to bond Al wire to either gold (Au) or aluminum (Al) bond pads. It is called gold wire bonding when gold wire is used [1].

In general, aluminum wire for ultrasonic wedge bonding normally has 1% silicon added to increase its strength because pure aluminum is too soft to be drawn to fine-wire dimensions. For example, 31.75 μm (1.25 mil) diameter aluminum wire added with 1% silicon has 1 to 4 % elongation and 19 to 21 gf tensile strength. Figs. 1.1 and 1.2 show typical aluminum ultrasonic wedge bonds on 100×100 μm^2 aluminum bonding pads for Al - Al first bond on the IC chip and thick gold plated bonding pads for Al – Au second bond on the chip carrier.

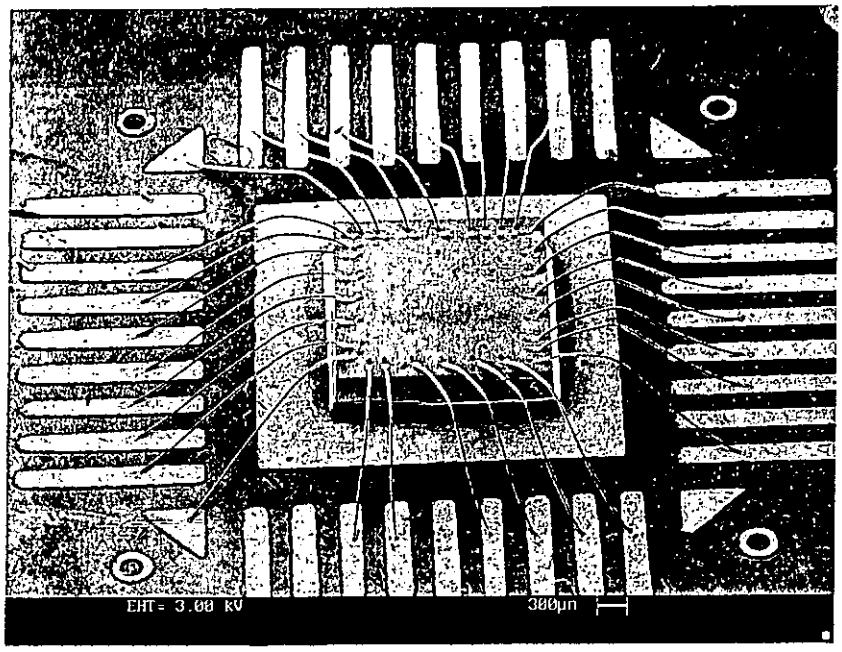

Fig. 1.1 A plane view of typical wire bonds to interconnect the IC die and the chip carrier.

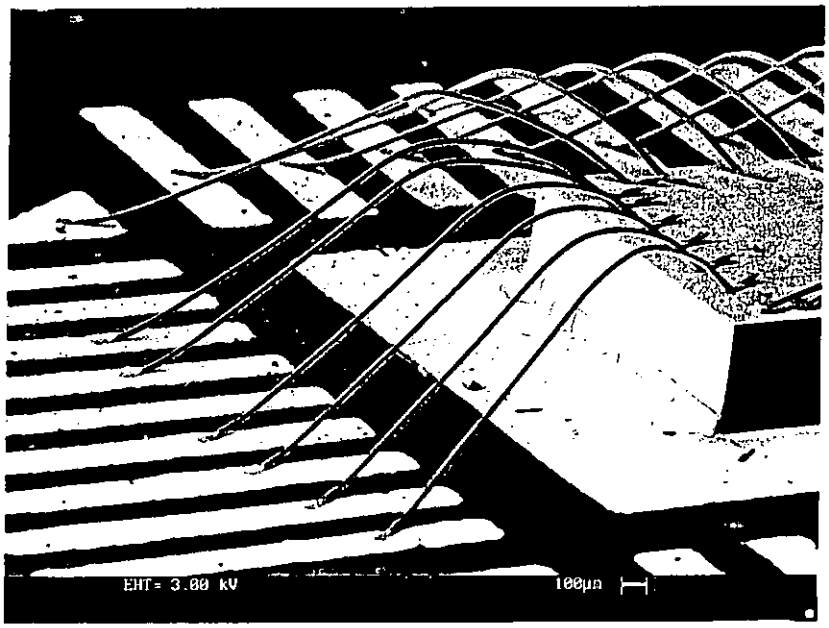

Fig. 1.2 A side view of typical aluminum wire wedge bonds.

1.2 Wire bonder

An AB-500B computerized semi-automation ultrasonic wire wedge bonder (fig. 1.3) manufactured by ASM Assembly Automation Ltd. is used in the present project.

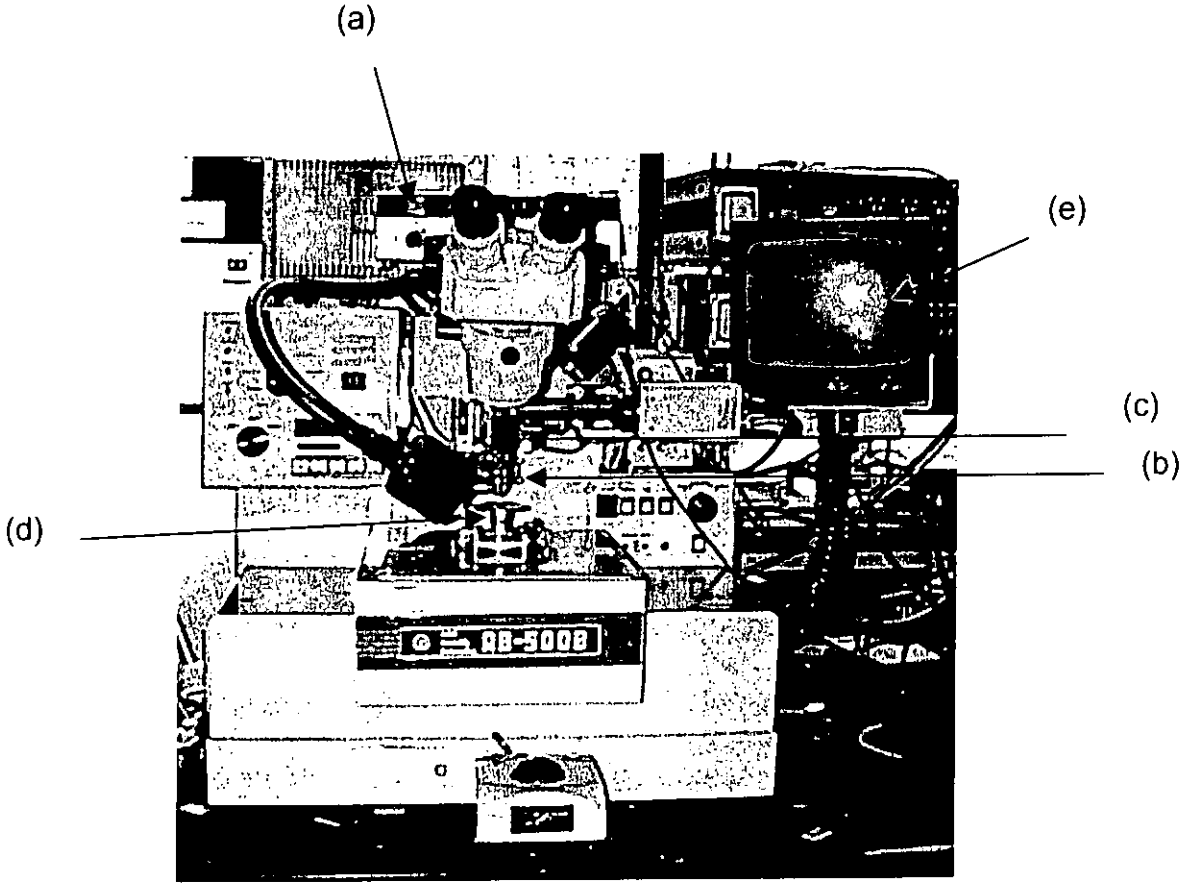

Fig. 1.3 The ASM 500B computerized semi-automatic ultrasonic wedge bonder. (a) the PLL ultrasonic generator; (b) the Uthe 70-PTL Al wedge bond ultrasonic transducer; (c) the bond head; (d) the workholder and (e) the vision system.

The bonding machine comprises three major components: bonder assembly, controller system and the vision system [2].

Bonder assembly includes the following components:

(a) A phase-locked-loop (PLL) ultrasonic generator supplies the ultrasonic power to the ultrasonic transducer and keeps the system close to its resonant operational frequency for stabilization.

(b) An ultrasonic transducer (fig. 1.4) converts electrical energy into mechanical vibration. It essentially includes a piezoelectric driver, a transducer horn, a bonding tool and a barrel. Ultrasonic power is fed into the piezoelectric driver, to drive the transducer horn and set the bonding tool into vibration in longitudinal modes. The transducer horn has an exponential shape and it amplifies the longitudinal vibrations and transmits vibrations to the bonding tool. At the bonding tool, longitudinal vibration of the horn is converted into flexural mode vibrations. The Uthe 70-PTL Al wedge bond ultrasonic transducer has two small holes drilled at angles of 60° and 30° in the transducer horn for threading the Al wire (fig. 1.4). The nominal operation frequency of the transducer is 62.1-63 kHz. Gaiser Tool model 2130-2025-L bonding tool made of tungsten carbide is clamped into the front of transducer horn by a small screw. The barrel of the ultrasonic transducer is used to mount the transducer to the bonder.

(c) A bond head consists of a transducer mounting bracket that fixes the ultrasonic transducer by clamping at the barrel. It can descend vertically in the z direction until the bonding tool with a wire touches the bonding surface to produce a predetermined bonding force.

(d) A work holder can be programmed to move in the x-y direction with precision and has clamps to hold the device to be bonded.

(e) A vision system is used to visualize the bonding process. The illumination light generated by a lamp passes through the lens system to the camera and finally the object image is displayed on a TV monitor.

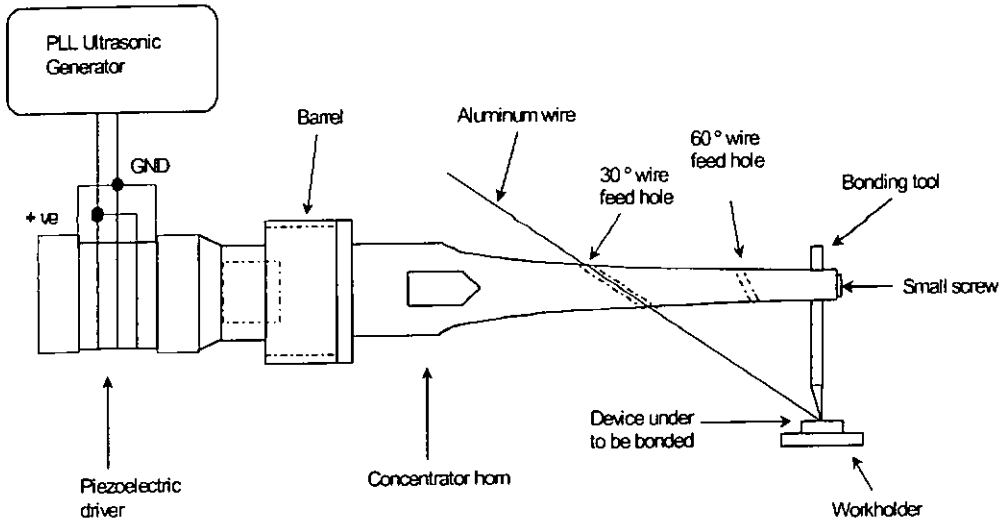

Fig. 1.4 Diagram of the Uthe 70-PTL Al wire wedge bond ultrasonic transducer.

1.3 Wedge bonding process

The following figures shows the simplified step-by-step procedure for making an ultrasonic wire bonding between the bond pad of a chip and the package with a typical wedge tool.

A wedge tool with a bonding wire (Al- 1% Si, 31.75 μm diameter) is placed above the bond pad. The tool is lowered to its 'first-search' position, presses the bonding wire against the bond pad with a predetermined force. By applying an ultrasonic energy, the wedge vibrates along the wire. After a short time, the wire begins to deform and a first bond is formed on the bond pad. The wire clamp is opened and the bonding tool raises while the wire is fed out from the spool of wire for forming a loop between the first and the second bond.

The work holder moves to the location of the second bond and a wire loop is formed. The tool is lowered to the 'second-search' position and exerts a force. Ultrasonic energy is applied again to form the second bond on the package. After the second bond has been made, the wire clamp is closed and pulls back on the wire to break it at the heel of the bond. Then, the wedge tool is raised again; the end of the wire is pushed forward underneath the tool until its tip is placed beyond the front of the tool. The bonding machine is then ready to repeat the cycle [3].

Microscopically, there are three phases in the ultrasonic wire bonding [3,4].

(1) Cleaning phase - In this short first phase, hardly any wire deformation occurs and the temperature of the bond pad surface rises only slowly. Throughout this phase, the bonding tool rubs the wire across the bond pad surface. The ultrasonic energy being applied is used mainly for surface cleaning, i.e. for removal of the surface oxide and contamination layers. Some ultrasonic energy is consumed in heating. There is only relatively small amount of ultrasonic energy being used for wire deformation.

(2) Mixing phase – In the second phase, the temperature rises sharply and the wire deforms accordingly. Input ultrasonic power is used to flatten the metal wire and to cause a distinct temperature rise in the bond pad surface. The metals are brought together until they are only atomic lattice distance apart over the interface area. The elevated temperature enhances the diffusion of atomic lattice dislocations and relaxes the weld area. A partial weld is formed and the wire sticks to the bond pad. The bonding tool now rubs onto the essentially immobile wire, thereby generating a further increase in temperature.

(3) Diffusion phase - No significant deformation or increase in temperature occurs in the third stage. The heat generated by the friction of the bonding tool on the surface of the wire causes the temperature of the bond area to rise, thereby increasing the relaxation of the weld area. This tempering process stabilizes the bond by 'curing' the diffusion – rich interface area and preventing it from becoming brittle.

Every bond will go through the three phases described above, although the length of each phase can vary for a number of reasons. For example, the wire composition is not homogeneous, the surface properties of the bond pad and wire and the contamination level may vary. In an ideal situation, as soon as the deformation curve levels off, the energy supplied can be reduced and removed altogether shortly afterwards. However, on most bonding machines a very high maximum energy level is programmed to ensure that all bonds are made. This method has a risk that a large number of bonds receive too much energy and thus being 'overbonded', resulting in a significant quality loss.

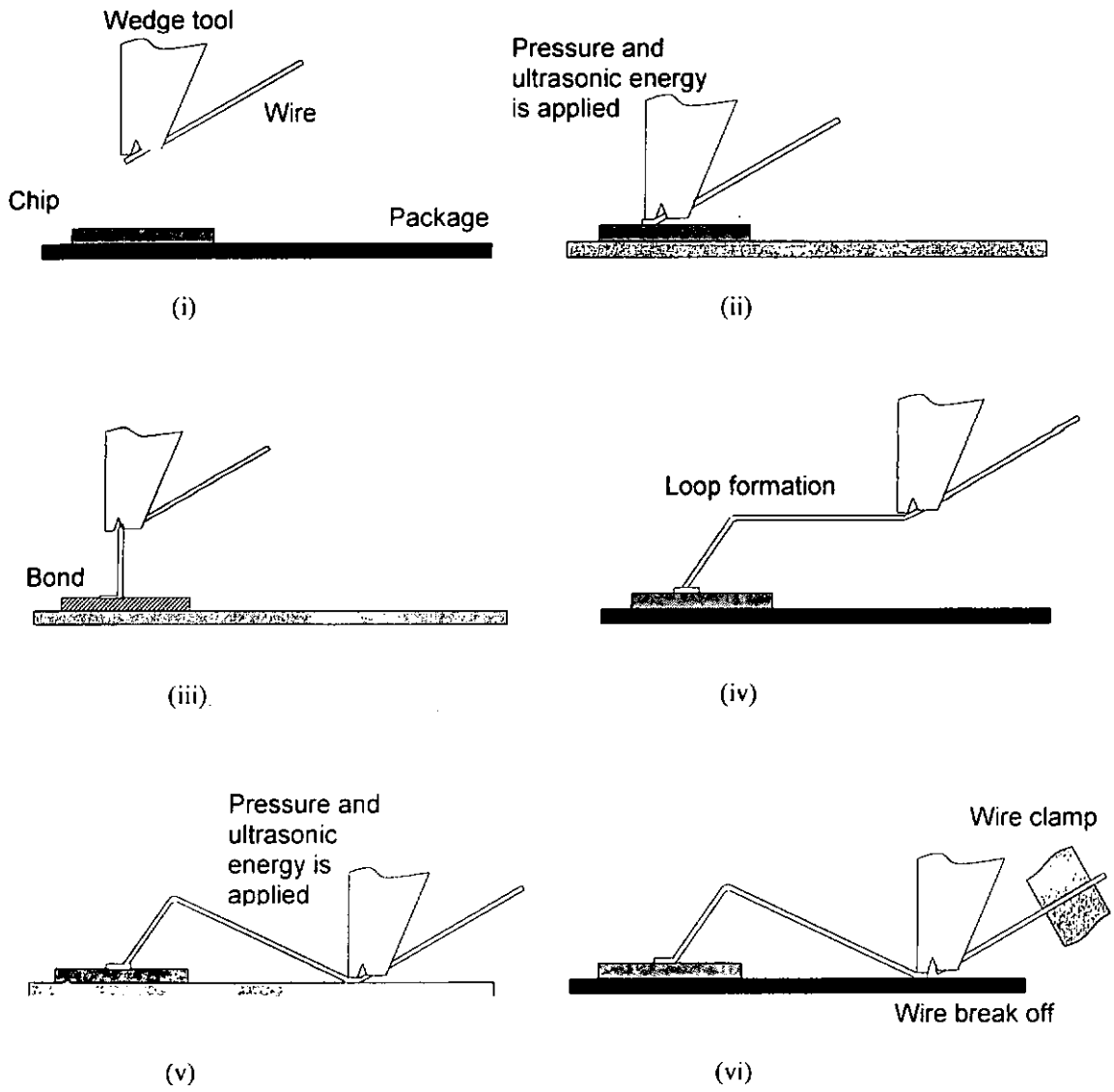

Fig.1.5 Simplified step-by-step procedure of the wedge bonding machine operation [5].

1.4 How ultrasonic bonds are formed

Soft, face-centered-cubic (FCC) metal wires (e.g. Al, Au, Cu) of 25 – 33 μm diameter are commonly used in small ultrasonic welds for microelectronic interconnections. There is no mathematical model for the welding process. It is a complex and yet not fully understood process. However, many efforts have been made to study and/or explain the process.

Ultrasonic Al (31.25 μm diameter) wedge bond formation was studied by examining the bond foot prints left on normal Al bond pads by bonds that did not stick. These are the bond lift-off patterns and represent the best method for studying the early stages of bond formation. Such patterns are made by increasing ultrasonic power and with constant bonding force (25 gf) and bonding time (30 ms).

The pattern in fig. 1.6a results from pressing the wire against the pad with normal bonding parameters except with an ultrasonic power setting of 0.5 $V_{p\text{-}p}$. Fig. 1.6b shows the lift-off pattern made by applying a driving voltage of 1.5 $V_{p\text{-}p}$ indicating that wire-to-pad microwelds start to form at points near the perimeter. In the lift-off pattern in fig. 1.6c resulted from a driving voltage of 2.5 $V_{p\text{-}p}$, the weld area spreads inward covering part of the area around the perimeter. Fig. 1.6d shows the bond formation when the driving

voltage is 3 V_{p-p}. The weld has increased considerably, but is still primarily confined to the area around the perimeter. As the driving voltage is increased to 3.5 V_{p-p} (fig. 1.6e), the ultrasonic wedge bonding starts around the perimeter and has progressed inward to form an optimum bonding.

Ultrasonic welding is a type of deformation weld in which the metal is first softened by the ultrasonic energy. The bonding force deforms the softened wire against the equivalently softened bonding pad, sweeping aside brittle surface oxides and contaminants, leaving clean surfaces in contact. Little deformation takes place in the center of the weld, so the oxides and contaminants remain there, and this area is often remained unwelded. Presumably, the same energy transfer mechanism that softens the metals without significant heat generation also supplies the required activation energy for interdiffusion. This forms the metal-to-metal (atomic) bonds within a few milliseconds [3].

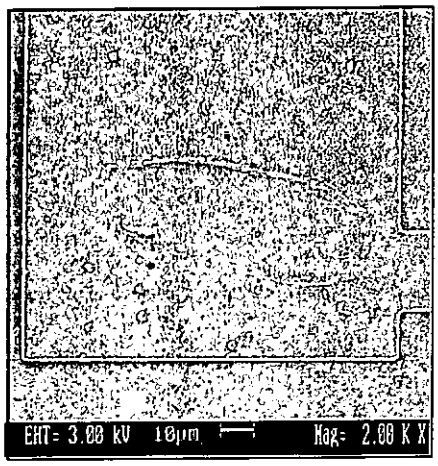

(a)

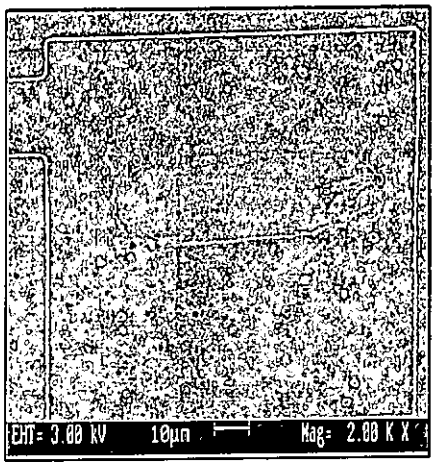

(b)

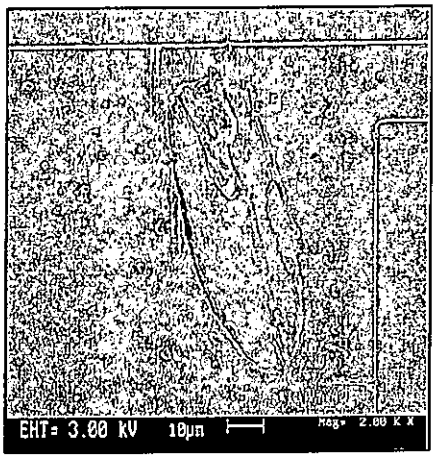

(c)

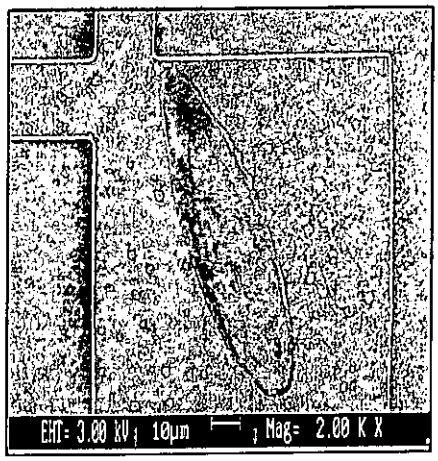

(d)

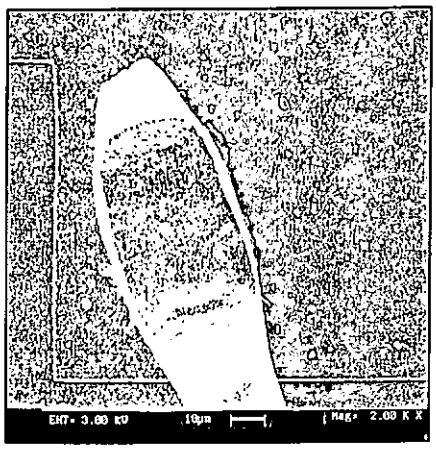

(e)

Fig. 1.6 Wedge lift-off patterns below the point that the wire adhere. Patterns are made by maintaining the (25 gf) bonding force and (30 ms) bonding time constant and progressively increasing the

ultrasonic power (the optimized driving voltage is 3.5 V_{p-p}). (a) 0.5 V_{p-p} driving voltage; (b) 1.5 V_{p-p} driving voltage; (c) 2.5 V_{p-p} driving voltage; (d) 3 V_{p-p} driving voltage and (e) 3.5 V_{p-p} driving voltage.

1.5 Real-time monitoring

In recent years, there has been considerable interest for an electrical or a mechanical real-time (in-process) quality control system in order to increase the bond yield. As there is no quantitative theory for ultrasonic bonding, the proper operating window to produce good quality bondings are determined empirically.

In general, two broad categories of measurement parameters have been considered in the development of an in-process monitoring and/or control technique. They are direct parameters of the bond itself or secondary parameters that will vary according to the extent of bond formation [6].

Direct bonding parameter measurements involve finding the transient temperature at the bonding interface, acoustic emission measurement etc. However, such kind of measurements have their limitations for developing in-process monitor or control systems. For example, an ideal acoustic emission technique [6] relies on the detection of significant emission signal during the change from interfacial sliding to plastic deformation conditions, or the signal changes as a result of stressing a completed bond during the final phase of the bonding period. In practice, acoustic emission signal amplitudes are small compared with signals of similar frequency arising from harmonics of the fundamental bonding frequency. Highly

sophisticated transient analysis techniques would be required to detect the acoustic emission signals.

Secondary bond parameters involve the measurements of progressive changes in mechanical impedance at the weld interface as the bond is developed. These measurements can conveniently be grouped according to the locations of the control parameters relative to the bonding zone. These are sometime called transmitted parameters, weld zone parameters and reflected parameters [3,6].

Transmitted parameters represent physical properties detected after the ultrasonic vibrations have passed into the substrate supporting structure, and they are modified as a result of changes in the bonding zone impedance. Weld zone parameters denote the wire deformation can be used to characterise bond quality, as evidenced by visual inspections of the wire bonds and compared them against certain assessment standards [7,8]. Changes in mechanical impedance at the bonding interface generally cause changes in the transducer driving system. Monitoring has been achieved by measuring the change in current flow in constant voltage systems and vice versa [9]. This methodology mainly measure the reflected parameters. Some of these methods have been published, others patented, and others have appeared only in internal or in military contract reports [9 -16].

1.6 Bonding parameters

There are some critical bonding parameters that influence the bond quality. They are the ultrasonic energy, bonding force and bonding time. Optimizing these parameters can improve the bond quality and the bondability.

1.6.1 Ultrasonic energy

Ultrasonic energy is produced by a piezoelectric driver. It plays an important role in the wire bonding process. Firstly, it removes the surface oxide and contamination layers to achieve surface cleaning. At the same time, the bonding wire is softened and deformed by the ultrasonic energy [3]. After the ultrasonic energy has been removed, the metals are left work-hardened, whereas equivalent thermal deformations leave the metal permanently softer (annealed).

To further increase the ultrasonic energy beyond the optimal condition, the probability of cratering will increase. This is because the metal mass flow is equal in all directions, stacking faults in Si occur perpendicular to the direction of the ultrasonic bonding tool motion (pulse direction). However, too low an ultrasonic energy does not result in a weld because there is not

enough energy for interdiffusion. Hence, finding an optimum ultrasonic energy necessary for a good wire bonding is necessary and important.

1.6.2 Bonding force

Bonding force can be divided into impact force and static force. Impact force occurs when a bonding tool hits the bonding pad. Static force is exerted to press the bonding tool against the bonding pad to ensure intimate contact between the wire and the bond pad. It deforms the softened wire against the softened bonding pad, sweeping aside brittle surface oxides and contaminants, leaving clean surfaces in contact.

In general, too high or too low a static bonding force can result in cratering. High bonding force implies that there is excessive interfacial scrubbings during some portion of the bonding cycle which results in cratering and poor bonding [3].

1.6.3 Bonding time

Bonding time indicates the duration of a burst of ultrasonic energy during which bonding is formed. In general, if the bonding time is decreased, increasing ultrasonic energy will be required to produce a reliable weld,

and the probability of cratering will increase. Hence, the optimal period of bonding time is related to the power of the ultrasonic energy [3].

1.7 Objectives of the thesis

The main objective of the present project is to install a piezoelectric sensor on the bonding transducer in order to detect the acoustic signals generated during the ultrasonic wire bonding. These signals can be separated into two parts: low frequency and high frequency signals. Low frequency signals represent the mechanical vibrations of the ultrasonic transducer. High frequency signals represent the ultrasonic energy produced by the piezoelectric driver of the ultrasonic transducer. Different electrode patterns of the sensors are also studied. Sensor with the most suitable electrode pattern is calibrated and the signals measured by the sensor will be used to monitor and differentiate the bond quality.

1.8 Motivation

In-process bond quality monitoring is an important technology for the microelectronics industry. There are considerable research studies about using different methodologies to achieve real-time bond quality monitoring. Some of these methods have been published and others patented [8-14]. Most of the papers and patents suggested that monitoring can be achieved by measuring an electrical parameter either from the ultrasonic power supply, or from the transducer's impedance, or from the amount of ultrasonic energy passing through the package, etc.

McBrearty *et al* [17,18] describes a successful missing wire detector for automatic bonding machines. The proposed method based on an in-process measurment of a bonding frequency shift which is characteristic of acceptable wire bonds.

J. L. Landes *et al* [19] describes a monitoring method for optimizing the ultrasonic bonding of materials by analyzing the impedance of the ultrasonic bonding transducer.

M. J. Hight et al [20] describes an apparatus for non-destructively monitoring the bonding quality of an ultrasonic bonding system by

comparing the vibration amplitude of the bonding tool in a freely vibrating (i.e. no load) condition and during the bonding operation.

K.Ulrich von Raben *et al* [21-23] and R.Pufall [24] described a method for monitoring the bonding parameters by using piezoelectric sensor to measure ultrasonic amplitude and by using piezoresistive sensor to monitor the bonding force.

In the literature, most research studies involve using two separate sensors for monitoring the bonding parameters. In this project, we try to use one piezoelectric sensor to measure the ultrasonic amplitude, impact force and bonding time and develop a new method for monitoring important bonding parameters that affect the bond quality.

Chapter 2

Characteristics of an ultrasonic wedge transducer for wire bonding

2.1 Introduction

The ultrasonic transducer is the heart of a wire-bonding machine. A quality, stable, well-designed transducer is essential for providing effective wire bondings. In this chapter, the characteristics of an ultrasonic transducer and the principles of ultrasonic wire bonding are described.

2.2 Electrical characteristic of an ultrasonic transducer for wire bonding

The experimental setup shown in fig. 2.1 was used to measure the electrical characteristic of the ultrasonic transducer. The transducer was suspended on two strings to enable it to vibrate freely. The transducer is quite sensitive to the clamping conditions. In order to reduce the noise of the transducer, the best method is using two strings to suspend the transducer. Then, the spectra of electrical impedance and phase angle as functions of frequency were measured by a HP 4194A impedance/gain

phase analyzer and results were recorded by a computer. To simulate the actual bonding condition, another measurement is carried out with the transducer clamped in the bracket.

The spectra in fig. 2.2 show the electrical impedance and phase angle as functions of frequency for a freely vibrating transducer from 50 kHz to 100 kHz. The strongest minimum electrical impedance was found at 63 kHz. Fig. 2.3 is the profile after the transducer was clamped in the bracket and the strongest minimum electrical impedance shifted slightly to 62.5 kHz which agreed with the acceptable range of 62.1 kHz to 63 kHz suggested by the supplier. It shows that clamping the transducer will lower the transducer resonance.

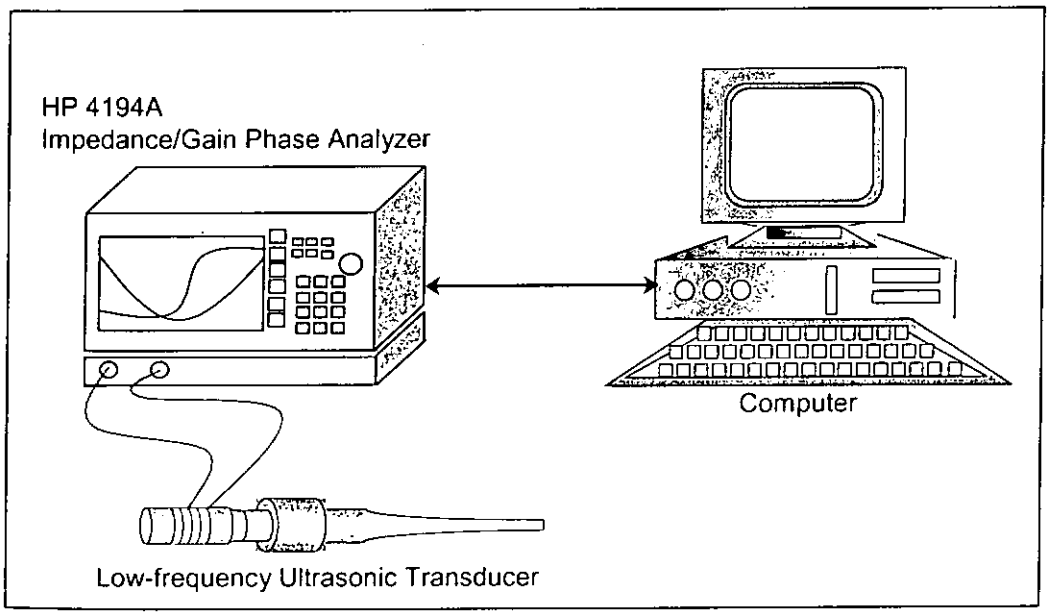

Fig. 2.1 The experimental setup for measuring electrical characteristic of the transducer.

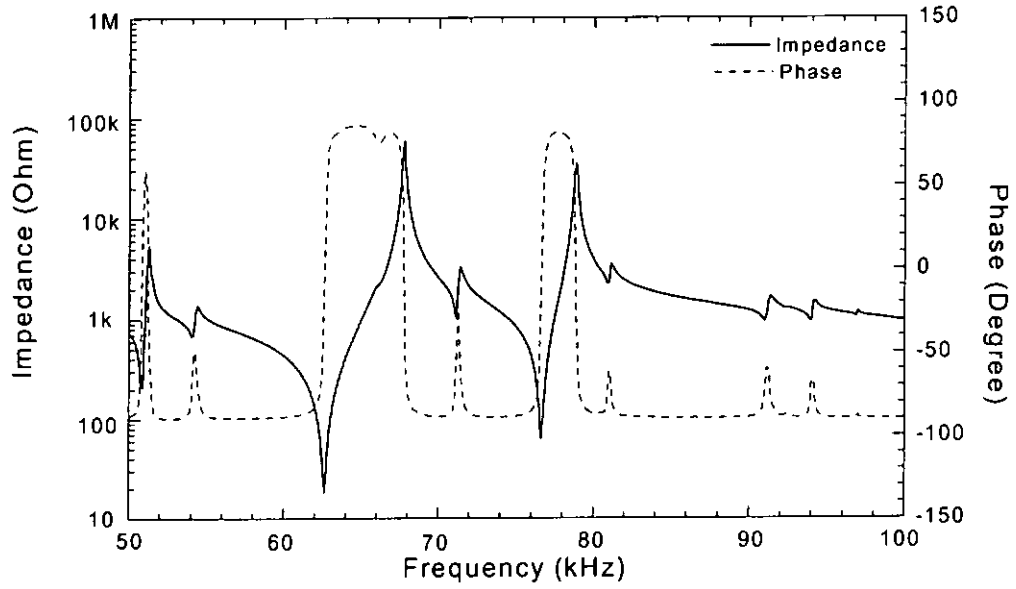

Fig. 2.2 The spectra of electrical impedance and phase angle against frequency of a freely vibrating ultrasonic transducer.

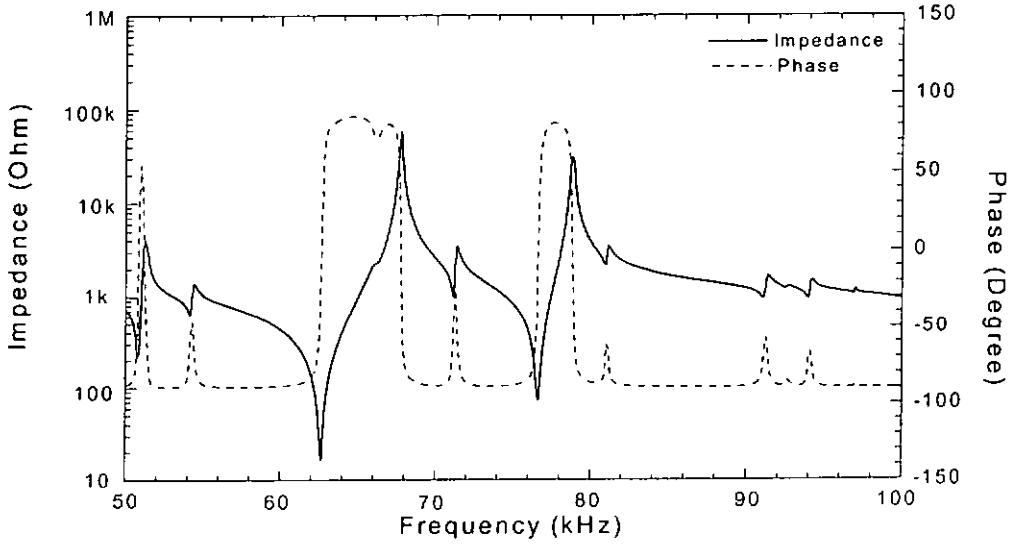

Fig. 2.3 The spectra of electrical impedance and phase angle as functions of frequency of a clamped ultrasonic transducer.

2.3 Principle of a wedge transducer

A 70-PTL Uthe ultrasonic wedge transducer (fig. 1.4) comprises a piezoelectric driver, a concentrator horn and a bonding tool which is secured by a screw. The individual parts can be discussed separately.

2.3.1 The piezoelectric driver

A piezoelectric driver provides a driving force to the ultrasonic transducer. It converts electrical energy into mechanical vibrations. The Langevin transducer [25,26] has a half-wave resonant length. Configuration of the piezoelectric driver includes two identical metal plates (stainless steel) with four piezoelectric ring elements (PZT) in between them and they are bolted together by a screw as shown in fig. 2.4. The piezoelectric rings are polarized in opposite directions and separated by electrodes (beryllium copper). The rings are connected electrically in parallel but mechanically in series. The coupling between the piezoelectric rings with the front metal section is achieved by mechanically prestressing the assembly in the axial direction by means of a bolt.

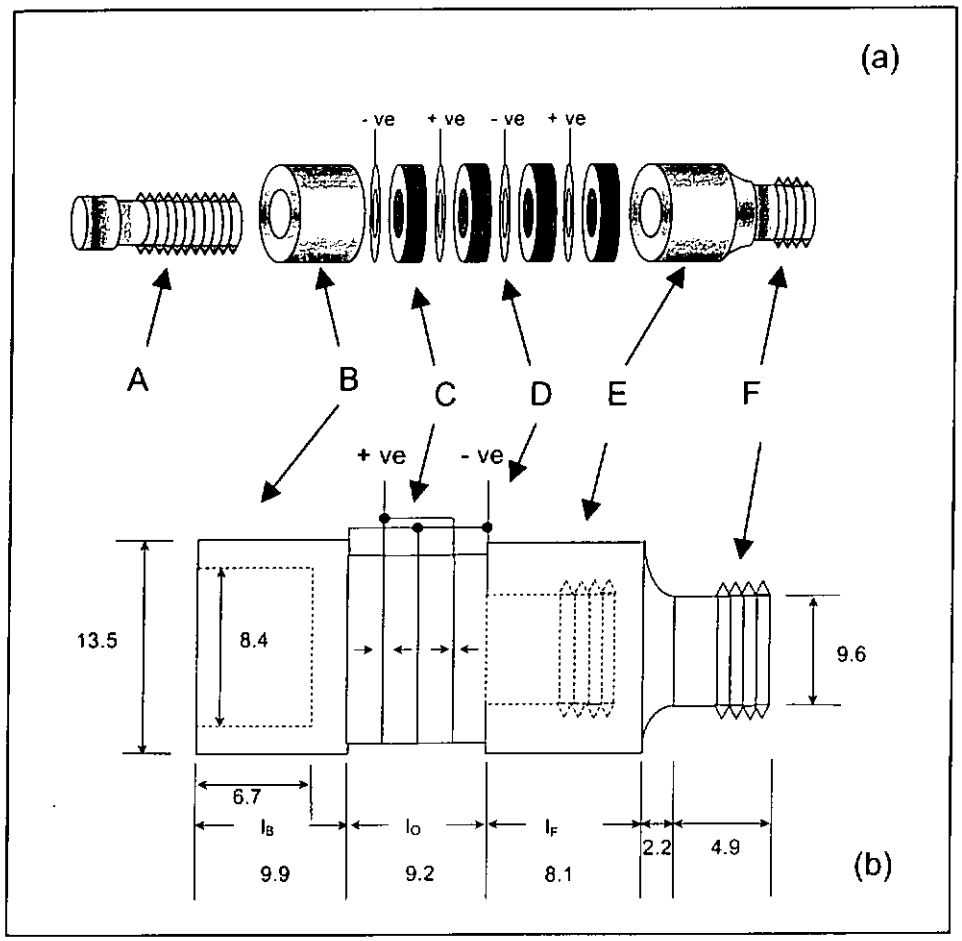

Fig. 2.4 The geometrical structure of a piezoelectric driver. (a) the solid body and (b) the layout of a piezoelectric driver. A represents the screw for pre-stressing; B represents the back metal plate (stainless steel); C represents the piezoelectric ceramic rings (PZT); D represents the electrode sheets (beryllium copper); E represents the front metal plate (stainless steel) and F represents the screw of the front metal plate.

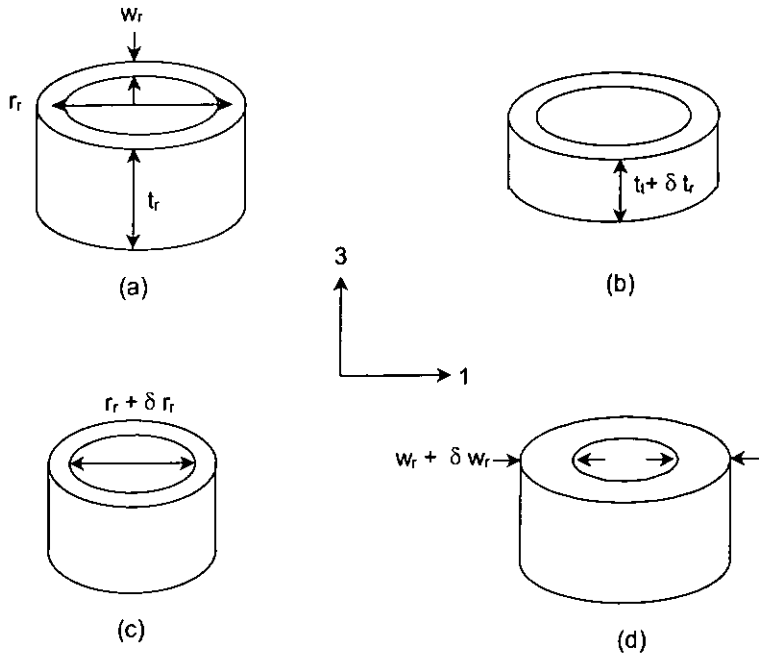

Fig. 2.5 Three possible fundamental vibration modes of a ceramic ring. (a) Undeformed ring; (b) thickness mode; (c) radial mode and (d) wall-thickness mode.

A piezoelectric ring has three possible fundamental modes of vibration [27] (fig. 2.5): a thickness mode that is determined by the ring thickness (t_r); a radial mode that is determined by the mean diameter of the ring (r_r) and a wall-thickness mode that is determined by the wall-thickness of the ring (w_r).

Thickness vibration mode in a poled ring results in a variation of its thickness, the ring becomes longer and shorter ($t_r \pm \delta t_r$). In a radial vibration mode, the ring becomes larger and smaller ($r_r \pm \delta r_r$). In a wall-thickness vibration mode, wall thickness of the ring becomes thicker and

thinner ($w_r \pm \delta w_r$). The resonance frequencies of the three vibration modes can be found from the following equations [28]:

Thickness mode $$f_t^I = \frac{1}{2t_r\sqrt{\rho_r s_{33}^D}} \quad (2.1)$$

Radial mode $$f_r^E = \frac{1}{\pi r_r\sqrt{\rho_r s_{11}^E}} \quad (2.2)$$

Wall-thickness mode $$f_w^E = \frac{1}{2w_r\sqrt{\rho_r s_{11}^E}} \quad (2.3)$$

where f_t^I is the fundamental thickness resonance frequency which is given by the lowest anti-resonant frequency of thickness mode; f_r^E and f_w^E are the fundamental radial and wall-thickness resonance frequencies which are given by the lowest (series) resonant frequencies of the radial and wall thickness modes, respectively. s_{33}^D is the piezoelectric elastic compliance at constant electric displacement in the thickness (3-) direction. s_{11}^E is the piezoelectric elastic compliance at constant electric field in the radial (1-) direction. ρ_r is the density of the ring. $r_r = (r_{outer}+r_{inner})/2$ is the mean diameter of the ring. r_{outer} and r_{inner} are the outer and inner diameters of the ring. $w_r = (r_{outer} - r_{inner})/2$ is the wall-thickness of the ring.

The spectra of electrical impedance and phase angle against frequency of the Uthe piezoelectric ring is shown in fig. 2.6. There are three resonant peaks at 130.8 kHz, 460.9 kHz and 881.3 kHz and three anti-resonant

peaks at 137.9 kHz, 498.9 kHz and 914.5 kHz. They represents the radial mode, wall-thickness mode and thickness mode, respectively.

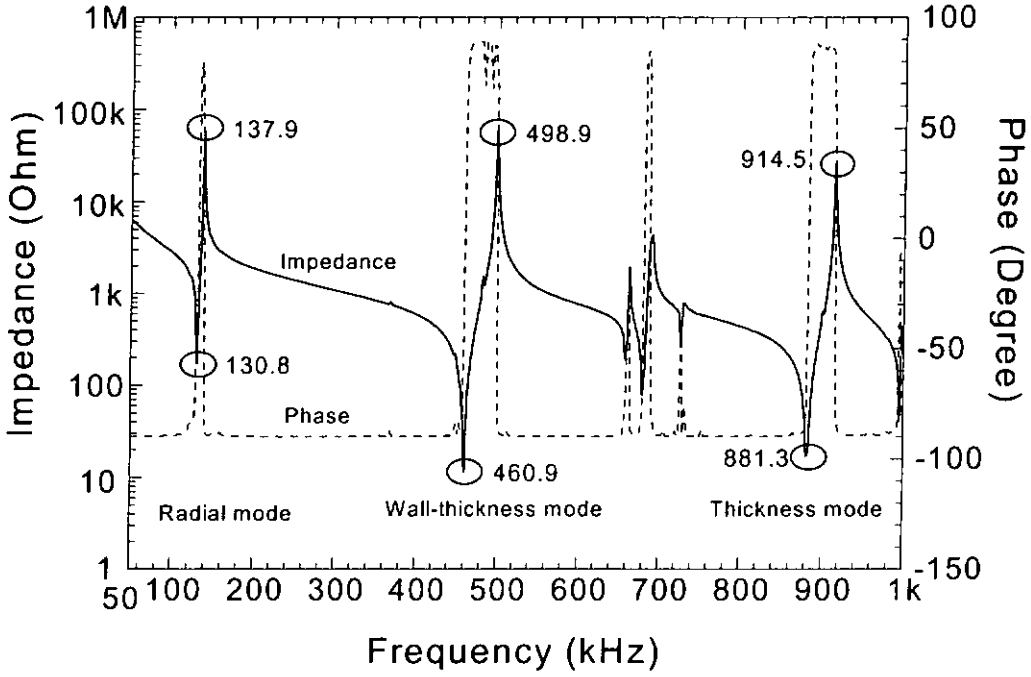

Fig. 2.6 The electrical impedance and phase angle against frequency of a typical Uthe PZT ring used in fabricating the piezoelectric driver. The dimensions of the ring are t_r=2.3 mm, r_r= 8.9 mm and w_r=3.9 mm.

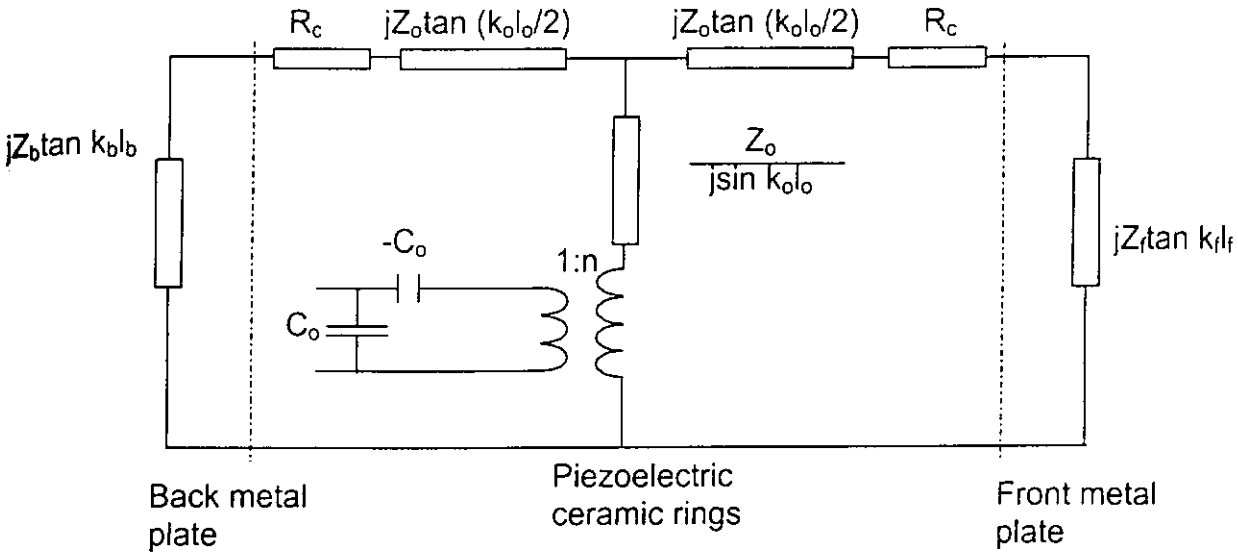

Fig. 2.7 The equivalent circuit of a piezoelectric driver [29-33]. Z_0, Z_b and Z_f are the impedance. k_b, k_f and k_o are the wave numbers. C_0 is the clamped capacitance. n is the transformation ratio. R_c is the contact loss.

The equivalent circuit of the piezoelectric driver is given in fig. 2.7 [29-33]. The T-circuit represents the PZT rings. The other two resistors represent the front and back metal plates, respectively. The electrode sheets, the screw of the plate and the pre-stressed screw are ignored in this circuit. The parameters in the figure are defined as follows:

$$Z_b=(\rho c)_b A_b \qquad (2.4)$$

$$Z_f=(\rho c)_f A_f \qquad (2.5)$$

$$Z_o=(\rho c)_o A_o \qquad (2.6)$$

$$k_b=\omega/c_b \qquad (2.7)$$

$k_f=\omega/c_f$ (2.8)

$k_o=\omega/c_o$ (2.9)

When the transducer is operated without a load, the mechanical impedance Z_m of the ultrasonic transducer can be represented by [29].

$$Z_m = R_m + jX_m \tag{2.10}$$

where R_m and X_m are the equivalent mechanical resistance and reactance.

$$R_m = -\frac{Z_0^2 R_c / \sin^2(k_0 l_0)}{R_c^2 + 4Z_0^2 \cot^2(k_0 l_0)} + \frac{2H(H^2 - W_1 W_2) + H(W_1 + W_2)^2}{4H^2 + (W_1 + W_2)^2} \tag{2.11}$$

$$X_m = -\frac{2Z_0^3 \cot(k_0 l_0)/\sin^2(k_0 l_0)}{R_c^2 + 4Z_0^2 \cot^2(k_0 l_0)} + \frac{(W_1 + W_2)(H^2 + W_1 W_2)}{4H^2 + (W_1 + W_2)^2} \tag{2.12}$$

$$W_1 = G + Z_b \tan(k_b l_b) \tag{2.13}$$

$$W_2 = G + Z_f \tan(k_f l_f) \tag{2.14}$$

$$H = R_c + \frac{2Z_0^2 R_c / \sin^2(k_0 l_0)}{R_c^2 + 4Z_0^2 \cot^2(k_0 l_0)} \tag{2.15}$$

$$G = Z_0 \tan(k_0 l_0 / 2) - \frac{Z_0[R_c^2 - 4Z_0^2 \cot(k_0 l_0)\tan(k_0 l_0 / 2)]/\sin(k_0 l_0)}{R_c^2 + 4Z_0^2 \cot^2(k_0 l_0)} \tag{2.16}$$

Where Z_0, Z_b and Z_f are the impedance, R_c is the contacting loss caused by bonding at interfaces,.ω is the angular frequency, k_b, k_f and k_o are the wave number. A_b, A_f and A_o are the cross-sectional areas, c_b, c_f and c_o are

the longitudinal mode velocities of sound in materials. l_b, l_f and l_o are the length of back section, front section and ceramic rings section.

When the transducer is at its mechanical resonance, its equivalent mechanical reactance can be ignored, i.e. X_m=0. Substituting the parameters of the Uthe 70-PTL piezoelectric driver in eqs. (2.11) to (2.16), it is found that the contact loss is relatively small and can be ignored. Thus, eqs. (2.11) to (2.16) can be simplified as follows [32]:

$$R_m = 0 \tag{2.17}$$

$$X_m = \frac{W_1 W_2}{W_1 + W_2} = \frac{Z_0[1 + (\frac{x+y}{Z_0})\cot k_0 l_0 - \frac{xy}{Z_0^2}]}{2\tan(\frac{k_0 l_0}{2}) + \frac{x+y}{Z_0}} \tag{2.18}$$

$$H = 0 \tag{2.19}$$

$$G = Z_0 \tan(k_0 l_0)_1 \tag{2.20}$$

Where $y = Z_f \tan(k_f l_f)$, (2.21)

$x = Z_b \tan(k_b l_b)$, (2.22)

When the transducer is at its mechanical resonance, X_m=0, eq (2.18) becomes zero and gives the following eq.

$$\tan^{-1}(\frac{x}{Z_0}) + k_0 l_0 + \tan^{-1}(\frac{y}{Z_0}) = \pi \tag{2.23}$$

Eq (2.23) is the frequency equation of the piezoelectric sandwich transducer. The first, second and third terms in eq. (2.23) represent the front section, the piezoelectric ring elements and the back section of the sandwich transducer, respectively. As the total length of the driver is equal to half a wavelength, the total phase length of the driver is equal to π. The phase length of front and back metal section and piezoelectric rings of the Uthe piezoelectric driver is 0.25π, 0.22π and 0.21π, respectively. (fig. 2.8)

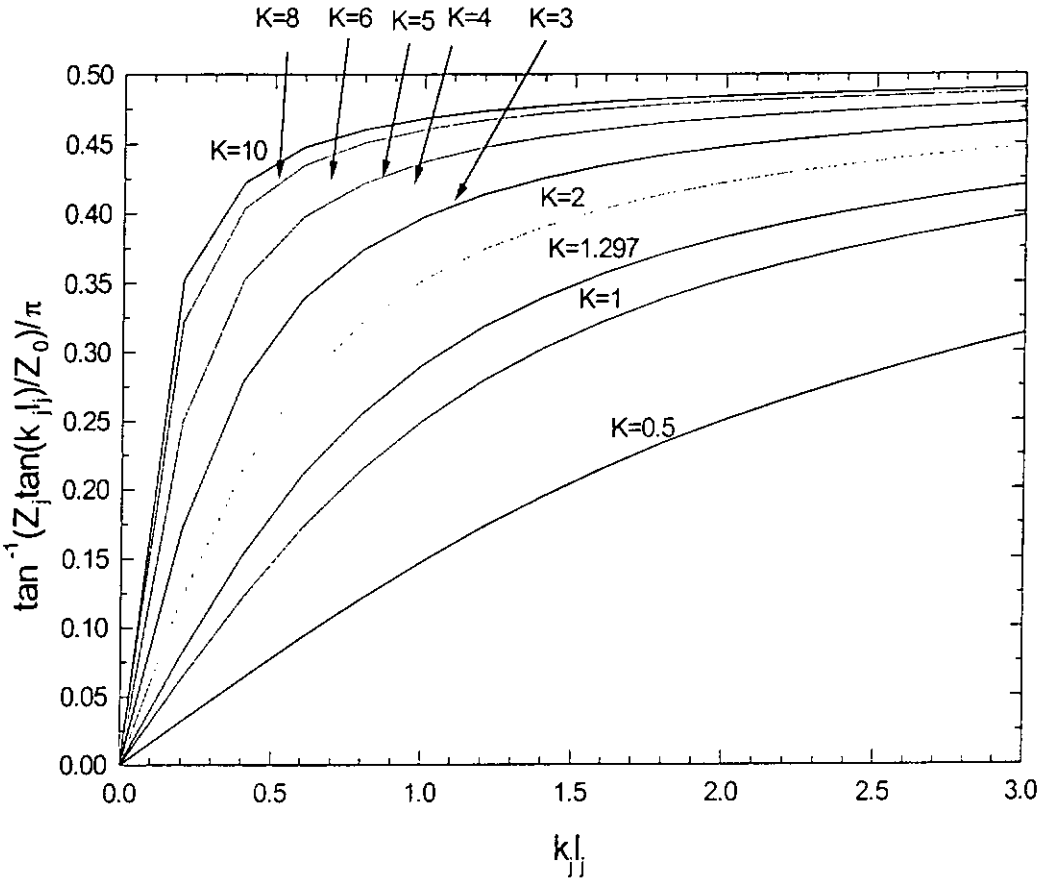

Fig. 2.8 Relation between phase length (kl) and $\tan^{-1}(Z_j \tan(k_j l_j)/Z_0)/\pi$. The subscript j either front (f) or back (b) metal section or the piezoelectric rings (o). The piezoelectric elements are assumed to be made of PZT –4, the materials of the front and back sections are 347 stainless steel (Appendix B). Any point on one of the curves represents a kind of transducer with an impedance ratio K ($=Z_j/Z_o$). Curve with K=1.297 respresents the Uthe 70-PTL piezoelectric driver.

2.3.2 The concentrator horn

The piezoelectric driver produces vibration amplitude which is too low for practical applications. It is a common practice to amplify the mechanical motion by means of a concentrator horn. Some of the popular choices are stepped, conical and exponential horns.

Main functions of the concentrator horn are the following:

(1) To amplify the displacement or particle velocity of the ultrasonic transducer.

(2) To provide a more suitable impedance matching between the ultrasonic transducer and the load to which it is coupled to.

(3) To resonate at the same frequency as the driving ultrasonic transducer.

The geometrical structure of the exponential concentrator horn with a cylindrical coupler on one end from a 70-PTL Uthe transducer is shown in fig. 2.9.

Using the wave equations for one-dimensional elastic solid in the x-direction [34]:

$$\frac{\partial^2 u}{\partial x^2} = \frac{1}{c^2}\frac{\partial^2 u}{\partial t^2} \qquad (2.24)$$

The solution of the above equation is [32-33]:

In the cylindrical coupler:

$$u_1 = a_1 \cos(k_1 x) + b_1 \sin(k_1 x) \tag{2.25}$$

In the exponential horn:

$$u_2 = e^{\alpha x}[a_2 \cos(k_2 x) + b_2 \sin(k_2 x)] \tag{2.26}$$

$$\alpha = \ln\zeta / L_2 \tag{2.27}$$

$$k_2 = (k_1^2 - \alpha^2)^{1/2} \tag{2.28}$$

where u_1, u_2 are the longitudinal displacement in the x-direction; a_1, a_2, b_1 and b_2 are arbitrary constants; k_1, k_2 are the wave numbers; α is a constant; ζ is the ratio of the radius of large end to that of small end of the exponential part.

Let the length of the cylindrical coupler be L_1 and the length of exponential horn be L_2, and the intersection of the cylindrical and exponential parts be x=0

At $x=-L_1$, $u_1=u_i$, $EA_1\varepsilon_1=-F_i$,

$$a_1 \cos k_1 L_1 - b_1 \sin k_1 L_1 = u_i \tag{2.29}$$

$$Ek_1 A_1 (a \sin k_1 L_1 + b_1 \cos k_1 L_1) = -F_i \tag{2.30}$$

where E is the Young's modulus; ε_1 and ε_2 are the stain; F is the force and A is the cross-sectional area. The subscripts 1, 2 represent the cylindrical coupler and the exponential horn, respectively.

At x=0, $u_1=u_2$ and stress $E\varepsilon_1=E\varepsilon_2$, (continuity of displacement and stress)

$$a_1 = a_2 \tag{2.31}$$

$$k_1 b_1 = \alpha a_2 + k_2 b_2 \tag{2.32}$$

At x = L_2, $u_2=u_o$, $E\varepsilon_2=0$, (free end condition)

$$e^{\alpha L_2}(a_2 \cos k_2 L_2 + b_2 \sin k_2 L_2) = u_o \tag{2.33}$$

$$(\frac{\alpha}{k_2} a_2 + b_2)\cos k_2 L_2 + (\frac{\alpha}{k_2} b_2 - a_2)\sin k_2 L_2 = 0 \tag{2.34}$$

Solving (2.24) to (2.34), the coefficients a_1, a_2, b_1 and b_2 are given as follow:

$$a_1 = u_i \frac{\Lambda_1}{\Gamma} = a_2$$

$$b_1 = u_i \frac{\Lambda_2}{\Gamma} \tag{2.35}$$

$$b_2 = u_i \frac{k_1 \Lambda_2 - \alpha \Lambda_1}{k_2 \Gamma}$$

where $\Lambda_1 = \cos k_2 L_2 + \frac{\alpha}{k_2} \sin k_2 L_2;$

$$\Lambda_2 = \frac{k_1}{k_2} \sin k_2 L_3 \qquad (2.36)$$

$$\Gamma = \Lambda_1 \cos k_1 L_1 - \Lambda_2 \sin k_1 L_1$$

At resonance, assumes F_i=0 in eq. (2.30) and then substituting (2.35), the frequency equation of the horn is

$$\tan k_1 L_1 = -\frac{\Lambda_2}{\Lambda_1} = -\frac{k_1 L_2}{\ln R + k_2 L_2 \cot k_2 L_2} \qquad (2.37)$$

where $k_2 L_2 = \sqrt{(k_1 L_2)^2 - \ln^2 R}$

The equations of the particle displacement can be found by substituting eq (2.35) into (2.25) and (2.26).

Cylindrical coupler:

$$u_1 = \frac{u_i}{\Gamma}(\Lambda_1 \cos k_1 x + \Lambda_2 \sin k_2 x) \qquad (2.38)$$

Exponential horn:

$$u_2 = \frac{u_i e^{\alpha x}}{\Gamma}(\Lambda_1 \cos k_2 x + \frac{k_1 \Lambda_2 - \alpha \Lambda_1}{k_2} \sin k_2 x) \qquad (2.39)$$

By differentiating eqs.(2.38) and (2.39) with respective to x and multiplying by the Young's modulus E, the stress equations can be found.

Cylindrical coupler:

$$\sigma_1 = \frac{E k_1 u_i}{\Gamma}(-\Lambda_1 \sin k_1 x + \Lambda_2 \cos k_1 x) \qquad (2.40)$$

Exponential horn:

$$\sigma_2 = \frac{Eu_i e^{\alpha x}}{\Gamma}[\alpha(\Lambda_1 \cos k_2 x + \frac{k_1\Lambda_2 - \alpha\Lambda_1}{k_2}\sin k_2 x) + k_2(-\Lambda_2 \sin k_2 x + \frac{k_1\Lambda_2 - \alpha\Lambda_1}{k_2}\cos k_2 x)]$$

(2.41)

The absolute value of the ratio of output and input displacement is defined as the displacement magnification factor MF. It is obtained by substituting eq (2.35) into (2.29).

(2.42)

$$MF = \left|\frac{u_o}{u_i}\right| = \left|\frac{\zeta}{\Gamma}\right|$$

At resonance, the magnification factor is

$$(MF)_{res} = \left|\frac{\zeta}{\Lambda}\cos k_1 L_1\right| = \left|\frac{\zeta \cos k_1 L_1}{\cos k_2 L_2 + \ln\zeta \dfrac{\sin k_2 L_2}{k_2 L_2}}\right| \qquad (2.43)$$

Inserting all the parameters for the transducer under study and the transducer is assumed to be made of aluminum alloy 6061T6, magnification factor is equal to 3.

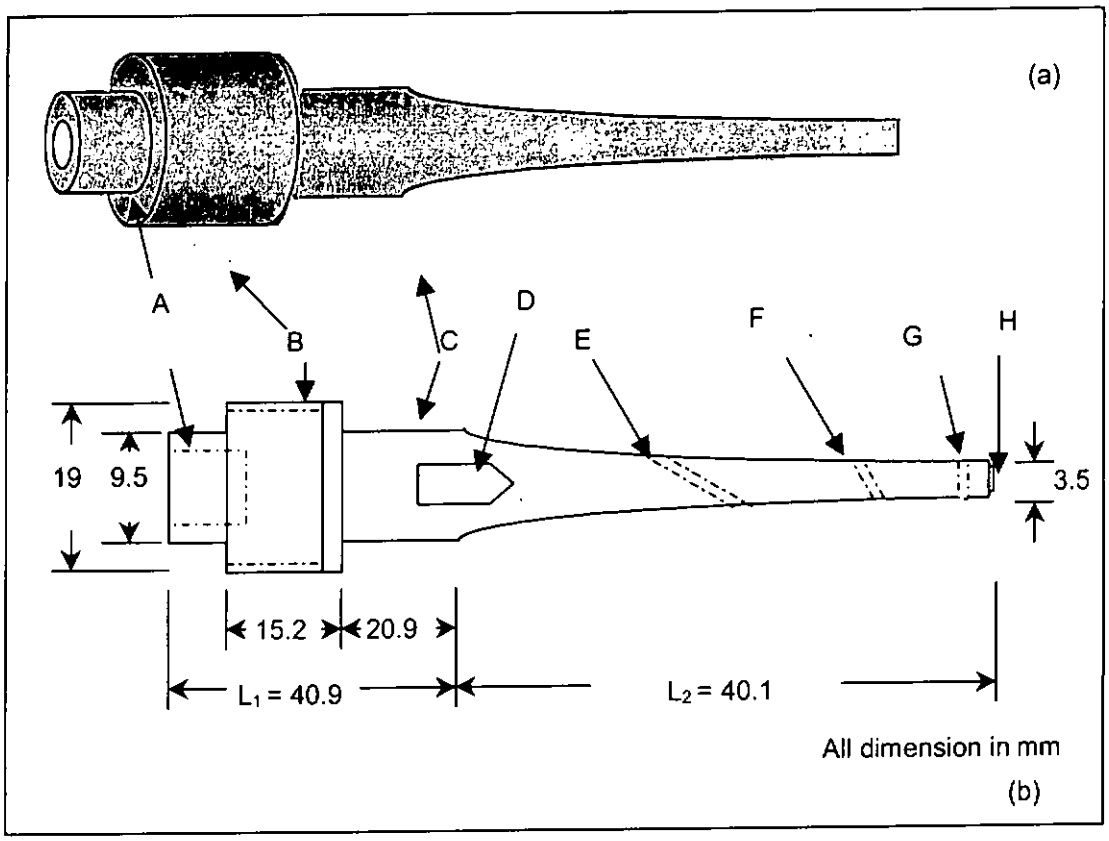

Fig. 2.9 The geometrical structure of a Uthe concentrator horn. (a) a solid body. (b) the layout of the horn. A represents the part for connecting the piezoelectric driver. B represents the barrel for clamping the transducer to the bracket. C represents the concentrator horn. D represents a flat surface cut on both sides of the horn. E represents the wire feed hole at 60°. F represents the wire feed hole at 30°. G represents the bonding tool hole and H represents the small screw for clamping the bonding tool.

Chapter 3

Selection of sensor material and its location

3.1 Introduction

Sensor works as a transducer that converts one form of energy carrying relevant information into another form which can be processed or interrogated. The six major categories of energy involved in sensing processes are – chemical, electrical, magnetic, mechanical, radiation and thermal energies. In this work, piezoelectric sensors which can convert mechanical to electrical energy and vice versa are studied.

Piezoelectric materials come in the forms of single crystal, ceramics, composites and polymers. They can be used as sensors, actuators, accelerometers, etc. To choose a suitable material as the sensing element and to find an optimum location for sensor placement in the wire bonding transducer are discussed in this chapter.

3.2 Sensor location

To choose a proper sensor location, some guidelines are needed. The sensor attaches at the chosen location should (1) produce a large enough output signals; (2) be sensitive to the mechanical change of the transducer; (3) reflect the mechanism of the bonding process.

In this work, the sensor is placed between the piezoelectric driver and the horn concentrator. As the piezoelectric diver is half wavelength long at the frequency of operation (62.5 kHz). the interface between the piezoelectric driver and the concentrator horn is an antinode which has a maximum axial displacement. The merits of this location are as follows:

(1) Since the sensor is inserted at the antinode of the transducer, it experiences a maximum axial ultrasonic displacement and produces a large output signal reflecting the effectiveness of the ultrasonic energy transmission.

(2) The sensor becomes an integral part of the transducer, forming part of the transmission path for the ultrasonic signals to reach the concentrator horn. Also, the bending force of the concentrator horn causes compression to part of the sensor and gives information about the bonding force;

(3) It generates signals related to the electrical and mechanical changes during the bonding process.

3.3 Sensor materials

All piezoelectric materials have a non-centrosymmetric crystal lattice and exhibit a piezoelectric effect (Appendix A). Materials that satisfy this criterion include polycrystalline ceramics such as lead zirconate titanate (PZT), piezoelectric ceramic/polymer composite and piezoelectric polymers such as polyvinylidene fluoride (PVDF).

Ceramics are compounds between metallic and non-metallic elements. These materials are typically insulative to the passage of electricity and heat, and more resistant to high temperature and harsh environments than metals and polymers. With regards to mechanical behavior, ceramics are hard but very brittle. Lead zirconate titanate —$Pb(Ti_{1-x}Zr_x)O_3$—PZT is one of the piezoelectric ceramics that can be used for sensing applications, and it has a perovskite structure. Above the Curie temperature, it has a cubic structure. Below the Curie temperature, it has a tetragonal structure. By varying the composition , the Curie temperature and the relative permittivity can be modified. In addition, by adding impurities (doping) , the properties of PZT can be modified considerably [36-38].

Kawai [39] discovered that polyvinylidene fluoride (PVDF) has piezoelectric activity which is several times larger than that in quartz. PVDF is a polymer, $(—CH_2—CF_2—)_n$, that has a crystallinity of 40 – 50%.

The PVDF crystal is polymorphic and the two most common forms are designated as α and β forms. Form β is polar and piezoelectric. High piezoelectric response is associated with the polar β form in which the hydrogen and fluorine atoms are arranged to give a maximum dipole moment per unit cell. The dipole moments of the crystallites are randomly oriented with respect to each other before the sample is electrically polarized. The piezoelectric polymer used in the present study is supplied in the form of a thin film by Atochem in U.S.A. It is flexible and has large compliance. This feature makes it suitable for a wide range of applications such as headphones, speakers, sensors, etc. The performance of these materials greatly depends on the thermal treatment and poling conditions. Besides, The main features of PVDF and its copolymer with TrFE, P(VDF-TrFE) are that they are both pyroelectric and piezoelectric, and they have high dielectric permittivity compared to other polymers due to their polar nature [40].

Piezoelectric ceramics/polymer composites are biphasic materials having a desirable combination of the best properties of the constituent phases. Usually, one phase (the matrix) is continuous and completely surrounds the other (the dispersed phase). 0-3 composite is the simplest type of connectivity patterns. It consists of piezoelectric ceramic particles dispersed in a 3-dimensionally connected polymer matrix. One of the features of 0-3 composites is their versatility in assuming a variety of

forms, including thin sheets, molded shapes, extruded bars and fibers. Most 0-3 composites studies previously were made of piezoelectric ceramic and non-piezoelectric polymer matrix. In this study, a piezoelectric ceramic/piezoelectric polymer PZT/P(VDF-TrFE) 0-3 composite is used as the sensor [40].

There are three kinds of piezoelectric materials being evaluated as possible sensor materials— PZT, PZT/P(VDF-TrFE) 0-3 composites and PVDF. Their material properties are given in Appendix B.

3.4 Tightening torque measurement

In order to install the sensor at the prescribed location. Care must be taken to ensure that the transducer performance will not be affected by the presence of the sensor, and the torque τ used to tighten the screw becomes very crucial. In this work, a 70-PTL ultrasonic wedge transducer made by Uthe Techology Inc., a HP 4194A impedance/gain phase analyzer, a computer and a Tohnichi Inc. 12 RTD torque driver were used to evaluate how the tightening torque τ affects the transducer performance. The setup is similar to that shown in fig. 2.1.

The sensor is a ring-shaped piezoelectric material. The outer and inner diameter is 9 mm and 5 mm, respectively. Three different materials, PZT, PZT/P(VDF-TrFE) 0-3 composite (with 50 volume fraction of PZT) and PVDF are used, their thickness are 0.8 mm, 0.3 mm and 0.1 mm, respectively. The sensor is sandwiched between the driver and the concentrator horn.

By varying the tightening torque applied to the transducer, in steps of 0.05 N•m, the spectra of electrical impedance Z and phase angle θ as functions of frequency can be measured by the analyzer. The data is then transferred to the computer for recording and further analysis. From the Z

and θ vs f spectra, the strongest minimum electrical impedance of the transducer is found and this corresponds to its resonant frequency f_R. Values of f_R, the electrical impedance Z_R and phase angle θ_R at f_R are recorded as functions of the tightening torque and shown in fig. 3.2 & 3.3.

The mechanical quality factor Q of the transducer is found by using an equivalent circuit as shown in fig. 3.1.The HP 4194A analyzer has an equivalent circuit option that can be used to simulate the ultrasonic transducer. When an equivalent circuit as shown in fig. 3.1 is identified, the analyzer can give values of L, R, C_a and C_b that provides the best simulation, hence Q can be calculated using eq (3.1). Then, the tightening torque is increased in steps of 0.05 until 1.2 N•m is reached.

$$Q = \frac{2\pi f_R L}{R} \qquad (3.1)$$

where Q is mechanical quality factor; f_R is the resonance frequency; L and R are inductance and resistance of the equivalent circuit, respectively.

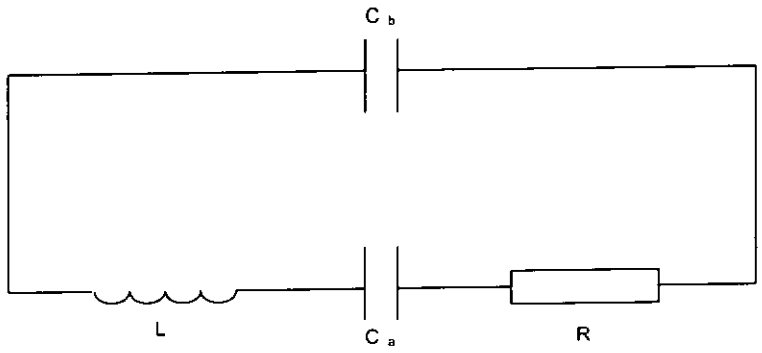

Fig. 3.1 An equivalent circuit of the ultrasonic transducer. L is inductance, R is resistance. C_a and C_b are the capacitance.

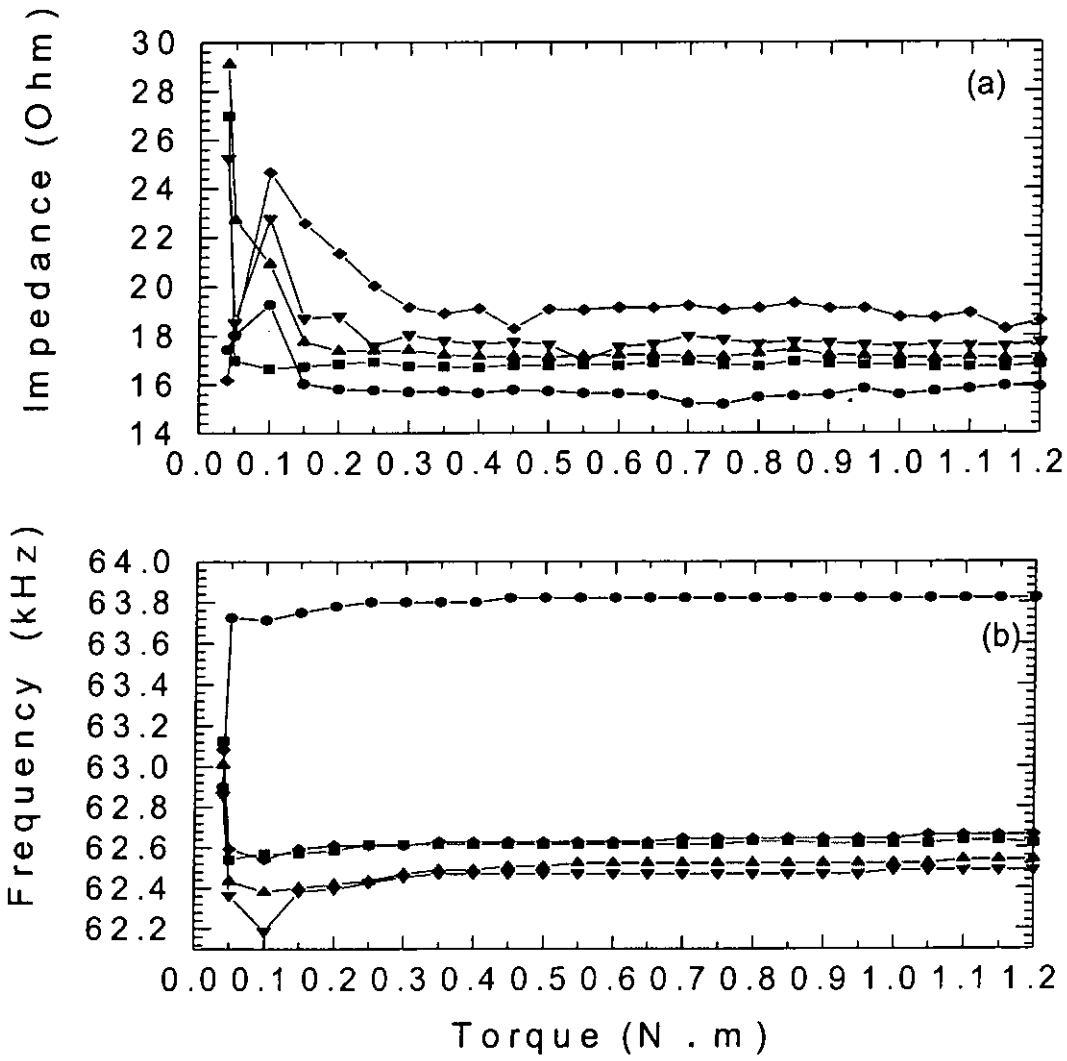

Fig. 3.2 The results of (a) electrical impedance (b) resonance frequency of different piezoelectric materials against the tightening torque. – ■ – represents transducer without sensor but with wedge; – ● – represents transducer without sensor and wedge; – ▲ – represents PZT as the sensor (with wedge) ;– ▼ – represents 0-3 composite as the sensor (with wedge) and – ◆ – represents PVDF as the sensor (with wedge).

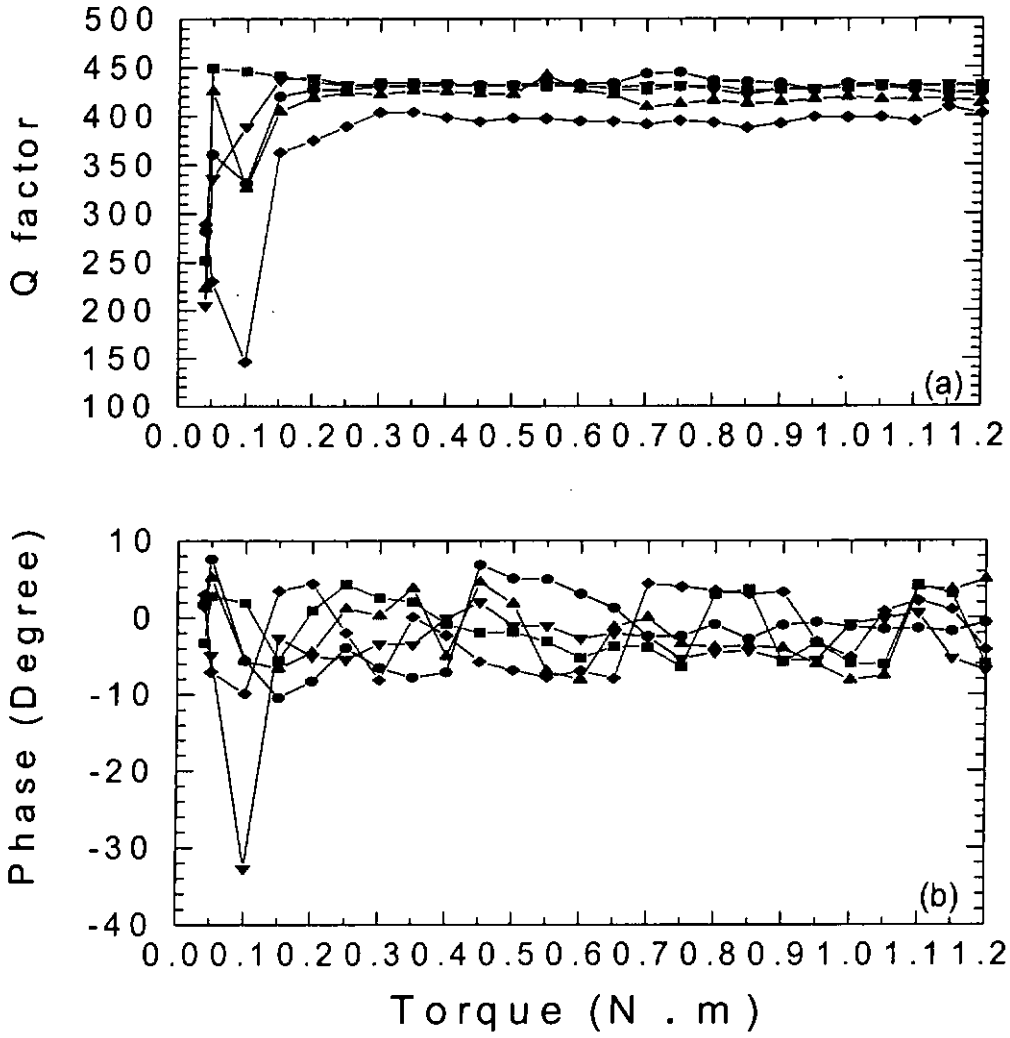

Fig. 3.3 The results of (a) Q factor (b) phase angle of different piezoelectric materials against the tightening torque. – ■ – represents transducer without sensor but with wedge; – ● – represents transducer without sensor and wedge; – ▲ – represents PZT as the sensor (with wedge);– ▼ – represents 0-3 composite as the sensor (with wedge) and – ◆ – represents PVDF as the sensor (with wedge).

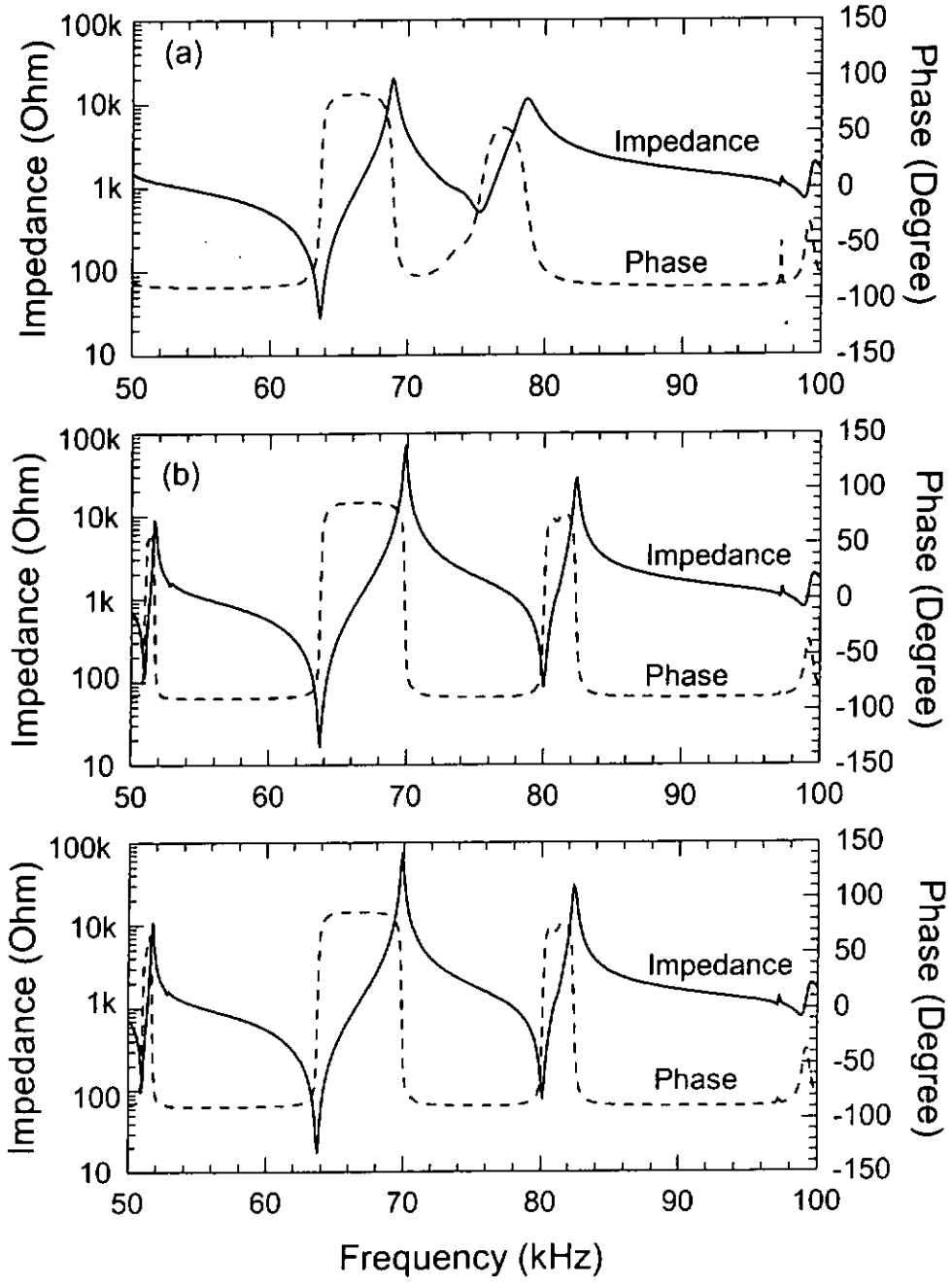

Fig. 3.4 The spectra of electrical impedance and phase angle against frequency with PVDF sensor under (a) 0.05 N•m (b) 0.7 N•m (c) 1.2 N•m of tightening torque.

Fig. 3.2 and fig. 3.3 show the results of the tightening torque experiments. It is found that the bonding tool can affect the characteristic of the transducer. After attaching the bonding tool to the transducer, the electrical impedance is 5% higher than that of the transducer without the bonding tool and the resonance frequency (frequency of minimum impedance) shifts from 62.6 kHz to a high frequency range (63.8 kHz). However, the Q factor and the phase of them are relatively unaffected.

After inserting the piezoelectric material between the driver and horn, the characteristic of the transducer has also changed. However, it is still in an acceptable range. (The resonance frequency range is 62.1-63 kHz and the electrical impedance is 14-23 ohm).

The acoustic impedance (Z_a = density × velocity of sound) matching is an important factor that affect the transducer electrical impedance. As the sandwich driver is made of ceramic that has acoustic impedance closed to that of PZT, the electrical impedance of the transducer with a PZT sensor has value closest to the original transducer than that of the transducer with composite and PVDF sensor as shown in fig. 3.2a. When the applied torque is less than 0.15 N•m, the contact between the piezoelectric driver and the concentrator horn is poor due to the screw between them being loose which results in a fluctuation of the electrical impedance.

Fig. 3.2b shows values of the resonance frequency against the tightening torque, the curve of the transducer with a PVDF sensor is closest to that of the original one which may be owing to the difference in thickness of the sensor elements. Being the thinnest, the PVDF causes least shift in the resonant frequency and results in less changes in the characteristic of the transducer. The fluctuation of phase angle for different sensor materials in fig. 3.3d is due to background noise.

It is found that when the applied tightening torque varies from 0.05 to 0.3 N•m, the resonance frequency, electrical impedance and Q factor are rather unstable. The piezoelectric driver and the concentrator horn are in poor contact due to the screw between them being loose and poor coupling occurs during energy transmission from the driver to the sensor. In addition, the spectra of the electrical impedance and phase angle against different frequencies shows a clear and pure resonance peaks at a tightening torque of 0.7 N•m (fig. 3.4b). If the torque is less than 0.7 N•m, the resonance peaks are not sharp (fig. 3.4a). Above 0.7 N•m, the impedance and phase spectra are similar to the spectra of at 0.7 N•m of torque (fig. 3.4c). Therefore, the minimum torque for tightening the driver and solid horn is about 0.7 N•m.

When choosing a proper sensor material, besides considering the electrical properties, other criteria such as the mechanical properties are

also important. At the location of the sensor placement, the sensor needs to tolerate a high compression force, the ceramic is not suitable because it is easy to break when the thickness is thin. The fabrication of composite is relatively more complicated than that of PVDF which will raise the cost of the sensor. So, a PVDF sensor is chosen as the sensor material for subsequent study.

3.5 Effect of electrode pattern on received signals

Prepoled PVDF film (0.1 mm thick, from Atochem, U.S.A.) covered with aluminum electrodes on both sides were used in the sensor fabrication. NaOH was used to etch away the undesired electrode area and the configurations of the sensors are shown in fig. 3.5. Electrical wires were connected to the sensors by silver epoxy. Then, epoxy was used to insulate the joints and to fix the electrical wire.

There are five electrode patterns on the PVDF sensors as shown in fig. 3.6. The gray area represents the electroded part while the white area represents non-electroded areas. A-type electrode pattern is a ring shape that covered the entire sensor surface. A cross-shaped electrode pattern is the B-type. C-type pattern has a butterfly shape. D-type is quite similar to the B-type electrode pattern, but its inner perimeter has no electrode. E-type electrode pattern uses the left and right hand electrode patterns similar to the B-type but with the top and bottom electrodes similar to the D-type. The B, C, D and E type electrode patterns have four regions- top, bottom, left and right. Each of them detects the changes in mechanical stress in the four different regions of the ultrasonic transducer.

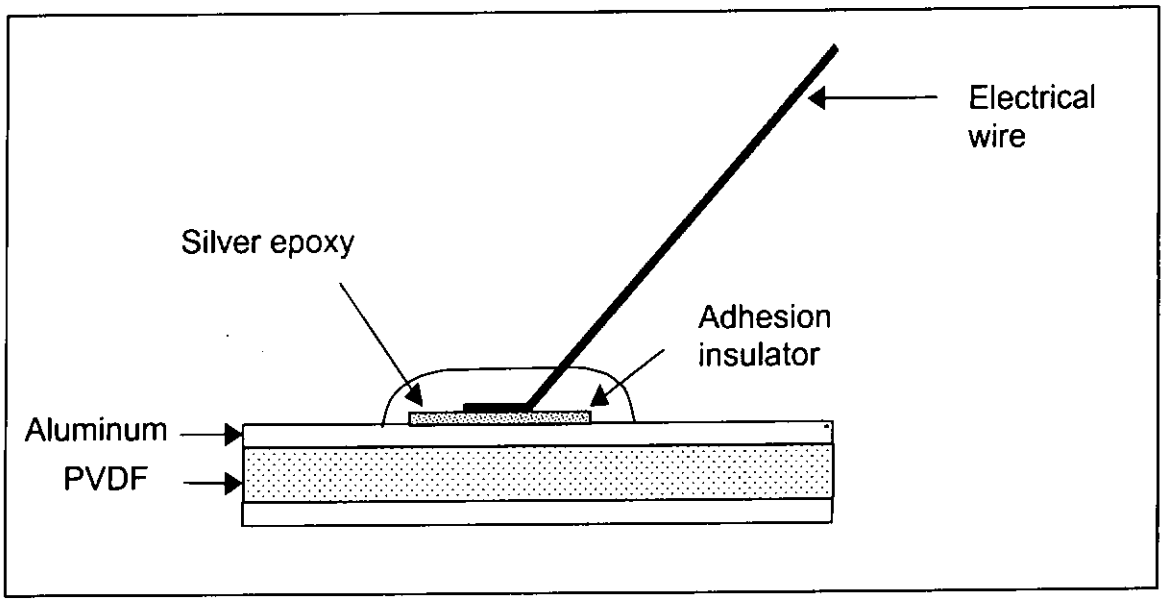

Fig. 3.5 A schematic diagram of the sensor.

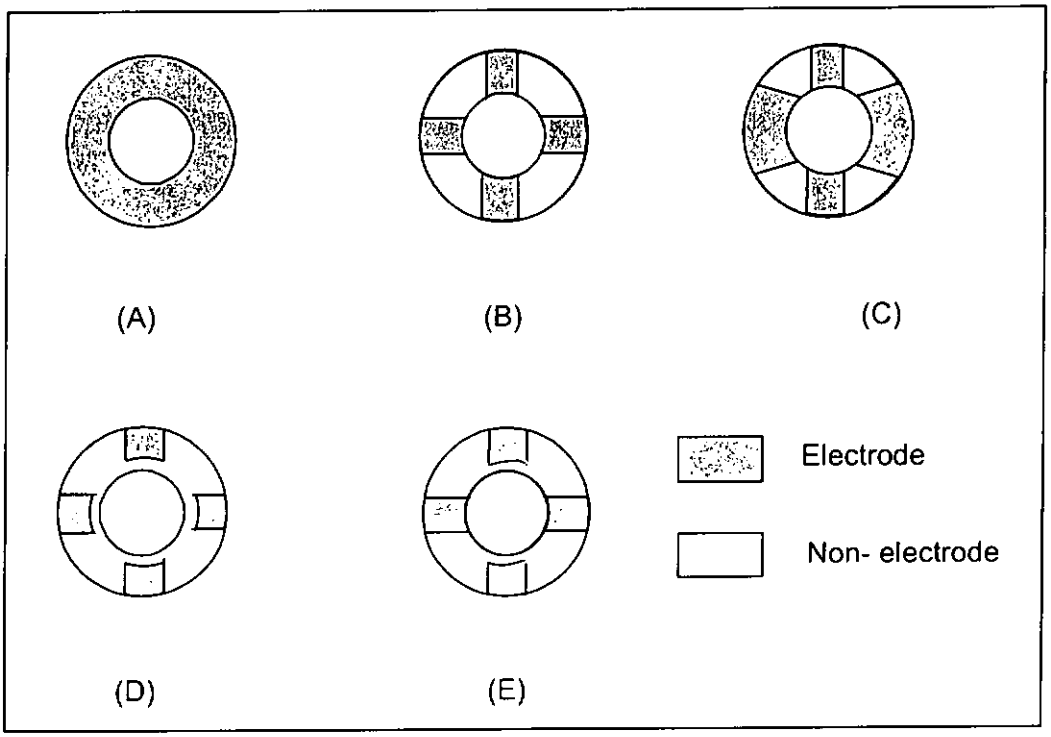

Fig.3.6 Five different types of electrode patterns of the sensors. (A) a ring shape electrode (B) a cross shape electrode (C) a butterfly-like electrode (D) an outer-cross shape electrode and (E) symmetric cross shape electrode.

3.5.1 Sensor output during wire bonding

Experimental setup to evaluate the sensors with different electrode patterns is shown in fig. 3.7. The piezoelectric sensor and an insulator situated between the piezoelectric driver and the concentrator horn is affixed to a 70-PTL ultrasonic wedge transducer using a 0.7 N•m tightening torque. The transducer is then fixed to the bracket of the bonder by clamping at the barrel. The output signal is amplified and filtered by a SR 560 preamplifier and then fed to a HP 54522A digital oscilloscope. The output signal from the sensor is also fed directly to the oscilloscope. Appropriate filtering is used to remove the noises. The filter is set at a cut-off frequency of 100 Hz with a gain of 10.

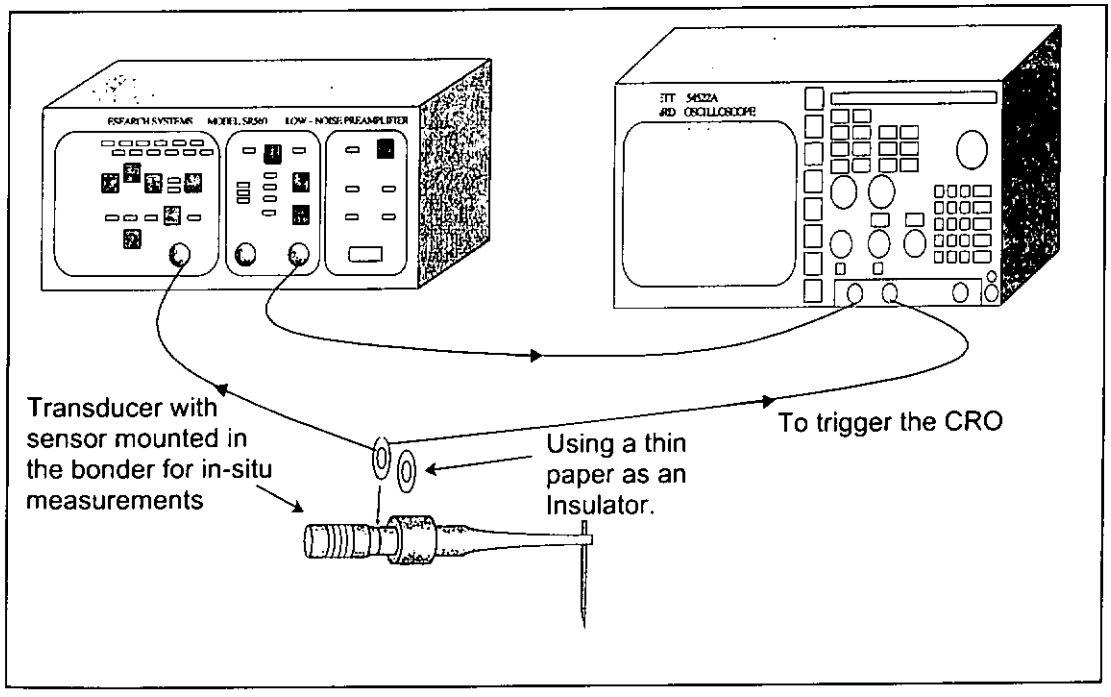

Fig.3.7 The experimental setup.

3.5.2 Results and discussions

Figs. (3.8 - 3.12) show the signals captured by different sections in different types of electrode patterns.

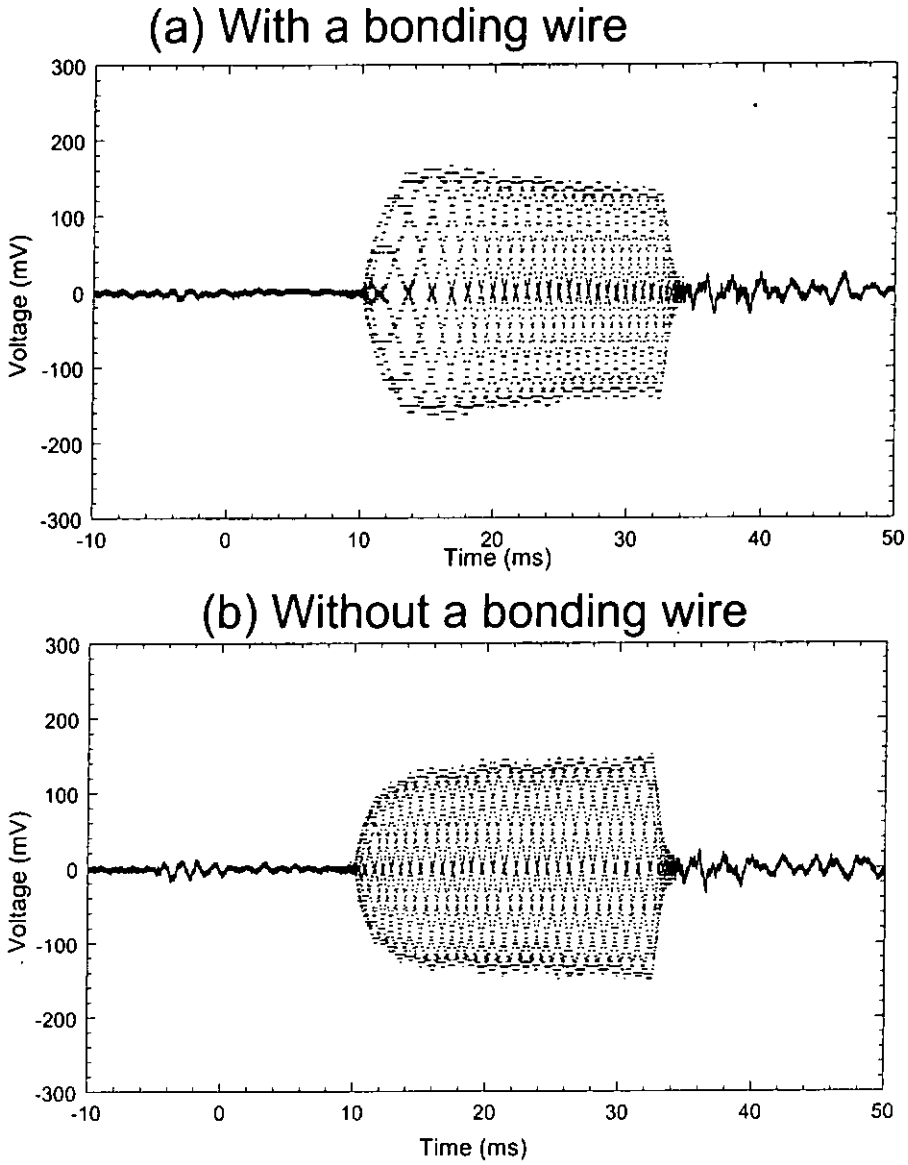

Fig. 3.8 Signals captured by a sensor with an A-type electrode pattern when the transducer is operated (a) with a bonding wire and (b) without a bonding wire and background noises are filtered with a low frequency cutoff at 100 Hz. The amplification factor is 10.

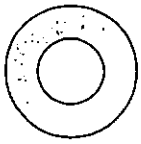

A-type electrode attern

Type A electrode pattern

Fig. 3.8 shows the signals captured by a sensor with a ring electrode pattern (fig. 3.6a). When the bonding tool touches down on the bonding pad (at time ~ -5 ms), impact force signal is observed. However, amplitude of the impact force signal is not very sharp. This is because the output signal is a sum of signals from various part of the whole ring electrode and partial cancellation occurs which results in a weak output impact force signal. So, this kind of electrode pattern is not suitable for detecting the impact force. However, using type A electrode pattern can give good ultrasonic signals and signals from a transducer with or without a bonding wire are distinctly different.

With a bonding wire, the front part of the signal is larger and it decreases sharply to a constant level. When the wire is missing, the forefront part of the ultrasonic profile is sharp and small. Then, the signal amplitude increases slightly. Microscopically, there are three phases in the ultrasonic wire bonding process. They are the cleansing phase, mixing phase and diffusion phase, respectively. With a bonding wire present, the wire will go though these three phases and absorb the energy whether the bond quality is good or not. However, the energy will be loss in the missing wire condition and resulting in the forefront part of the ultrasonic amplitude being sharp and small. The cleansing phase and mixing phase occur in

time between 10 ms to 25 ms, the steady level of the ultrasonic amplitude represents the diffusion phase.

As the bonding tool of the transducer touches down or lifts off from the bonding pad, the concentrator horn of the transducer experiences bending force which is more pronounced in the upped and bottom part of the horn. When the top part of the horn is compressed during touch down, the lower part is extended and the opposite happens during lift off. Hence, dividing the sensor into four sections enables the sensor to detect different signals. The top and the bottom parts collect the impact force information while the left and right sections capture the ultrasonic signals. To facilitate description, we use part α to represent the top and bottom sections of the sensors which are aligned in a direction parallel to the bonding tool (for force detection) and part β to represent the left and right sides of the sensor which are position horizontally and are perpendicular to the bonding tool (for ultrasonic signal detection).

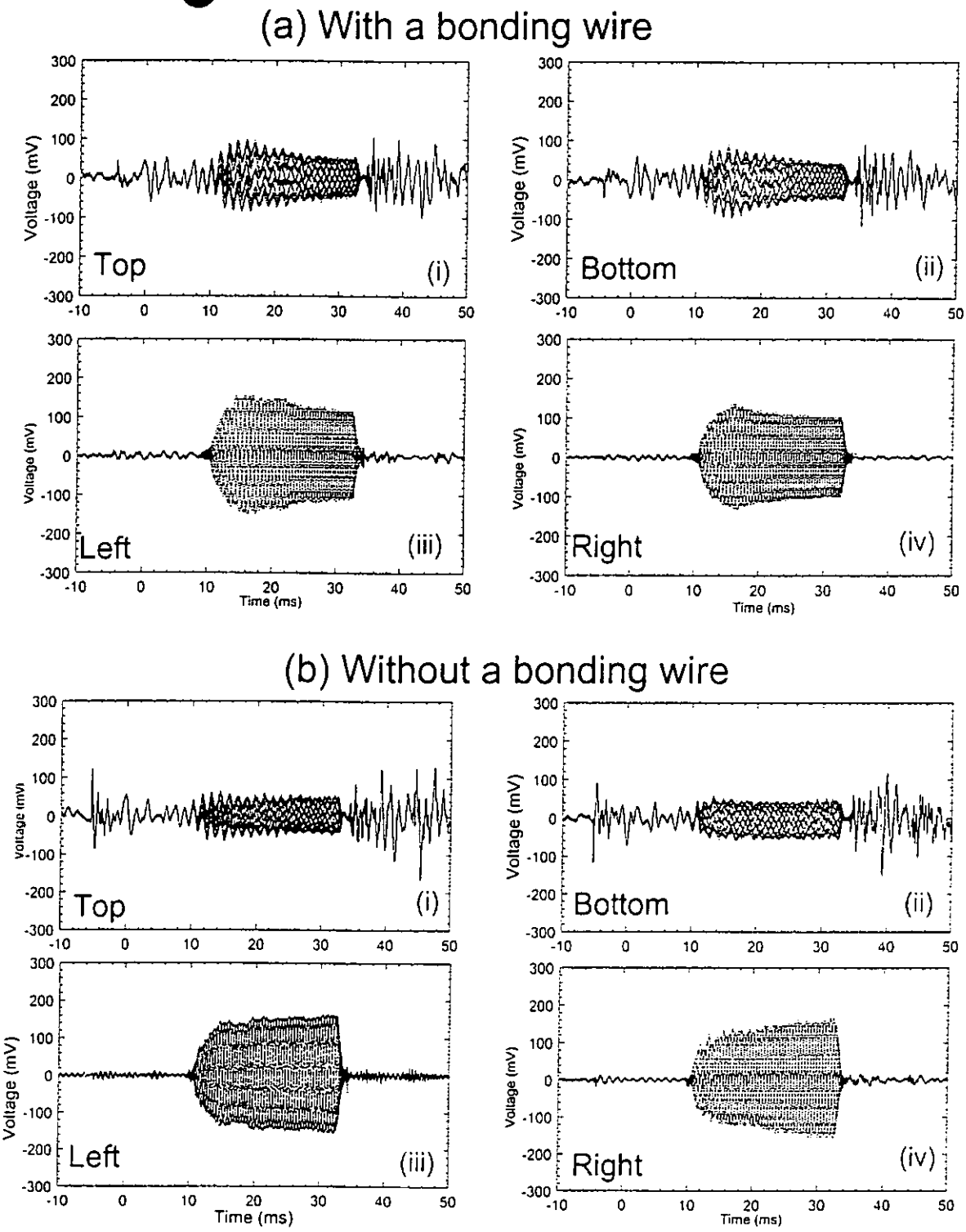

Fig. 3.9 Signals captured by a sensor with a B-type electrode pattern when the transducer is operated (a) with a bonding wire and (b) without a bonding wire and the background noises are filtered. The amplification factor is 10.

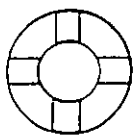

B-type electrode pattern

Type B electrode pattern

Fig. 3.9 represents the output signals detected from a sensor with a type B electrode pattern (Fig. 3.6b). It indicates that part β of the sensor can give good ultrasonic signal, which can be used to distinguish whether the transducer has a wire or not. However, force signals from part α are not very satisfactory in indicating the changing of the wiring conditions. For impact force detection, part α is better than the β. The vibration signals detected by part α overlap with the ultrasonic signals, and amplitude modulation occurs.

After the bond is formed, the transducer lifts off, and it vibrates again in the up and down directions. In fig. 3.9 (ai,ii) and (bi,ii), impact force occur at a bonding time t_B ~ –5 ms, the ultrasonic power is applied at t_B ~ 10 ms, for a duration of 34 ms, the bond is formed and the transducer lifts up and the vertical vibration of the transducer is detected again by part α of the sensor.

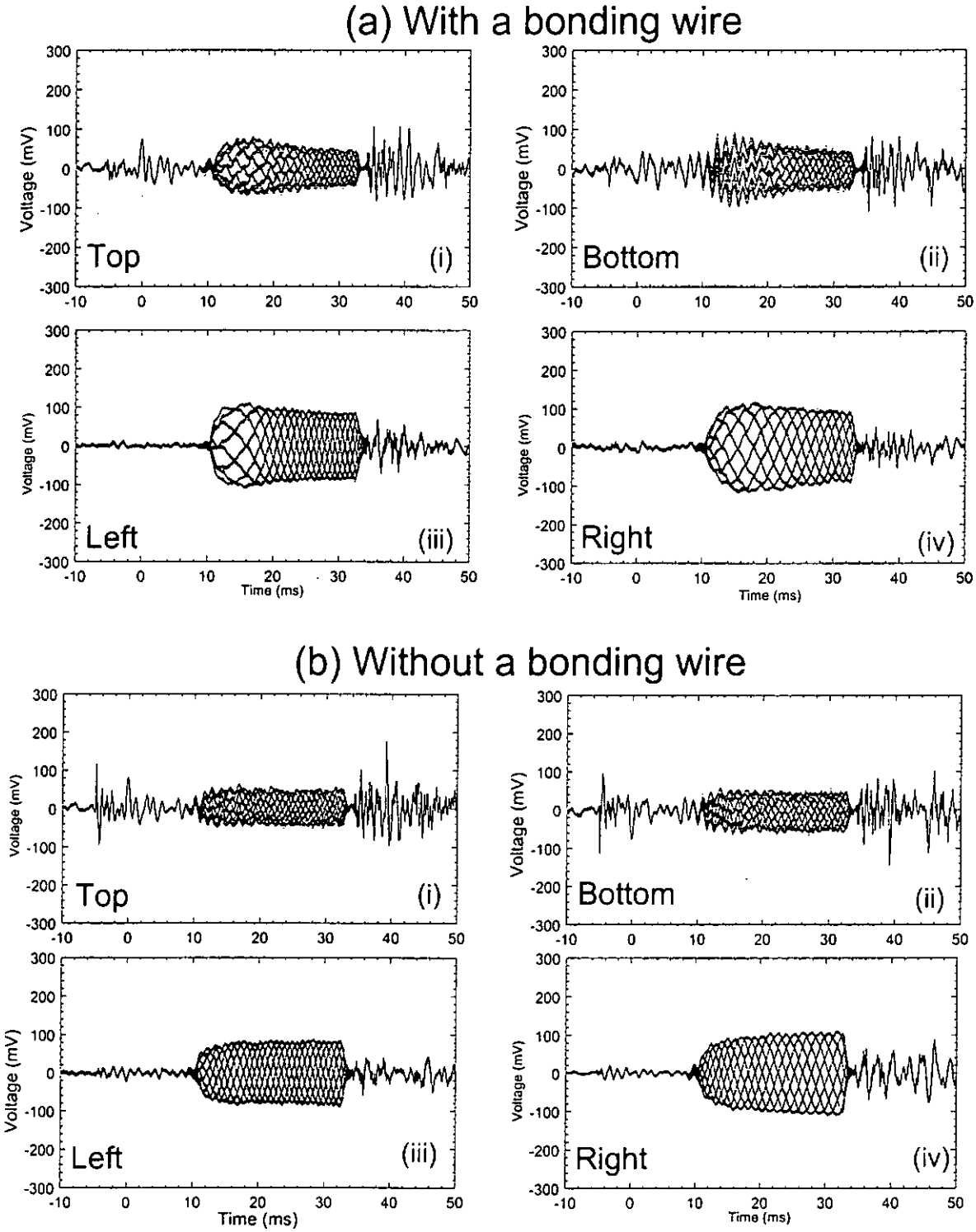

Fig. 3.10 Signals captured by a sensor with a C-type electrode pattern when the transducer is operated (a) with a bonding wire and (b) without a bonding wire and the background noises are filtered. The amplification factor is 10.

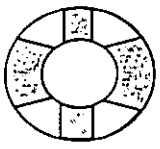

C-type electrode pattern

Type C electrode pattern

Fig. 3.6c shows that in the type C electrode pattern the shapes of part α is similar to that in type B pattern (fig. 3.6b) and the sensor output from part α (fig. 3.10) is also quite similar to that shown in fig. 3.9 (i &ii). However, part β in a type C electrode pattern is wing-shaped and covers larger areas. Due to averaging, the result is less sensitive to the change in wiring condition when compared to output from part β of type B electrode. (Fig. 3.9 iii & iv). A larger electrode area in part β gives a smaller change in the ultrasonic profile. Although the profile of the signal is not very clear, time for the bonding sequence can still be found which matches the previously discussed results.

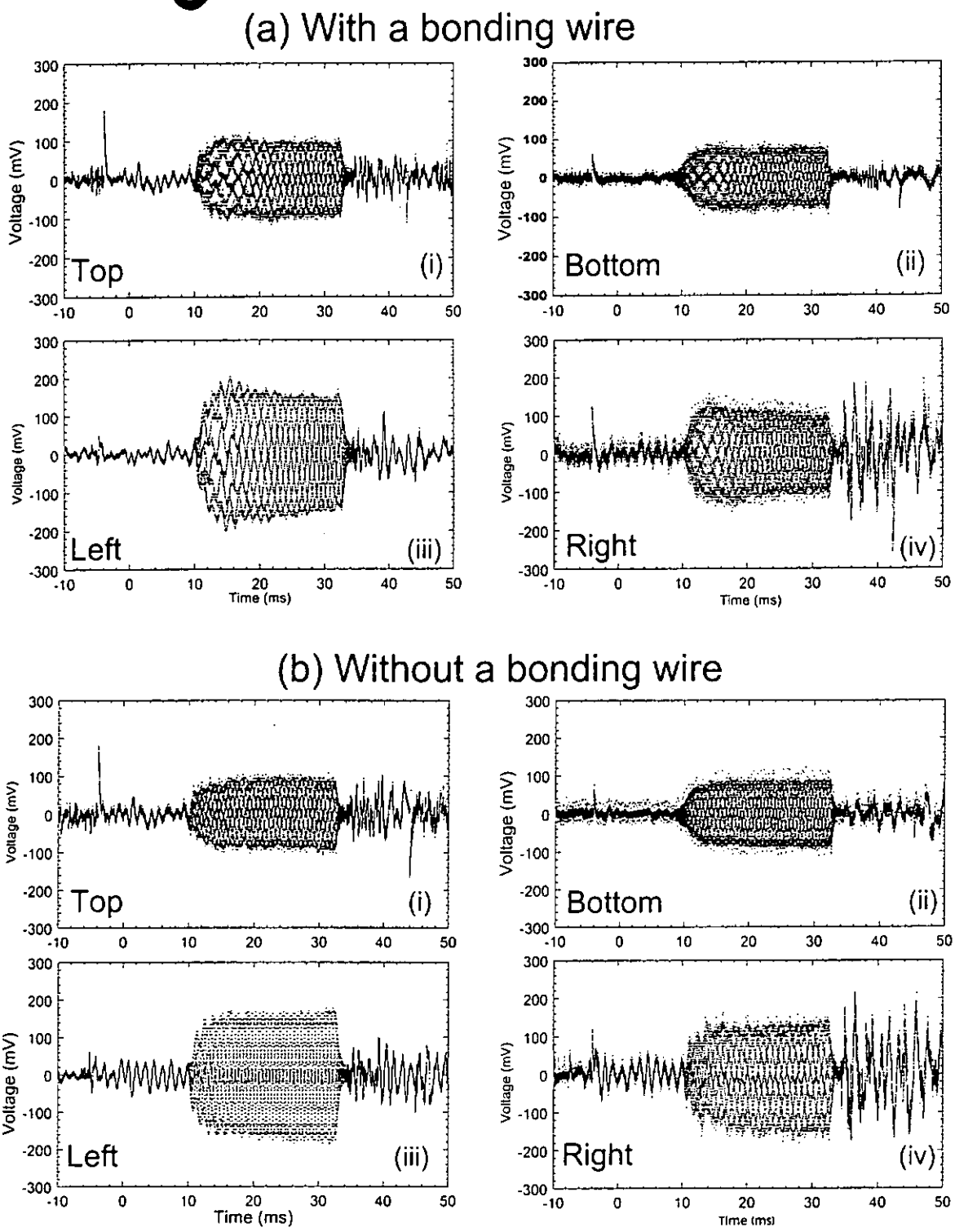

Fig. 3.11 Signals captured by a sensor with a D-type electrode pattern when the transducer is operated (a) with a bonding wire and (b) without a bonding wire and the background noises are filtered. The amplification factor is 10.

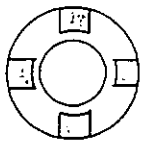

D-type electrode pattern

Type D electrode pattern

Electrode pattern D shown in fig. 3.6d has a ring-shaped inner area that has no electrode but is still divided into four separate sections. Figs. 3.11a and 3.11b display signals captured when the transducer is operating with and without a bonding wire, respectively. Signals captured from part α (fig. 3.11 (i & ii)) show that the impact force signal from the upper electrode is larger than that from the lower electrode. And it is less sensitive to the transducer vibrations. For output from part β, the right electrode also can detect the impact force signal. Besides, the right part of the sensor is also more sensitive to the low frequency signals than other electrode pattern described previously. However, the change in the ultrasonic signal for transducer with or without a bonding wire is not so clear.

On the other hand, the bonding time also matches with the previously described results. The transducer touches down at t_B ~ –5 ms, the ultrasonic signal is generated at t_B ~ 10 ms; the bonding duration is ~ 22 ms and then the transducer lifts off and moves to other bonding position.

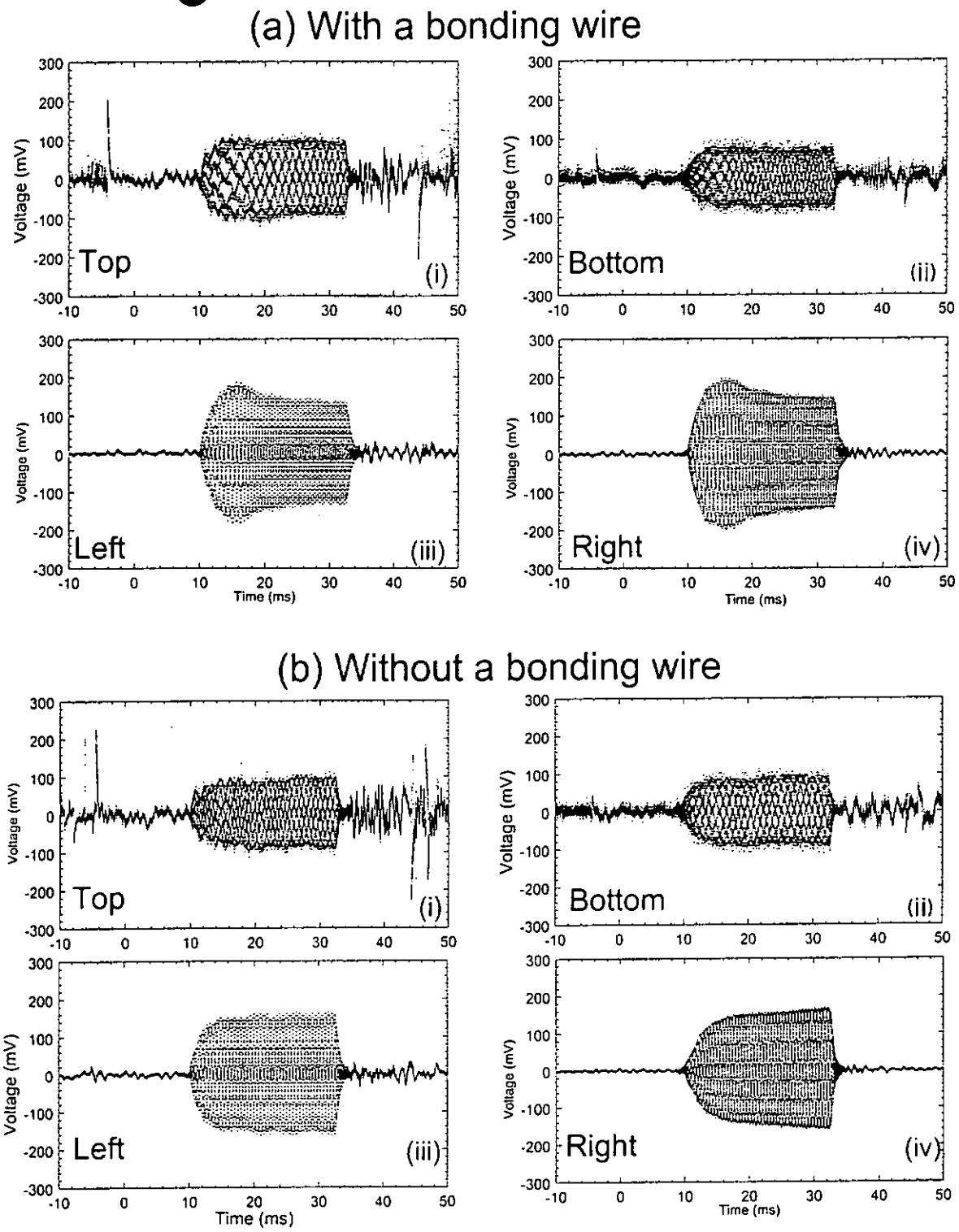

Fig. 3.12 Signals captured by a sensor with a E-type electrode pattern when the transducer is operated (a) with a bonding wire and (b) without a bonding wire and the background noises are filtered with a low frequency cutoff at 100 Hz. The amplification factor is 10.

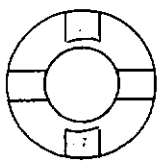

E- type electrode pattern

Type E electrode pattern

Part α of the E type electrode pattern is the same as that in a type D electrode, while part β is similar to that in a type B electrode. The results obtained by using this type of sensor is shown in fig. 3.12. As the shape of part α is similar to that in electrode type D, the results are quite similar. The upper part of the sensor is more sensitive to the force signal compared to the lower part. The profile of signals from part β is similar to that given by part β of the B type sensor. It can also be used to detect the variation in the wiring condition of the transducer. In case with the wire missing, the forefront part of the ultrasonic profile is sharp and small (fig. 3.12b iii & iv). Then, the signal amplitude increases slightly. For the condition with a bonding wire, the front part of the signal is larger and it decreases sharply to a constant level. Besides, the time sequence of the bonding also matches to that described previously for other types of sensors.

Electrode pattern evaluation in this chapter shows that the shape of the sensor electrode can influence the output signals. Comparing the results obtained from the five kinds of electrode patterns, it is found that part α of type D and part β of type B or E can give satisfactory force and ultrasonic signals which can be used to distinguish whether the transducer is operating with or without a bonding wire.

Chapter 4

Analysis of sensor signals

4.1 Introduction

In Chapter 3, we found that sensor with type E electrode pattern is a good choice for detecting the impact force and ultrasonic signal. It has four electrically insulated segments. The top and bottom electrodes are positioned symmetrically with respect to the vertical direction which is parallel to the bonding tool. The left and right electrodes are positioned symmetrically with respect to the horizontal direction which is perpendicular to the bonding tool.

The two pairs of electrodes are used to sense different parameters. The top and bottom pair is used to sense the bonding force. These electrodes are more responsive to the bending of the transducer when the bonding tool contacts the bonding pad because they are aligned vertically. The horizontal positioned electrodes are used for measuring the ultrasonic amplitude and the duration of the ultrasound burst.

The output from the electrode is fed to different kinds of filter and amplifier in order to analyze the force and ultrasonic signals separately.

4.2 Low frequency signals

Low frequency signals (<1 kHz), after passing through a low-pass filter (Model SR 650, Stanford Research Systems, INC), originate from the mechanical vibrations of the transducer. It is a result of the designated ultrasonic bonding process. The factors that cause mechanical vibrations are as follows: (1) the bending moments of the concentrator horn; (2) the vibration produced by the switching of the contact sensor in the bond head.

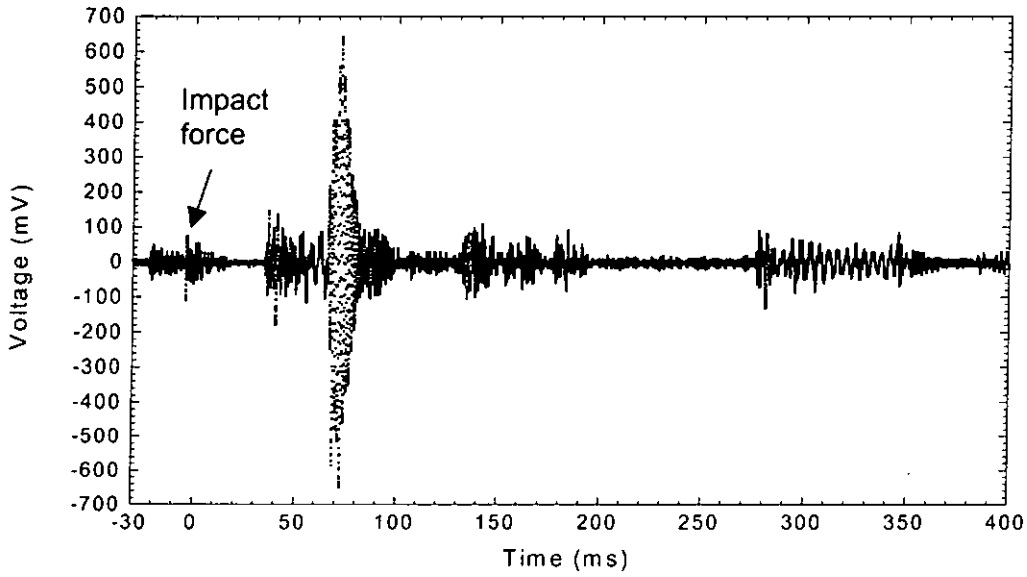

Fig. 4.1 The profile of low frequency signals captured by an upper electrode of E type sensor with 50k sample / second sampling rate. The record length is 32768 points. The record time is 655.36 ms.

Fig. 4.1, shows the profile of low frequency (< 1 kHz) signals recorded during the process of ultrasonic bonding between an IC die to the chip carrier. The ultrasonic transducer starts to move downwards at t_B ~ –13 ms and hits the IC die at t_B ~ –4 ms. In the interval between t_B = –4 to 18 ms, the oscillations represent damping of the concentrator horn. At 10 - 34 ms, the bonding tool contacts the surface of the IC die and makes a weld. Afterwards, the transducer lifts off and bouncing occurs from 35 – 63 ms. At 63 ms, the large impact signal is caused by the reaction force produced due to the switch of contact sensor is being closed and hits the bond head surface. During t_B = 90 – 136 ms, the transducer moves from the first bond to the second bond location.

From t = 136 – 150 ms, the transducer starts to move downward and is bouncing, then impacts on the surface of the package at t = 173 ms. Afterwards, the concentrator horn of the transducer is being damping in between 173 – 200 ms. At t = 273 ms, the wire is torn and then the transducer lifts upward at t = 276 ms. After lift-off, the transducer returns to its original height at t = 276 – 344 ms and damps out at t = 370 ms.

If we focus on the formation of the first bond, at t = -10 to 50 ms, and analyze the sensor output under two bonding conditions, namely when the transducer is operated with the bonding wire and when the transducer is operated without the bonding wire. Other bonding parameters are kept

constant. In this time interval, the signals mainly show the impact of the transducer on the IC die and its damping vibrations. The ultrasonic signals have been filtered off.

Fig. 4.2 shows the sensor (with type E electrode) output from the four electrode segments of the sensor under two bonding conditions. No matter what the bonding conditions are, the signal profiles from the left and right sensors are quite similar. However, the signal amplitude when the bonding wire is absent is larger than with the wire.

Besides, the signal amplitudes from the top and bottom sensors are higher than that from the left and right ones. This implies that the mechanical vibration of the concentrator horn is mainly in the vertical direction.

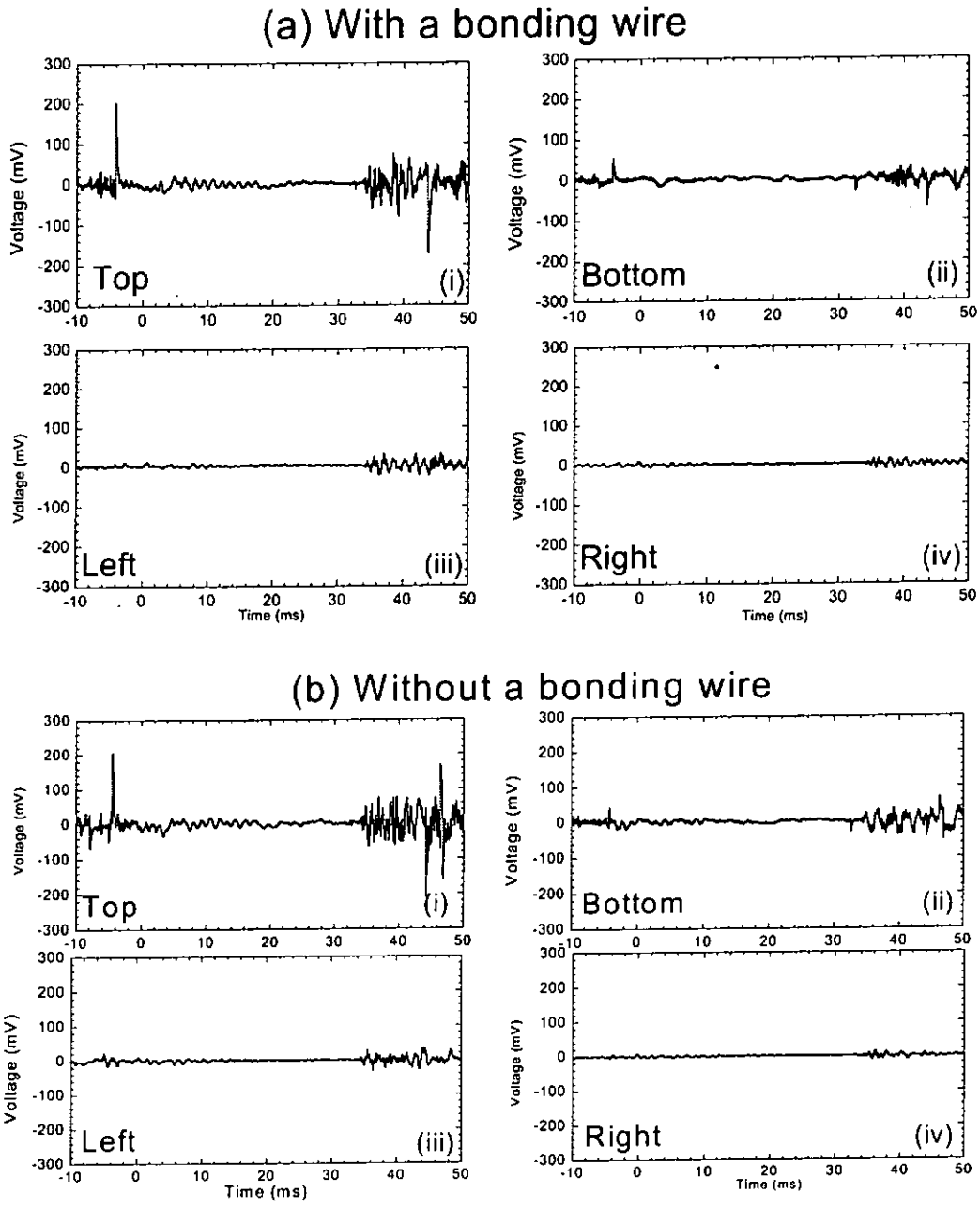

Fig. 4.2 The low frequency signals captured by the four electrode segments of E type sensor (a) with a bonding wire and (b) without a bonding wire on a new bonding pad. The sampling rate is 500 k sample / second with a record length of 32768 points.

4.3 High frequency signals

Using a high-pass filter (Model SR 650, Stanford Research Systems, INC) to filter off signals with frequencies lower than 62 kHz. High frequency signals can be obtained from the four electrode segments of the sensor. The output from the left sensor is given in fig. 4.3. Signals with frequency about 62.1~ 63 kHz represent the ultrasonic energy that is produced by the piezoelectric driver. At 10 – 34 ms and 185 - 267 ms, ultrasonic bursts can be observed. The first and second bonds are formed in these durations.

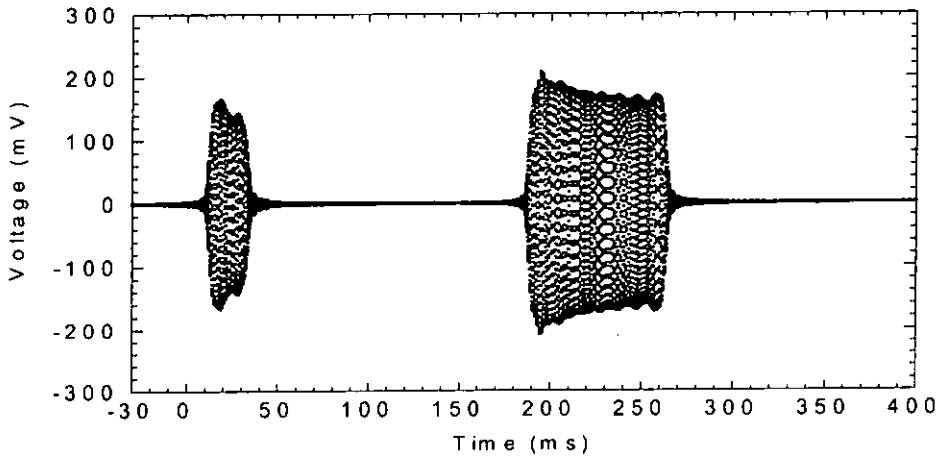

Fig. 4.3 High frequency signals captured by the left electrode of E type sensor with a bonding wire and filtered by a high pass filter with 62 kHz cut-off frequency. The ultrasonic power dial setting is 3.1. The sampling rate is 50 k sample / seconds with a record length of 32768 points.

Fig. 4.4 shows two bonding conditions as described in the previous section. The shapes of the profile are different in the two figures because of the alteration of the boundary conditions at the tip of the bonding tool. When the Al wire is present, it is situated between the bonding tool and the bond pad. When the wire is missing, the bonding tool contacts the bond pad surface directly. The ultrasonic signal has a larger initial amplitude when the wire is present. Then, this signal decreases steadily and becomes rather constant. This larger initial amplitude is not seen in the missing wire condition.

Moreover, amplitudes of the sensor output from the left and right electrode pairs are larger than that from the top and bottom electrode pair in both bonding conditions. This is because the top and bottom electrode pair has no electrode near the centre and this part of the electrode is more sensitive to the ultrasonic energy. It is noted that the A-type electrode pattern also can give good ultrasonic signals (fig. 4.5). Hence, if we are looking for a sensor pattern that can give good ultrasonic signal amplitude only, the A-type electrode pattern can be used.

The fundamental resonant frequency of the ultrasonic signals is about 62.8 kHz. Using a Fast Fourier transformation (FFT) method to analyze signals in fig. 4.4, the second and third harmonic components contained in the signal are also found. Fig. 4.6 shows that the strongest signal is the one

with the fundamental frequency, the second and third harmonics are much weaker (~ -30 dB) than the fundamental.

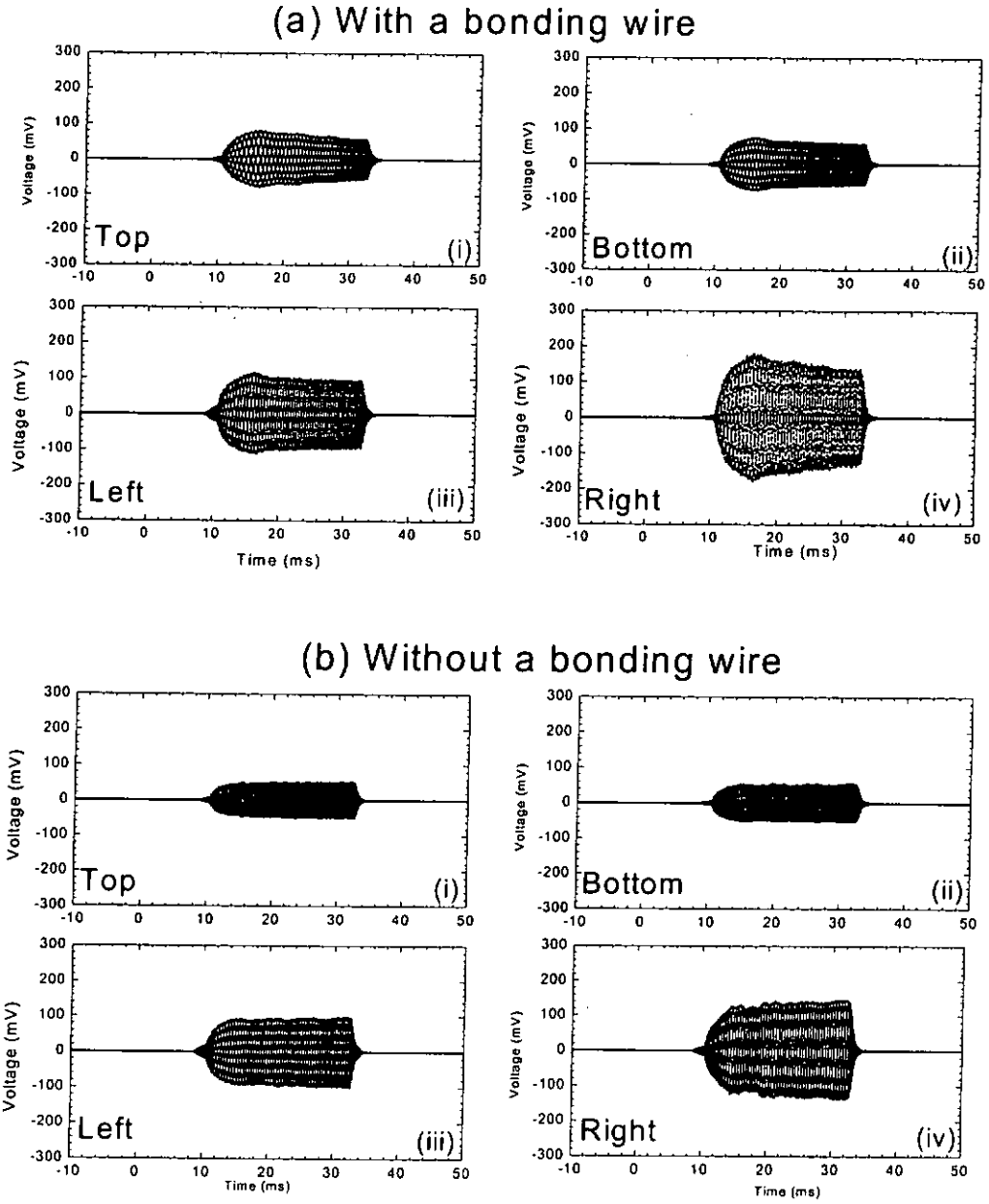

Fig. 4.4 High frequency signals captured by a E-type sensor with a high pass filter (62.5 kHz cut-off frequency) under the following bonding conditions: (a) with a bonding wire ;(b) without a bonding wire . The ultrasonic power dial setting is 3.1.

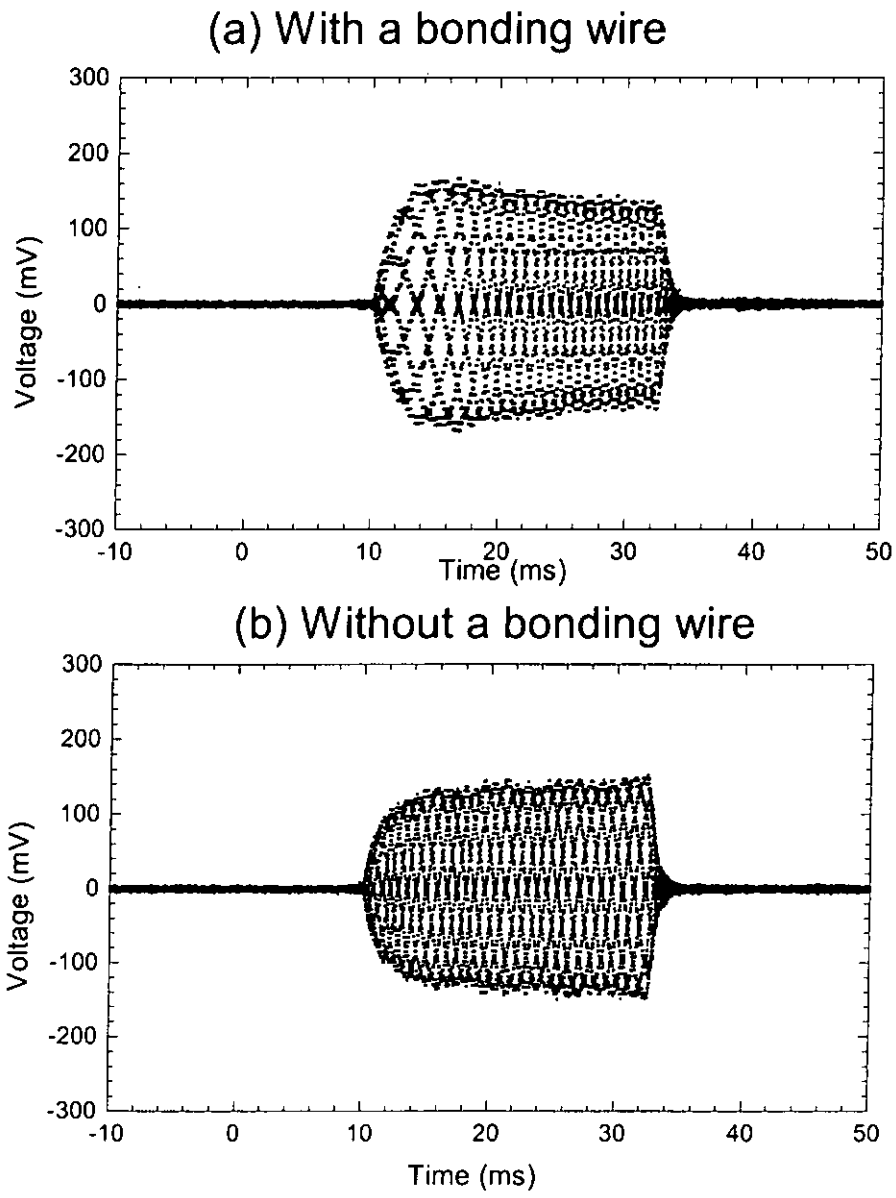

Fig. 4.5 High frequency signals captured by a A-type sensor with 62 kHz cut-off frequency high pass filter (a) with a bonding wire and (b) without a bonding wire. The ultrasonic power dial setting is 3.1.

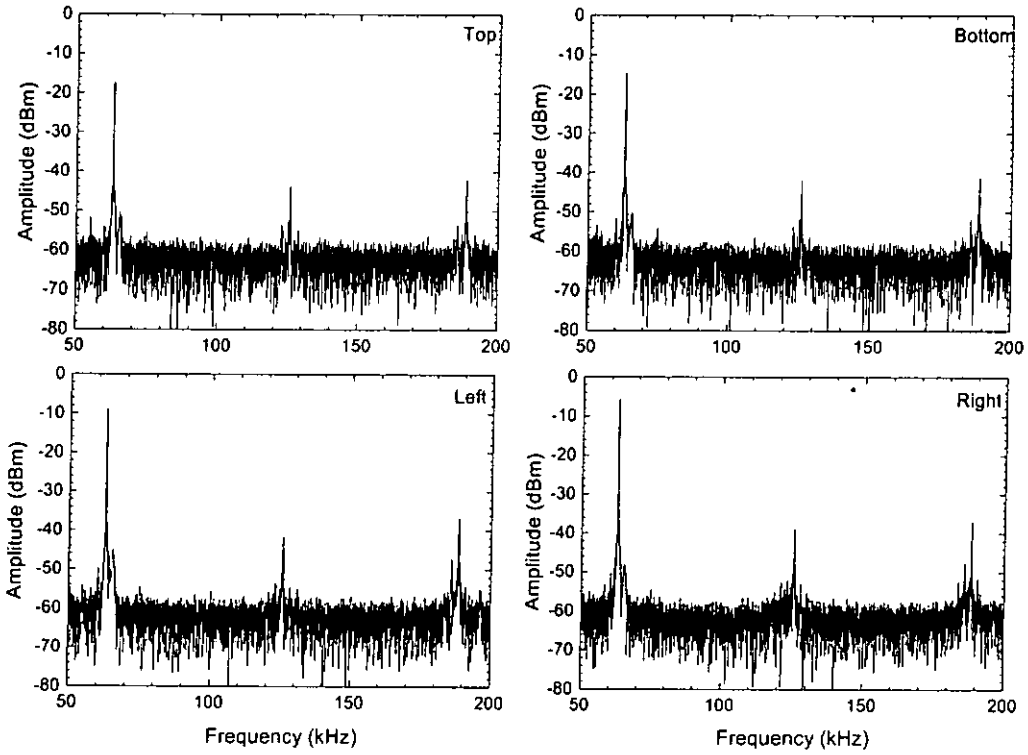

Fig. 4.6 The FFT spectra of outputs from the four sensors (with a bonding wire) (fig. 4.4).

4.4 Sensor output at various power dial settings

Ultrasonic power is one of the critical parameters in an aluminum wire bonding process. Too low an ultrasonic power will result in a bond that does not stick, excessive ultrasonic energy will cause cratering.

The bonding parameters (such as the bonding force, bonding time) of the bonder is kept constant except the ultrasonic power dial setting. The power dial setting is varied from 0 to 5 and using the left electrode of E type sensor to capture 100 signals from good bonds for each power setting when the bonder is operated with a bonding wire. The sensor peak to peak voltage output amplitude is the mean of 100 samples. The evaluation of the good bond will be discussed in Chapter 6.

The amplitude of the left sensor output as a function of the ultrasonic power supply dial setting is shown in fig. 4.7. When the ultrasonic power setting is zero, the amplitude is zero. As the ultrasonic power setting increases from 0.5 to 3; the sensor output also increases linearly. As the power setting increases from 3 to 4, the sensor signal only increases slightly probably due to more input energy has transferred to the sample. The sensor output increases again when power increases from 4 to 5. The power settings are given in peak-to-peak values. This graph indicates that the optimum ultrasonic power is between 3 – 3.5 which agreed with the

recommend values from the supplier of the transducer. In the pull tests reported in the Chapter 6, it is also found that good quality bonds are produced with the power settings between 3 – 3.5.

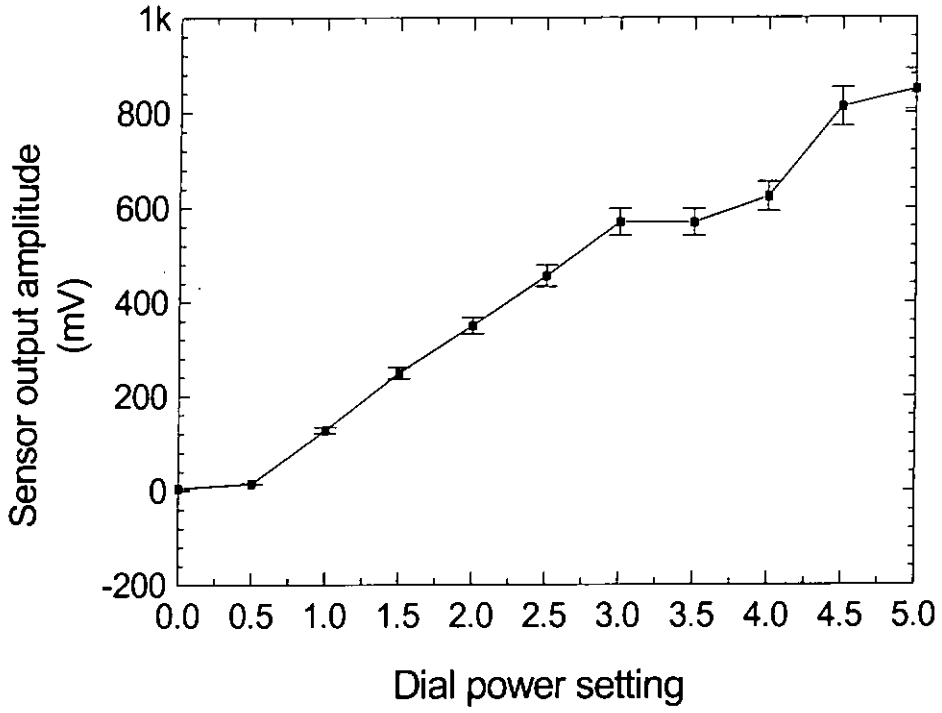

Fig. 4.7 The variation of ultrasonic power dial setting with the absolute value of the sensor output.

Chapter 5

Calibration of sensors

5.1 Introduction

Calibration is the process of applying a standard or known value of an input variable to an instrument and measure the output variable as a function of the input variable. Once the relationship between the input and output is calibrated, the calibration factor can be used to infer the value of an unknown input variable in other measurements. If the instrument can be characterized by a linear input/output relationship, the slope of this line is called its sensitivity and carries with it the units of the output signal / input signal.

In this chapter, methods for calibrating force measured by the sensor are presented. The first method is to use a back-to-back calibration by substitution to find the sensitivity of the sensor. Two sensors are installed in the ultrasonic wire bonder. The first sensor A is sandwiched between the piezoelectric driver and the concentrator horn and the second sensor B is embedded in the workchunk underneath the package. By a comparative method, the relationship between outputs from sensor A and sensor B can

be found. Sensitivities of the top and bottom electrode pair of sensor A to impact force are obtained.

5.2 Back-to-back calibration by substitution

5.2.1 Methodology

Using a traditional back-to-back calibration [41], sensor B is taken out from the workchunk and mounted back-to-back with a Brüel & Kjær type 8305 working standard accelerometer. The input acceleration provided by a Brüel & Kjær type 4809 shaker to sensor B and the standard accelerometer is identical. Consequently, the ratio of their sensitivities is simply the ratio of their output voltages.

The accuracy obtained with the back-to-back calibration method is improved by using the substitution technique, which is shown in fig. 5.1

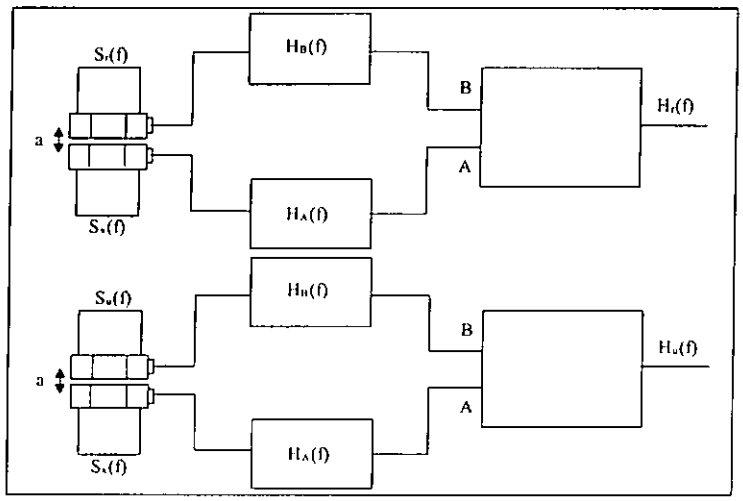

Fig. 5.1 The principle of back-to-back calibration by a substitution method.

Calibration by substitution involves making two back-to-back measurements. Initially, the transfer function* between the working standard accelerometer and a Brüel & Kjær type 4371 standard reference accelerometer is measured and stored. Then, the transfer function between the sensor and the working standard is measured and stored.

During the two measurements, the working standard accelerometer remains fixed to the shaker head, while the standard reference accelerometer and sensor B are subsequently mounted. The sensitivity of sensor B is then calculated as follows:

$$\frac{S_u(f)}{S_x(f)} * \frac{S_x(f)}{S_r(f)} = \frac{H_u(f)}{H_r(f)}, \qquad (5.1)$$

or

$$S_u(f) = S_r(f) * \frac{H_u(f)}{H_r(f)}, \qquad (5.2)$$

where $S_u(f)$, $S_r(f)$ and $S_x(f)$ are the sensitivities of the sensor, the standard reference accelerometer and the working standard accelerometer. $H_u(f)$ is the transfer function between the sensor and the working standard accelerometer.

*Transfer functions — The key mathematical elements in a block diagram denoting the transformation of input to output for that block. Transfer functions are usually Laplace or Fourier transforms of linear differential equations relating inputs and outputs [42].

$H_r(f)$ is the transfer function between the standard reference accelerometer and the working standard accelerometer.

The ratio $H_u(f) / H_r(f)$ is given by an equalized frequency response function. This is a post-processing function of the analyzer which calculates the complex ratio between the measured and the stored data.

Merits of a back-to-back calibration by the substitution method are the following:

(1) It cancels the systematic errors contributed by the electronics.

(2) Only recalibrations of the standard reference accelerometer and the precision attenuator are needed.

(3) Many mounting configurations are possible because the device under test is mounted on an adapter plate or working standard, not directly on the reference transducer.

5.2.2 The setup of the calibration

Configuration of the sensor calibration is shown in fig. 5.2. The instruments of this calibration system are manufactured by Brüel & Kjær. The system uses a type 4809 shaker connected to a type 2705 power amplifier. The power amplifier is driven by the signal generator built into a type 3022 signal analyzer unit. The type 4371 standard reference accelerometer or sensor B is mounted on top of the type 8305 working standard accelerometer which is mounted directly onto the shaker table. The output signals from sensor B and other accelerometer are fed separately into the analyzer and analyzed by a computer.

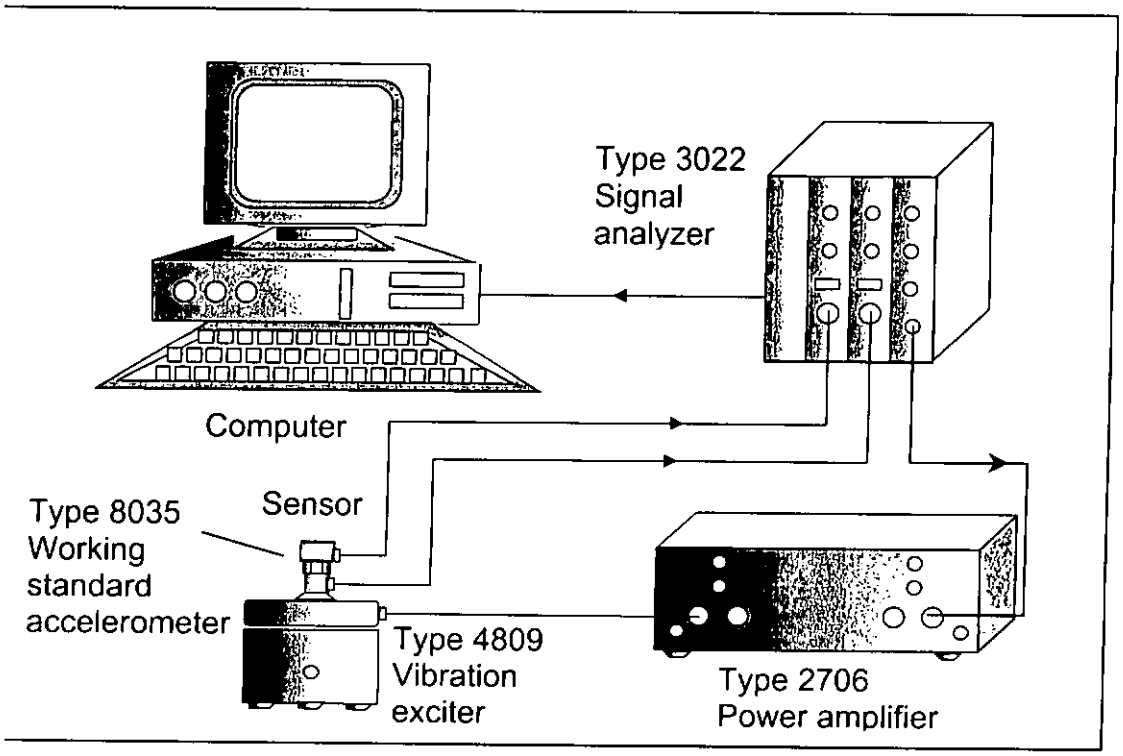

Fig. 5.2 The structure of the sensor calibration system.

5.2.3 The results of calibration

The transfer function H_r (f) between the type 4371 standard reference accelerometer and type 8305 working standard accelerometer and the transfer function between sensor B and the working standard accelerometer, H_u (f) were measured.

Sensor B has been fabricated using two different kinds of piezoelectric materials. The first sensor B1 consists of a 13×8×0.8 mm^3 lead zirconate titante PZT-5H as sensor (fig. 5.3). Two pieces of 57.5×35×12.7 mm^3 aluminum blocks secured by screws were used to fix and pre-stress the sensor and formed the housing of the sensor. The sensor, including its housing, was mounted on top of the working standard accelerometer that was directly affixed to the shaker table. The frequency response of the sensors and accelerometers are shown in fig. 5.4.

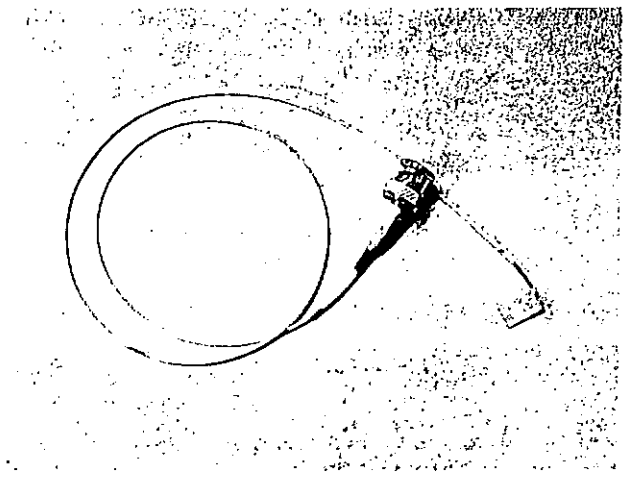

Fig. 5.3 The PZT-5H sensor.

A linear frequency range of 0-3.2 kHz is used and the gain is 10 during the calibration. In fig. 5.4a, the y-axis represents the acceleration of the working standard accelerometer in a logarithm scale. Fig. 5.4a shows that the working standard accelerometer has a constant sensitivity in the selected frequency range. The response of it is quite flat. The value of the accelerometer at 608 Hz is 16.5×10^{-3} m/s^2. From a Fast Fourier transformation (FFT), the frequency range of the impact force is about 400 – 800 Hz and 608 Hz is approximately the centre of the frequency range.

For the PZT-5H sensor B1, there is a peak at 2.4 kHz which is the resonant frequency of the sensor and the Al housing. Output of sensor B1 is 10.9×10^{-3} V at 608 Hz as shown in fig. 5.4b.

Fig. 5.4c shows the ratio between output of sensor B1 and the working standard accelerometer. After processing, a flat curve from 0 to 1.6 kHz is found, then the response slightly increases around 2.8 kHz and finally drops. From this curve, the ratio is 1.08 V/(m/s^2) at 608 Hz. Then, using equation 3.3, the ratio multipled by the sum of mass of the aluminum block (=131.2 g) and the accelerometer (=40 g) gives the sensitivity of the sensor. The sensitivity of PZT-5H is found to be 184 mV/N.

$$\frac{mV}{F(inN)} = \frac{mV}{ms^{-2}} \times mass(inkg) \qquad (3.3)$$

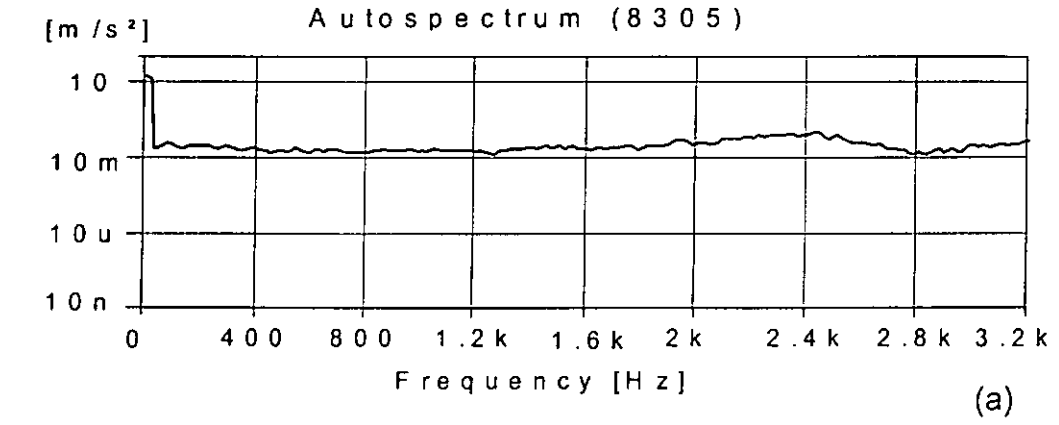

(a)

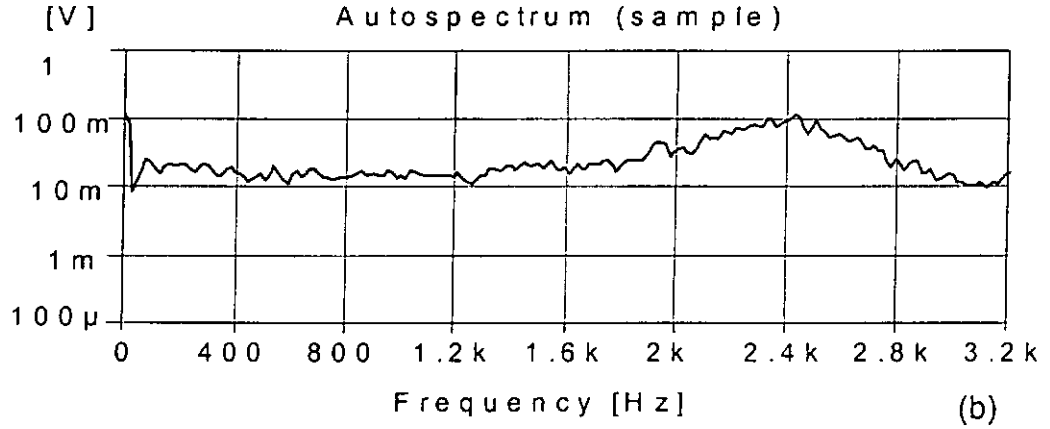

(b)

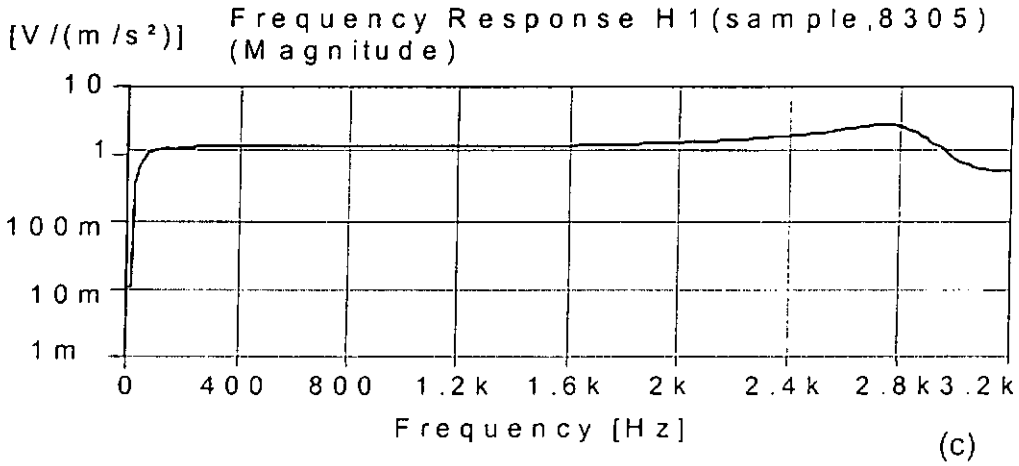

(c)

Fig. 5.4 The frequency response curve of (a) Type 8305 working standard accelerometer, (b) the PZT sensor and (c) (smoothed) ratio of the voltage output from the PZT sensor and the acceleration measured by the working standard accelerometer. I.e. Autospectrum (sample in (a)) / Autospectrum (8305 in (b))

5.2.4 Calibration of the PVDF sensor underneath the platform

A 13.8×11.5×0.11 mm^3 PVDF film was fabricated into a sensor B2 (fig. 5.5) and is placed underneath the chip carrier The PVDF sensor is placed into an aluminum housing. The housing is then mounted on top of the working standard accelerometer for measuring of the transfer function. The mass of the aluminum case and the standard accelerometer are 131.2 g and 40 g, respectively.

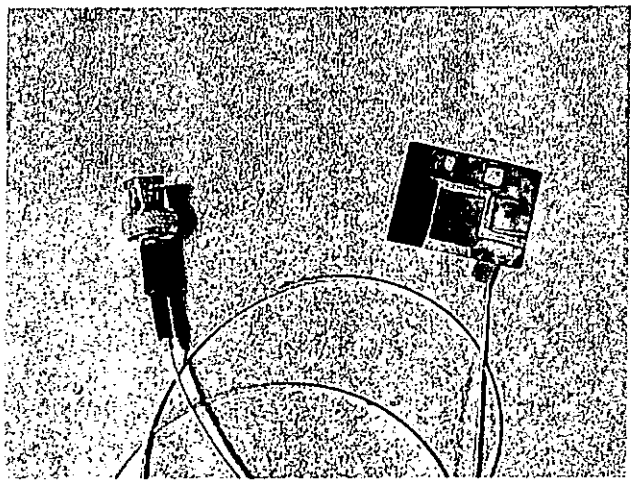

Fig. 5.5 The PVDF sensor.

Fig. 5.6a indicates that the frequency response curve of the working standard accelerometer is quite flat in the range of 0 to 3.2 kHz. The value is about 29.3×10^{-3} m/s^2 at 608 Hz. The frequency response curve of the PVDF sensor is shown in fig. 5.6b. From the figure, it can be observed that there is a resonant peak at 2.4 kHz. This curve has some ripples because

the aluminum housing is in intimate contact with the sensor set the housing in resonance and the vibrating film. The voltage output from sensor B2 is 6.72×10^{-3} V at 608 Hz.

Fig. 5.6c is the ratio of the frequency response curves of the sensor to the working standard accelerometer which is the sensitivity of the sensor. The sensitivity of the sensor is 229 mV/(m/s^2) or 39.2 mV/N at 608 Hz. It is also found that for f > 2 kHz values of the sensitivity depend on the frequency.

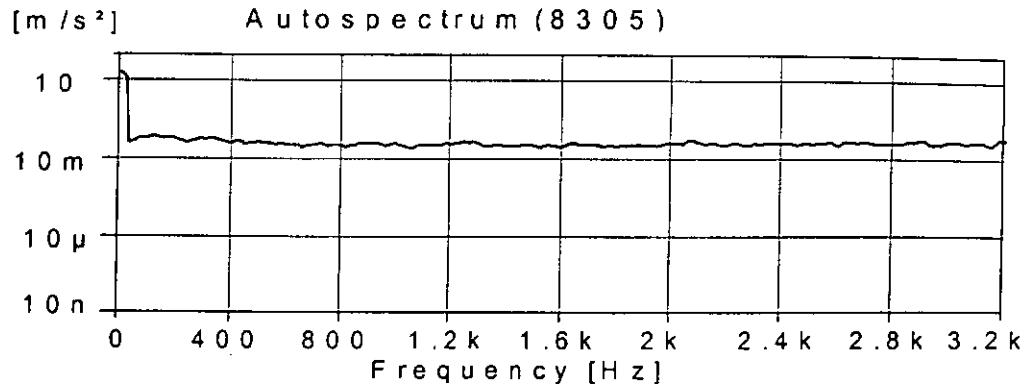

(a)

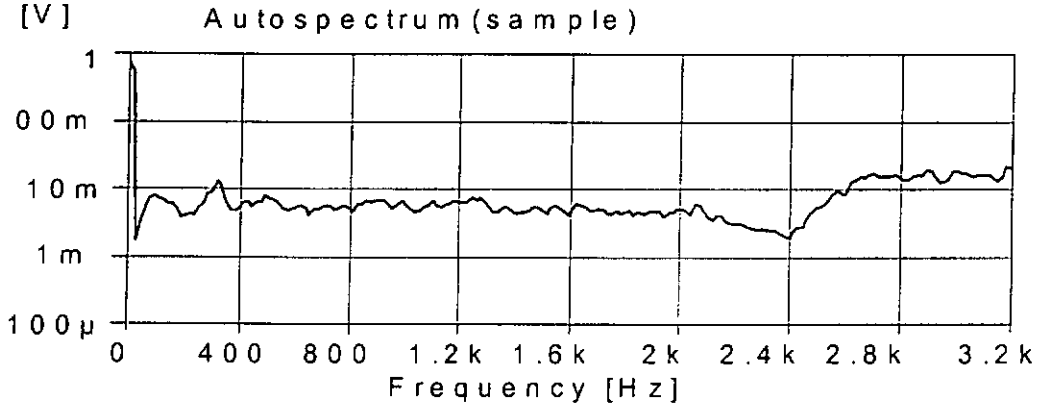

(b)

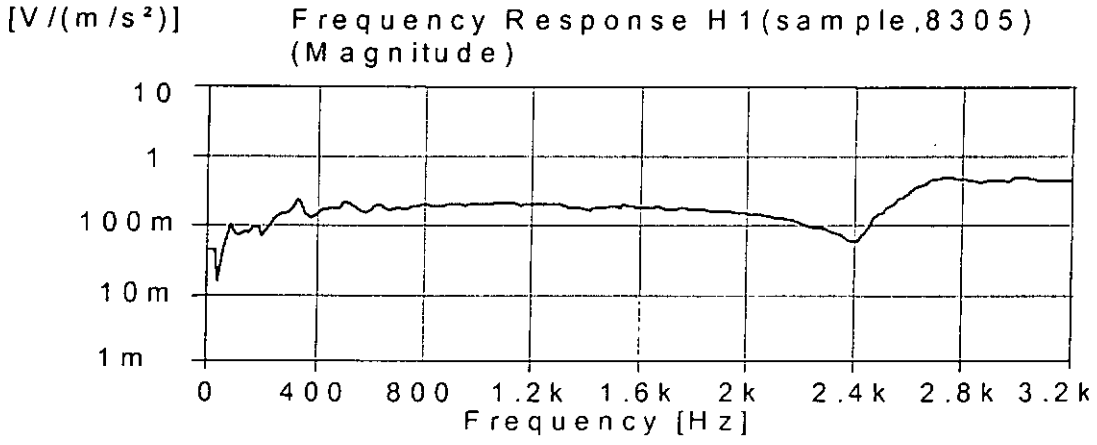

(c)

Fig. 5.6 The frequency response curves obtained with (a) type 8305 working standard accelerometer, (b) the PVDF sensor and (c) the ratio of the sensor to the working standard accelerometer.

5.3 Calibration by using a strain gauge

5.3.1 Methodology

The experimental setup of the second calibration method is shown in fig. 5.7. A 13×8×0.8 mm^3 PZT-5H sensor (sensor B1) was embedded in the workchuck underneath the device to be bonded. The output signal of the sensor that contains information on the impact force, the ultrasonic amplitude and the bonding time is fed into a HP 54522A digital oscilloscope. A 2 mm-aluminum wire strain gauge with gauge factor of 2 was also affixed to the solid horn of the ultrasonic wire-bonding transducer and used to measure the force information during bonding. The signal detected by the wire strain gauge is input to a Measurement Group, model 3800 wide range strain indicator, which is connected to another channel of the HP 54522A oscilloscope. The oscilloscope is linked to a desktop computer that can record, store and analyze the measurement data [43].

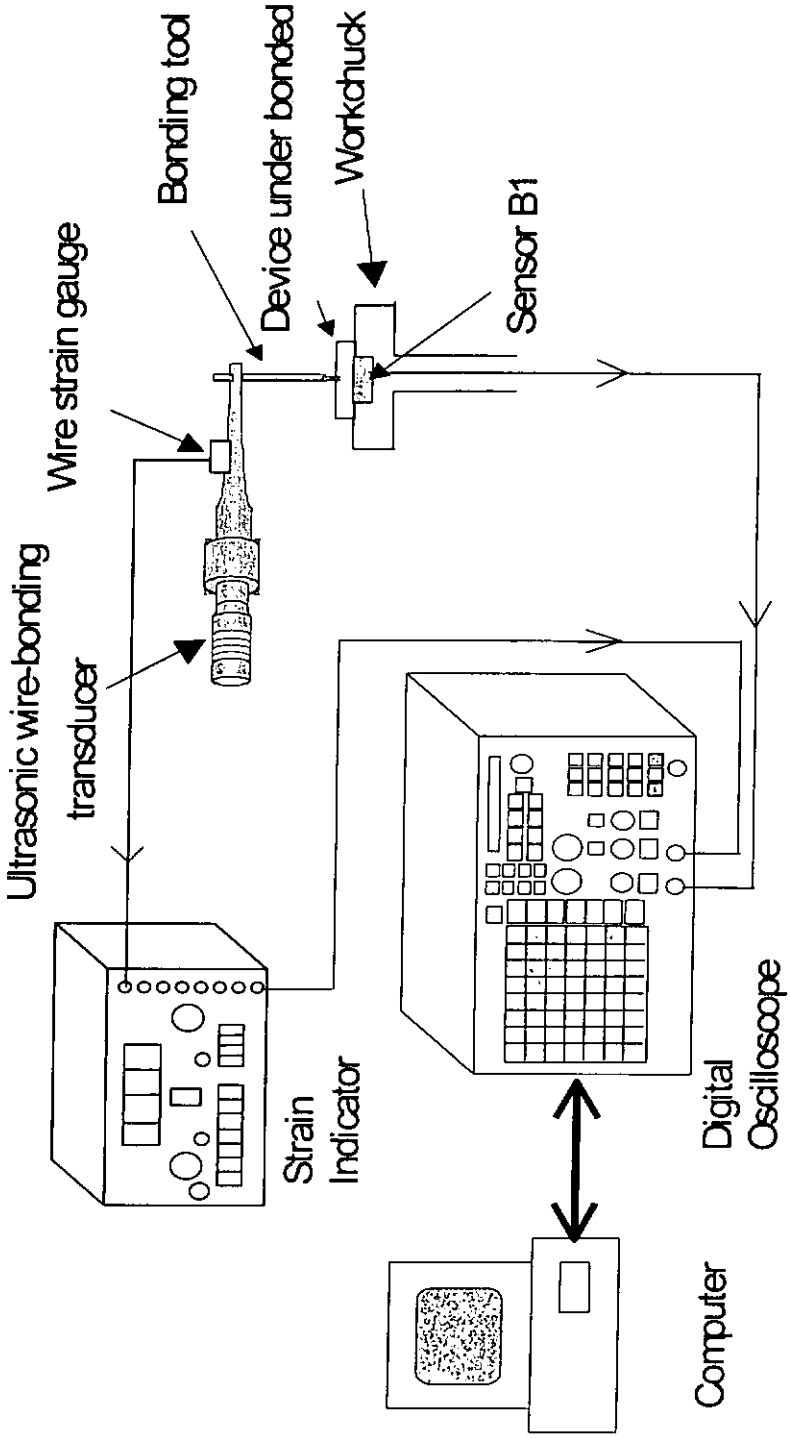

Fig. 5.7 The experimental setup of wire strain gauge and sensor B1.

5.3.2 Wire strain gauge signal

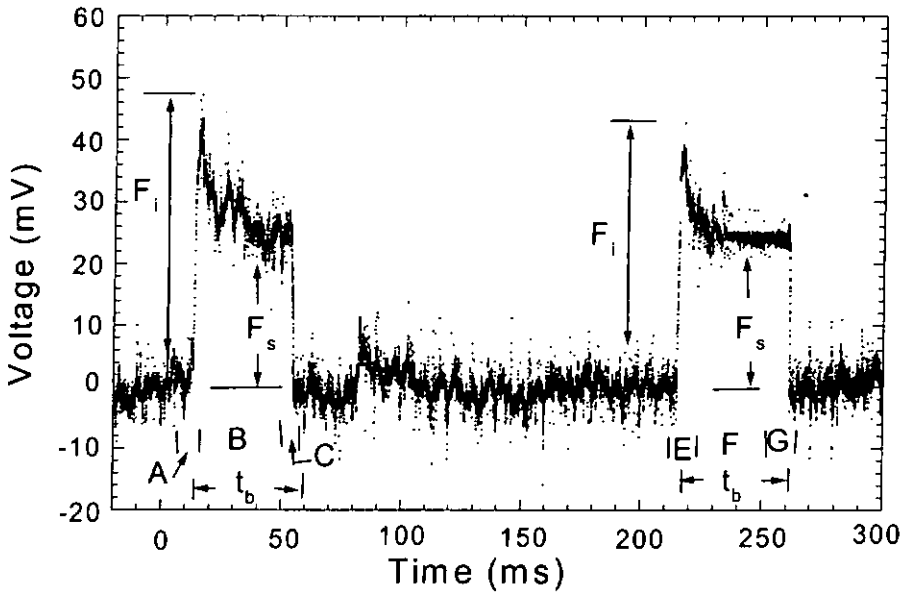

Fig. 5.8 The output signal detected by the wire strain gauge.

Fig. 5.8 shows the signal detected by the wire stain gauge for a bonded wire. It consists of three regions — A, B and C. In region A, the dynamic impact force F_i is produced as the bonding arm touches down on the IC die. Then the bonding arm vibrates as the result of this impact force and after the vibration subsides, the bonding arm remains stationary and exerts a preset constant bonding force F_s on the surface in region B. The bonding arm lifts up from the surface in region C and the signal returns to zero. Afterwards, the bonding arm moves to the location of second bond in region D. In region E, F and G, they repeats the steps of region A, B and C.

To calibrate the strain gauge, the end of the horn was loaded with various known dead weights and the voltage output obtained is shown in fig. 5.9 as a function of the applied force. From the slope, the sensitivity of the strain gauge was 94 mV/N with are 1 % error for linear fit. Thus, the impact force of first and second bonds are found to be about 513 mN and 463 mN respectively, whereas the bonding force F_s is about 270 mN.

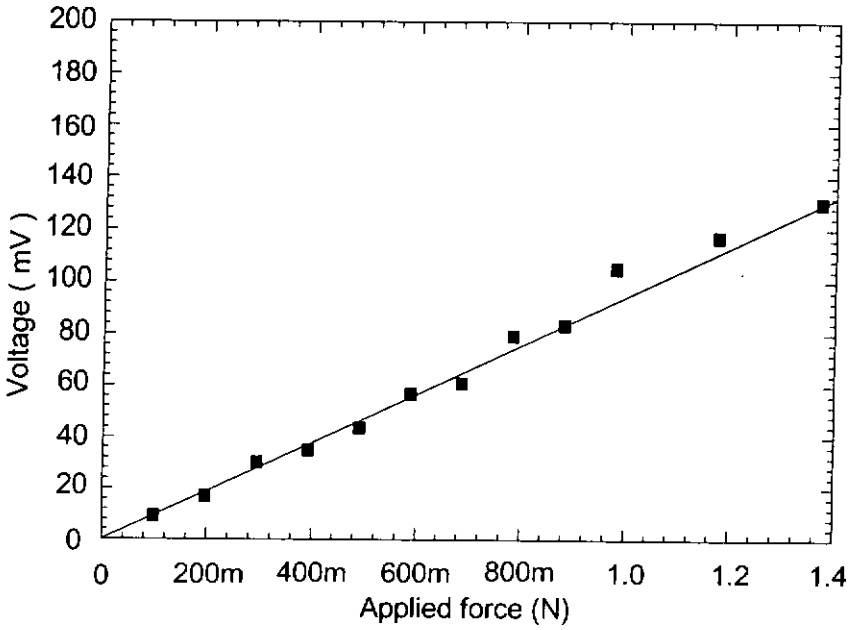

Fig. 5.9 The calibration curve for the wire strain gauge. The square and the line are the experimental data and the fitted line, respectively.

5.3.3 PZT sensor signal

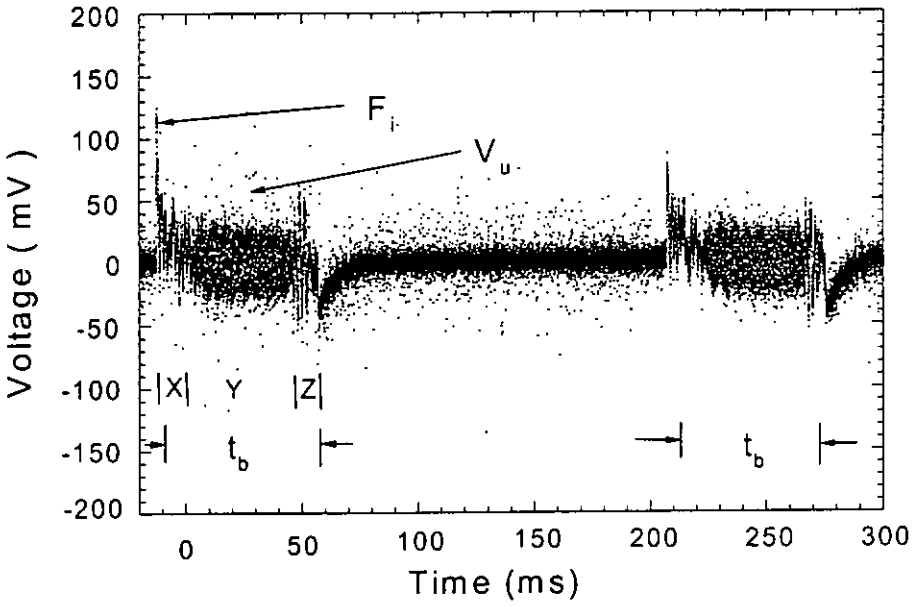

Fig. 5.10 The output signal detected by the PZT sensor.

The PZT sensor can detect low frequency and high frequency signals as shown in fig. 5.10. The signal also can be divided into three regions in each bond — X, Y and Z. Region X is when the bonding tool hits the IC die and vibrations are produced. After some time, vibration stops and ultrasonic energy (~ 60 kHz) for bonding the wire is applied in region Y. The solid horn lifts up from the die and set the IC in vibration in region Z. After completing the first bond, it moves to the site of the second bond and the above steps are repeated.

After the low frequency force signal in fig. 5.10 is removed by filtering, the ultrasonic amplitude is shown in fig. 5.11a. The ultrasonic energy deforms the wire and forms bond in stage Y. If the PZT sensor output is filtered to remove the ultrasonic signals, the first bond and second bond impact force signals are as in regions X and Z in fig. 5.11b.

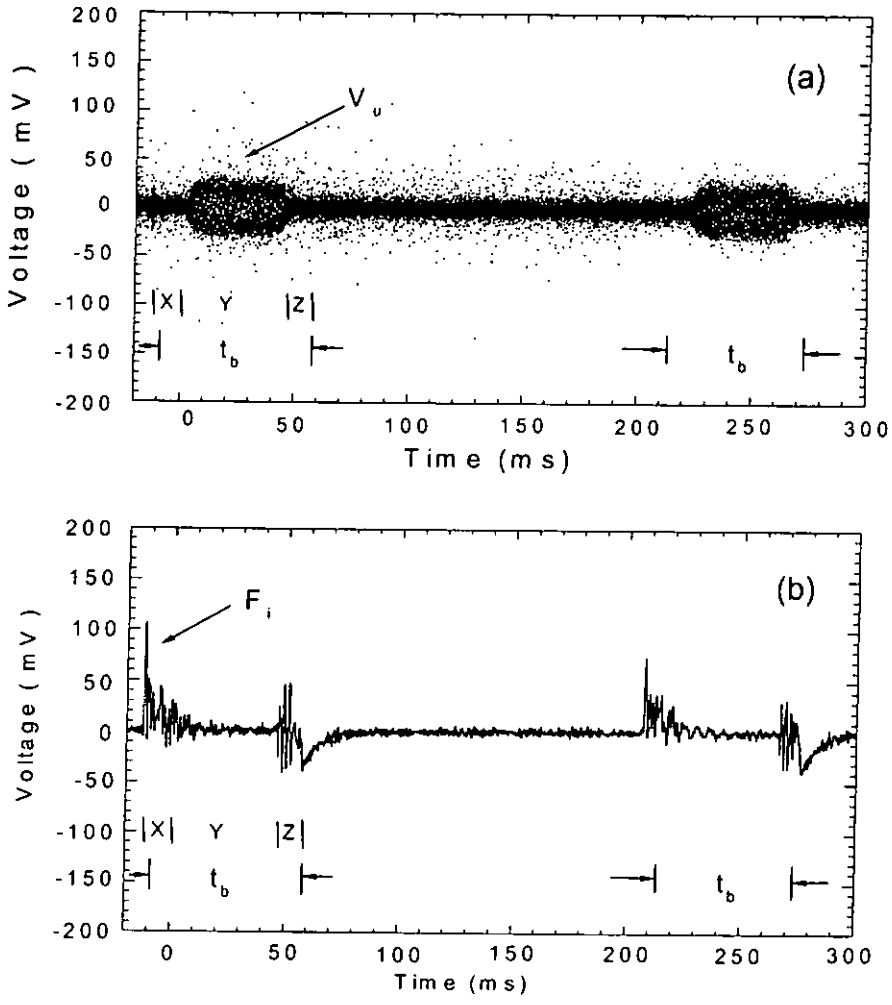

Fig. 5.11 The output signal of PZT sensor after (a) high pass filtered and (b) low pass filtered.

The signals captured from the wire strain gauge and the PZT sensor are quite different in shape. PZT sensor is more sensitive to the high frequency AC signals produced by the vibration of bonding tip but the wire strain gauge measures the absolute magnitude of the strain produced by the tip of the bonding tool. Combining outputs from both devices can give a complete measurement on both the impact and static forces. As the wire strain gauge is calibrated, by comparing the output voltages of it and the PZT sensor, the sensitivity of the PZT sensor is estimated to be about 212 mV/N.

In the back-to-back calibration method, the sensitivity of the same PZT sensor is found to be 184 mV/N. The relative error is about 15%. Using a strain gauge to calibrate sensor B the strain gauge needs to be calibrated first in each measurement as the strain gauge is quite sensitive to the change of environment conditions. Besides, the procedure to calibrate the strain gauge is quite complicate so we do not use this method to calibrate the PVDF sensor.

5.4 The correlation of the sensors

5.4.1 The experimental setup

Two PVDF sensors have been mounted in the bonding transducer as shown in fig. 5.12. One of them, sensor A with an E-type electrode pattern, is sandwiched between the piezoelectric driver and the concentrator horn and becomes an integral part of the bonding transducer for in-process monitoring. The other one, sensor B2, already calibrated, is embedded in the workchuck for calibrating the sensor A by a comparison method.

During the wire bonding process, sensor A and sensor B detects the same impact signal exerted by the bonding tool on the bond pad surface. Sensor A detects the bending moment of the concentrator horn due to the impact of the bonding tool on the bond pad surface. Sensor B2 detects the reaction force of the bonding tool while it hits the platform.

After signal capturing, the output signals from the two sensors are fed into the two channels of a digital oscilloscope HP 54522A. Profiles of sensor outputs are then stored by the computer for further analysis.

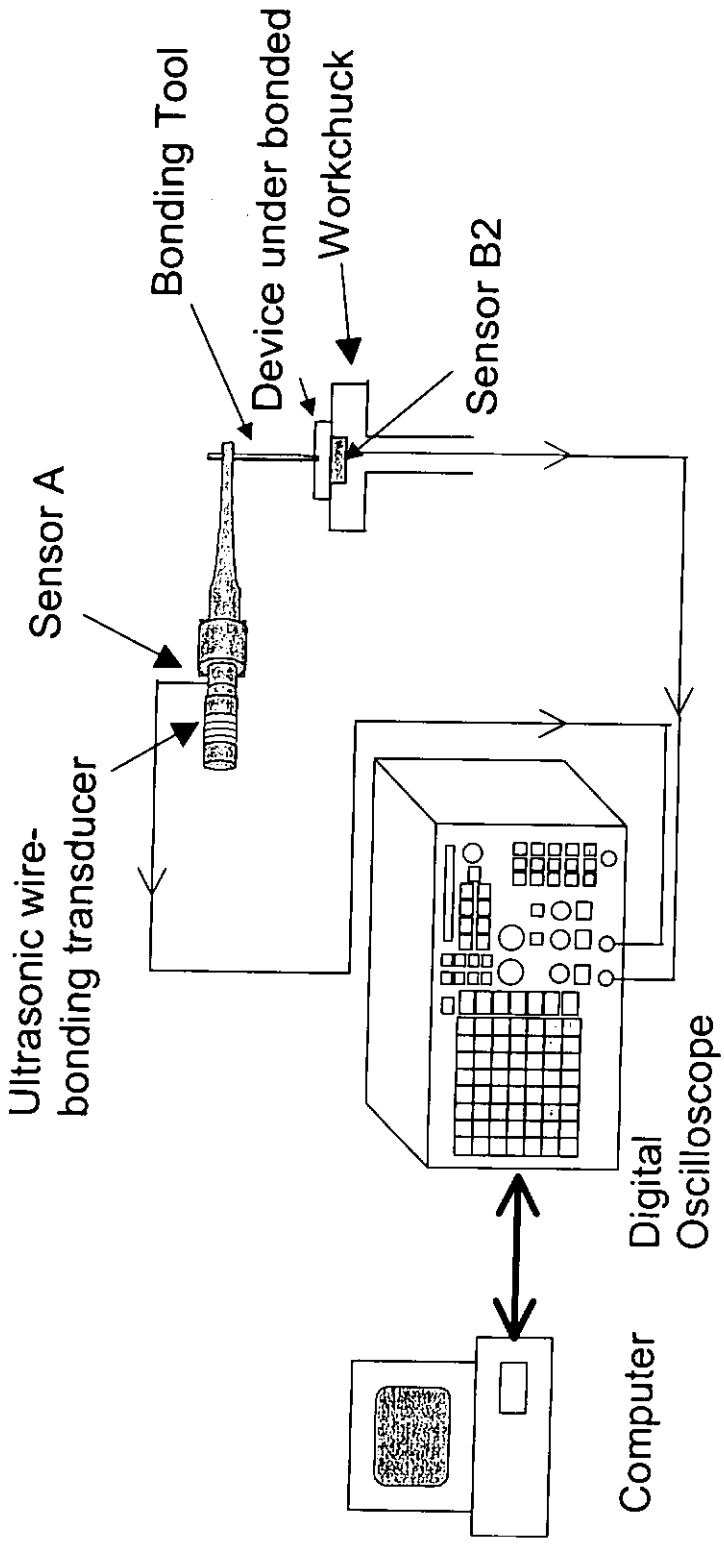

Fig 5.12 Schematic diagram of finding correlation between two sensors.

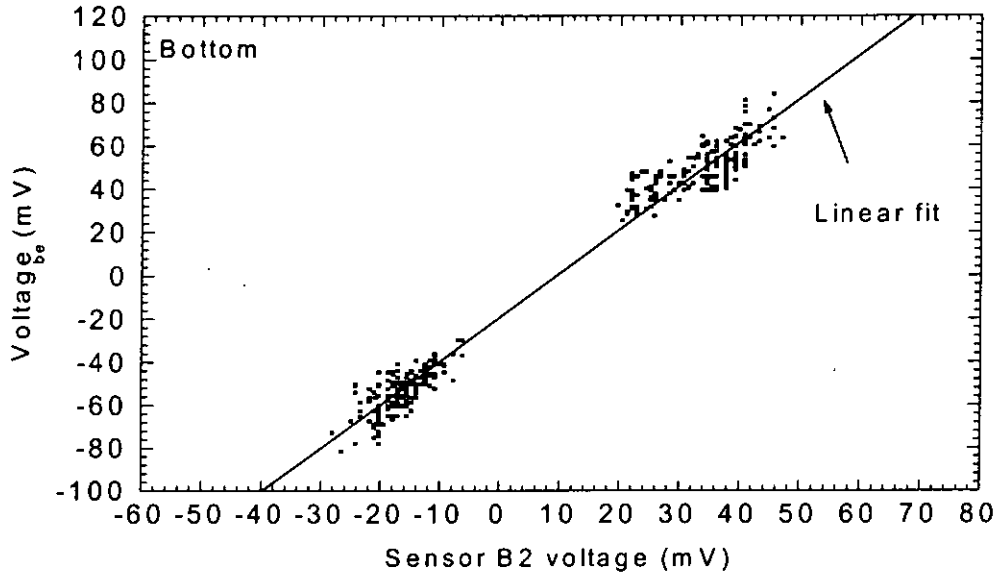

(a)

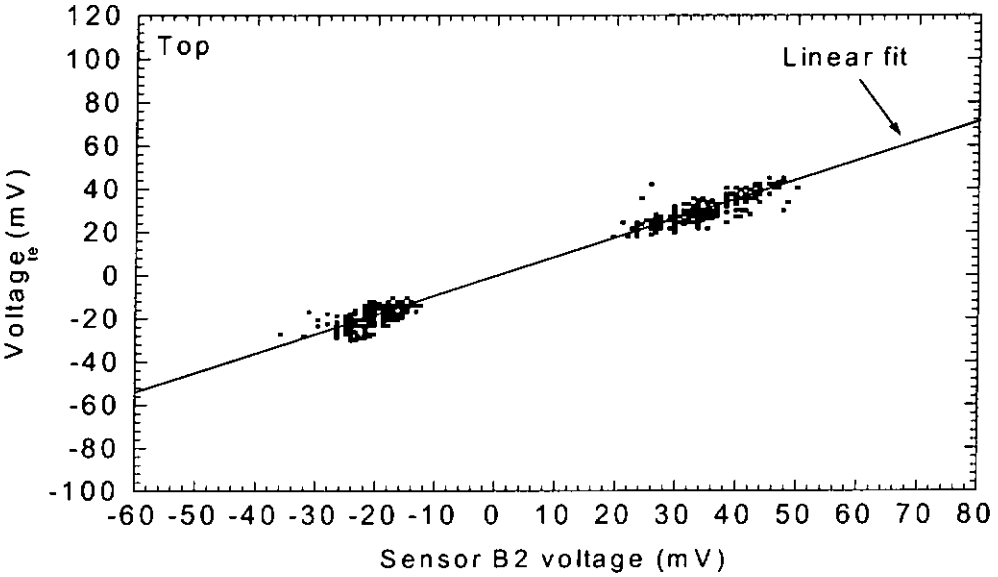

(b)

Fig 5.13 The voltage of sensor A versus that of sensor B2 as the bonding tool during touch down (+ve x-axis) and lift off (-ve x-axis). The equation of linear fitted curve in (a) –21.6 mV+1.9 V_{cs}, (b) –940 μV+ 0.9 V_{cs}. The subscripts be, te and cs represent the bottom and top portion of sensor A and sensor B2, respectively.

5.4.2 Results and discussion

To compare signals from the two sensors, the operation parameters of the bonder is programmed in a normal bonding condition except that the bonding wire is missing. This is because the impact force signals transmits better into the platform in the absence of the wire. To measure the impact force produced in the bonding process, only the top and bottom sensor pair is used. The upper and bottom portions of sensor A are calibrated separately. All four sensors in electrode pattern E have flat frequency responses as determined using the impedance analyzer HP 4194A and no resonance peaks are found in the frequency range of 200 Hz– 250 kHz.

The results for 100 samples are obtained and plotted in a graph and shown in fig. 5.13. The slope of linear fitting curve represents the sensitivity of the specific electrode area of the sensor. Using fast fourier transformation (FFT), the frequency range of the measured impact force is about 400 – 800 Hz. The sensitivity of the bottom and the top electrodes are approximately 52.8 mV/N and 34.2 mV/N at 608 Hz, respectively. 608 Hz is approximately the centre of the frequency range. From this value, the amplitude of impact force can be estimated.

Chapter 6

Bond quality measurement

6.1 Introduction

To distinguish whether a wire-bond is good or not, some bond quality indicators need to be defined. There are many parameters that may affect the bond quality. Ultrasonic power, bonding time and bonding force are known to be critical factors in aluminum wire bonding.

A higher ultrasonic power will result in a shorter bonding time. Although it can increase the production yield, it also increases the chance of bond failures due to cratering.

6.2 Pull test

The wire bond pull test is one of the established method for assuring the quality of the wire bonding operation. It was recommended for the evaluation of the strength of wire bonds in semiconductor devices in the 1960's. It can be divided into destructive bond pull test and non-destructive bond pull test. The destructive test is only useful on the wedge bonds or the wedge bond of a ball-wedge bond. The non-destructive test is frequently applied to reveal weak bond while avoiding damage to acceptable bonds. In a non-destructive bond pull test, the maximum applied force to the bond loop is limited to some predetermined value that is below the normal destructive pull test value.

To understand the principle behind the pull test, it is necessary to consider the geometrical configuration defining the variables given in fig. 6.1. The force in each wire, (f_{wt} and f_{wd}), at break, with a specified pull force, F, at the hook is [1, 44-47]:

$$f_{wd} = F\left[\frac{(h^2+\varepsilon^2 d^2)^{1/2}((1-\varepsilon)\cos\phi + \frac{(h+H)}{d}\sin\phi)}{h+\varepsilon H}\right] \qquad (6.1)$$

$$f_{wt} = F\left[\frac{(1+\frac{(1-\varepsilon)^2 d^2}{(H+h)^2})^{1/2}(h+H)(\varepsilon\cos\phi - \frac{h}{d}\sin\phi)}{h+\varepsilon H}\right] \qquad (6.2)$$

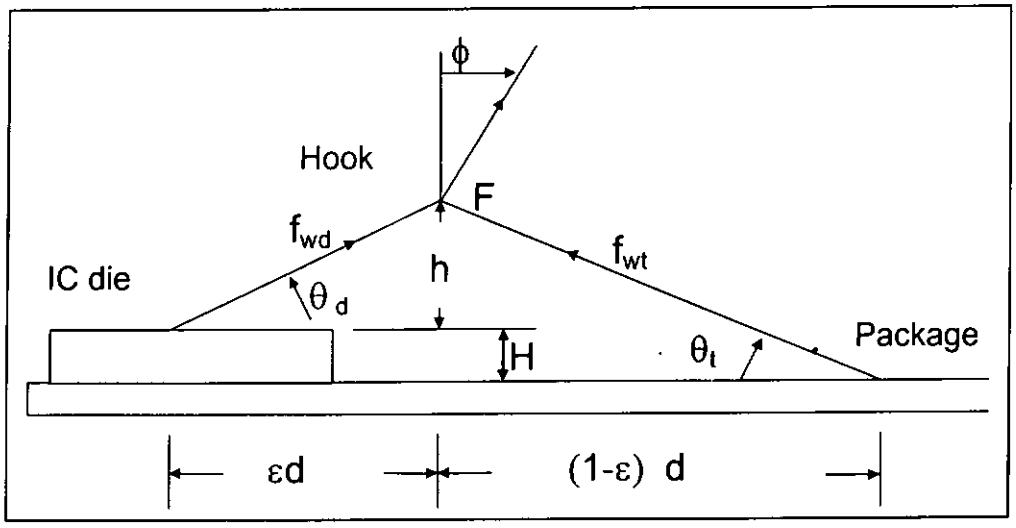

Fig. 6.1 The geometric variables for wire-bond pull test in the plane of the bond loop, as used in eqs (6.1) to (6.4) [45].

Assume the hook is vertically located at the center of the IC die and the package,

Then , ε=1/2, ϕ=90° and eq. 6.1 and eq. 6.2 become

$$F_{wd} = F\left[\frac{(4h^2 + d^2)^{1/2}(h + H)}{d(2h + H)}\right] \qquad (6.3)$$

$$F_{wt} = F\left[\frac{-h(4(h + H)^2 + d^2)^{1/2}}{d(2h + H)}\right] \qquad (6.4)$$

Where F is the specified pull force; F_{wt} is the wire break force at the package; F_{wd} is the wire break force at the die; d is the distance between the first bond (IC die) and the second bond (package); h is the height between the hook and the IC die; H is the height

between the IC die and the package; ε is the ratio of the hook location; ϕ is the angle between the pull force F and the normal; θ_d is the angle between the bonding wire and the IC die; θ_t is the angle between the bonding wire and the package.

Eqs. 6.1 to 6.4 show that the wire break force depends on the variables h, H, ε and d. In practice, h and H is smaller than 0.5 mm, d is about 1 mm and ε is 0.5 [.

In a wire-bond pull test, the pull force F applied to the hook will cause bond failure. Common modes of failure are the followings:

(1) First weld off – break at the bond – pad interface of the first bond.

(2) First neck break – at the heel of the first bond.

(3) Span break –the wire break at the location of the hook.

(4) Second weld off – break at the bond – pad interface of the second bond.

(5) Second neck break – at the heel of the second bond.

(6) Others – e.g. the first and second bond lift-off together.

6.3 Shear test

The shear test is more sensitive to the amount of interfacial weld area than the strength of the bond heel. The schematic diagram of shear test is shown in fig. 6.2.

In principle, the shear test is simple and consists of using some form of tool to apply a shear force on the side of a bond sufficient to push it off, and recording that force. The shear tool is a flat chisel and the dimension of the shearing edge is approximately 1 – 2 bond lengths. The shear tool is placed about 2.54 – 5 μm (0.1 – 0.2 mil) above the metallization bond pad and parallel to it. The shearing rate is within 0.25 – 6 mm/s^2 [35,48,49].

In a shear test, the shear force applied to the shearing tool will cause bond failure. The common modes of failure are the followings:

(1) Bond lift – Bond separated at bonding pad

(2) Bond shear –Wire material left on bonding pad

(3) Bonding pad lifted

(4) Cratering – Bonding pad lifted off taking portion of the underlying substrate material with it

(5) Wire shear – The shear tool is too high, only a portion of the bond removed

(6) Shear tool contacts substrate – Shear tool contacts bonding pad or substrate

Table 6.1 shows the range of shear force used to distinguish the bond quality. For shear force between 30 – 40 gf, it is considered as a good bond. The range of shear force for an average bond is 20 – 30 gf. When the shear force is less than 20 gf, it is then a poor bond.

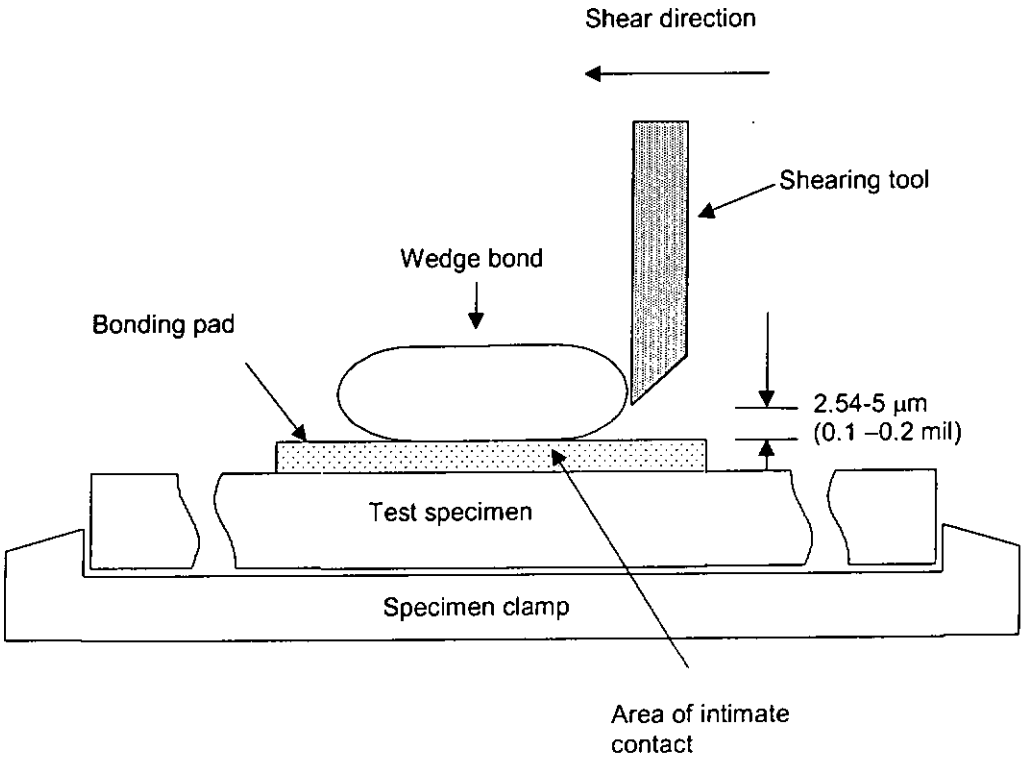

Fig. 6.2 The schematic diagram of the wire wedge bond shear test.

	Good bond	Average bond	Poor bond
Shear force (gf)	30 - 40	20 - 30	< 20

Table 6.1 The range of shear force for defining bond quality.

6.4 Visual inspection

Visual inspection is a basic method for bond quality evaluation. The inspector looks at the appearance of the bond and measures the bond width, bond length, wire tail, loop height etc (figs. 6.3 & 6.4). Occasionally, the inspection also includes the condition of the bonding wire, for example, whether the wire is damaged or not.

The bonding wire will deform after the bonding process. The weak point of the bond is located at the bond heel (bond neck). It is because the bond heel becomes metallurgically work-hardened and weakens as the bond deformation increases. To prevent this phenomenon, some criteria is necessary for optimizing the bond quality.

The deformed bond width is usually within 1.4 to 1.8 times the original wire diameter. In case the bond width is less than 1.4 times, the total area of the bond is too small and not strong enough for adequate bond adhesion and the bond will lift off easily. However, when the bond width is larger than 1.8 times, the perimeter of the bond becomes irregular and tends to be squashed especially in the heel of the bond.

In addition, if the length of wire tail is too long, it will cause short circuit. However, the bond will lift up easily if the length of wire tail is too short.

Therefore, it is necessary to find out the optimal acceptance criteria for all the measured parameters before measurements in order to bench mark the bond quality.

The merits of visual inspection are the followings:

(1) It is a non-destructive test that does not damage the bond.

(2) It is a convenient method for quality control.

(3) The measurements are simple and easy.

The disadvantages of visual inspection are the followings:

(1) The internal defects of the bond cannot be observed.

(2) The condition of the interface between the wire and bond pad cannot be observed.

(3) Poor adhesion between the wire and the bond pad cannot be visualized easily.

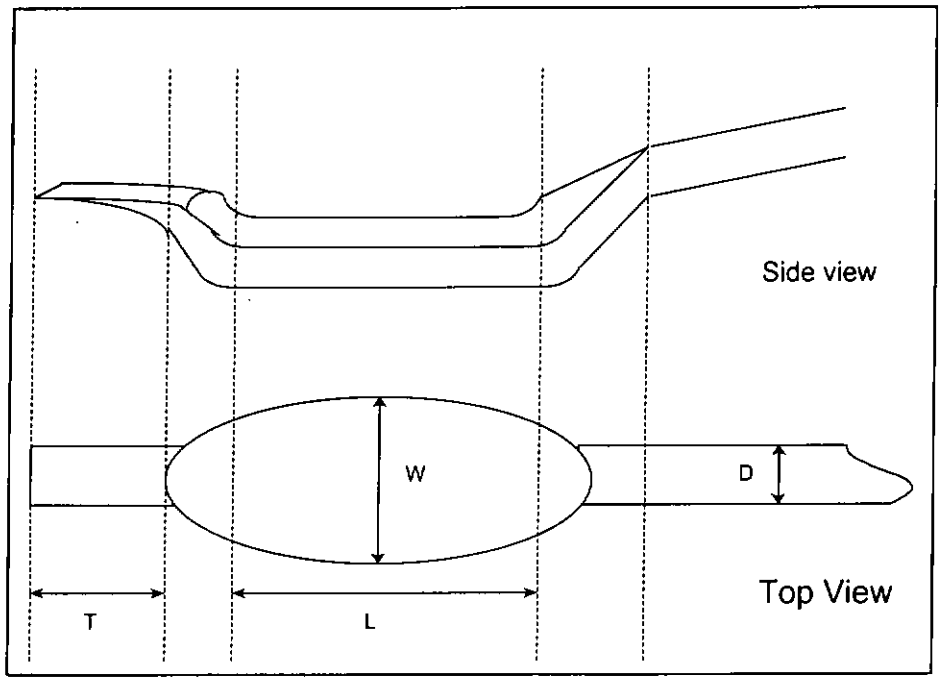

Fig. 6.3 A typical wedge bond , diameter of the wire is D. Bond width (W), bond length (L) and bond tail (T) are the measured parameters.

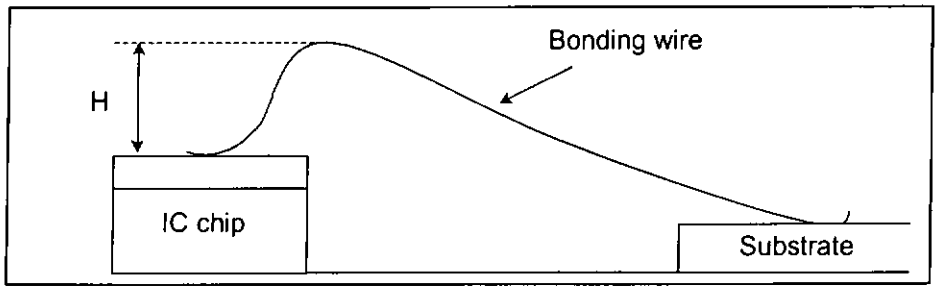

Fig. 6.4 A typical wire bonding interconnection between an IC chip and a substrate. The loop height (H) is measured.

6.5 Evaluation of the bond quality

The samples were fabricated by an ASM 500B computerized semi-automatic ultrasonic wire wedge bonder. The 31.75 μm (1.25 mil) diameter (Al – 1%Si with 1-4% elongation) bonding wire has 19-21 gf tensile strength and was supplied by Tanaka electronics Singapore Pte, Ltd. It acts as an interconnection between the 100×100 μm^2 Al evaporated bonding pads on the IC die and the Au plated bonding pads on the chip carrier. The horizontal distance between the two bonds is 2 mm, the vertical distance between two bonds is 0.55 mm and the height of loop is 0.3 mm.

The bonding time and bonding force is set at constant values of 30 ms and 27 gf, respectively. The sample groups are fabricated with various ultrasonic power settings from 3 V_{p-p} to 5.5 V_{p-p} in steps of 0.5 V_{p-p}. Each sample group has 100 bonds. Using a Nikon V-12A projector the deformed bond width is measured. A Royce Instruments System 550 tester can be used to perform the pulling test and shear test. In the pull test, a 76.2 μm diameter pull hook is used in pulling the wire until it breaks. Then, the pull force F is recorded and the location of the wire break point which is the weakest section of the wire under the pull test is also noted. In general, the break point of the wire is located near the heel of the first bond, second bond or span break. Then eqs. (6.3) and (6.4) are used to calculate the

actual pull force from the measured pull force F of the first bond failure mode and the second bond failure mode.

After the pull test measurement, the same tester is changed from a pull hook to a flat chisel-shaped shear ram. The edge of the shear ram is 228 μm. The shear force and the failure mode of each bond are recorded. Thus, the following figures are obtained.

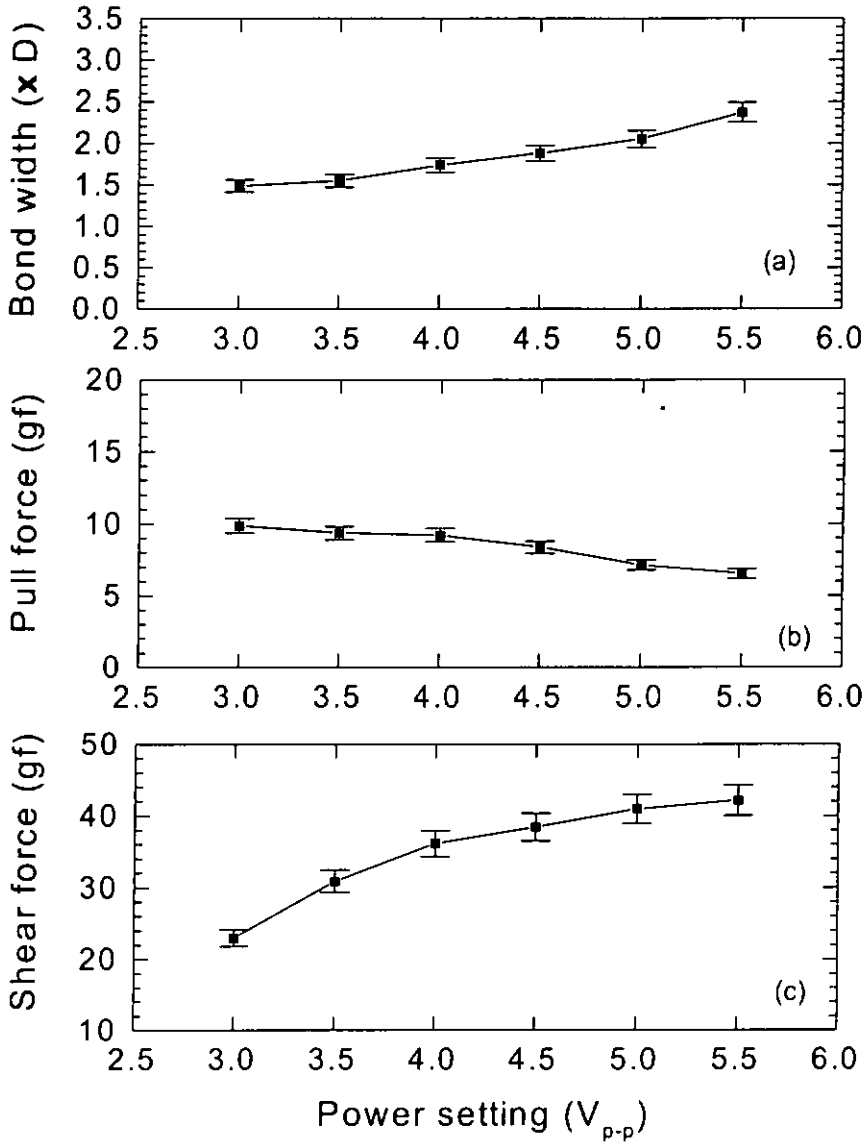

Fig. 6.5 Data from the first bond with 31.75 μm (1.25 mil) diameter Al wire on Al metallization (a) bond width; (b) pull force and (c) shear force on ultrasonic aluminum wedge bonds against power settings. Each point represents the mean of 100 bonds. All bonds are bond neck failure in bond-pull test and bond shear failure in bond-shear test. The error bar is ~ ± 5%.

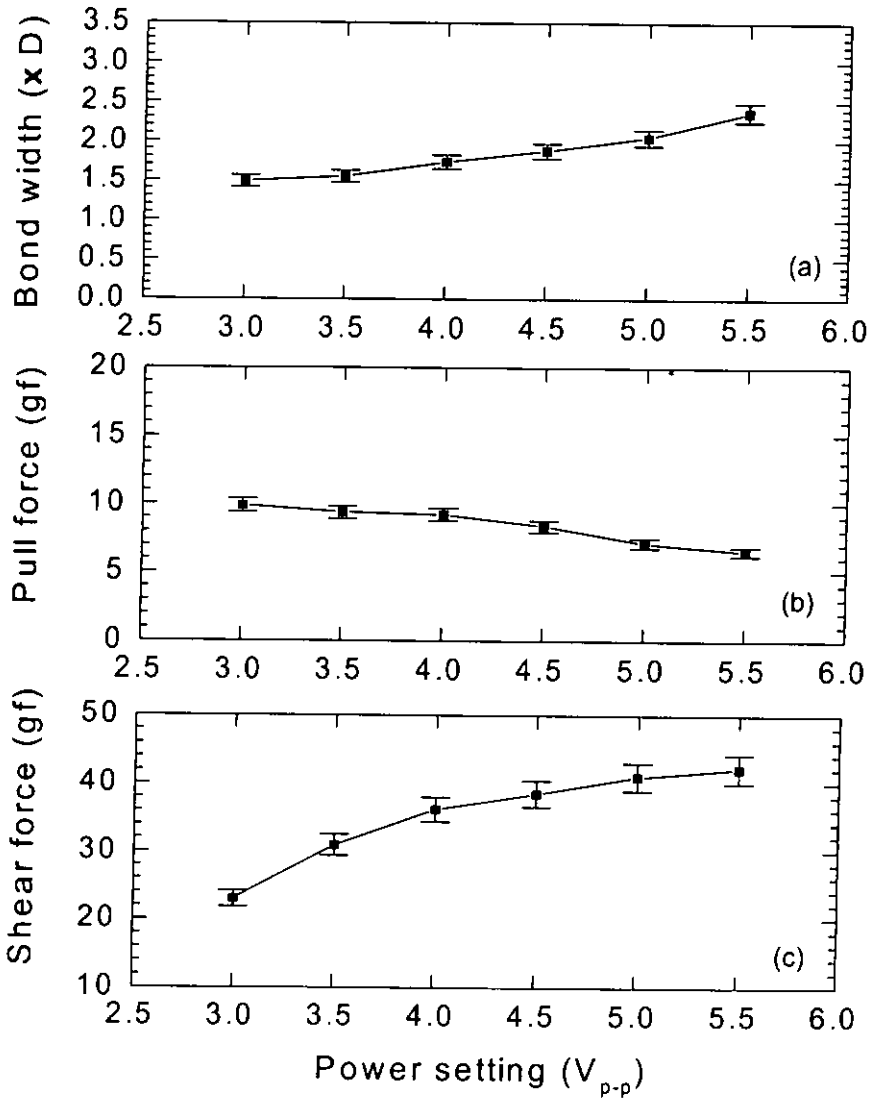

Fig.6.6 Data from the second bond with 31.75 μm (1.25 mil) diameter Al wire on Au metallization (a) bond width; (b) pull force and (c) shear force on ultrasonic aluminum wedge bonds against various power settings. Each point represents the mean of 100 bonds. All bonds are bond neck failure in bond-pull test and bond shear failure in bond-shear test. The error bar is ~ ± 5 %.

From figs. 6.5 and 6.6, it is seen that as the ultrasonic power increases, the bond width and the shear force increase but the pull force decreases for both kinds of ultrasonic bonds. The deformed bond width increases which implies that the thickness of the bond decreases and the tensile strength of the heel of the bond will be reduced. The pull test is particularly sensitive to the weakening of the bond heel. Therefore, the pull force decreases as the ultrasonic power and deformation of the bond increases. On the other hand, the shear test is completely independent of the condition of the bond heel. It is only sensitive to the actual amount of welded area. Therefore, the shear force increases as the ultrasonic power and deformation of the bond increase.

Comparing the bond strength of the first and second bond, it is found that the first bond is stronger than the second bond. The shear force test can substantiate this conclusion. In the first bond, bonding between the same material (Al-Al) is more reliable than bonding between different materials in (Al-Au) in the second bond [35].

Therefore, the definition of a good bond is one that has high shear force, with large weld area after shearing, has a high value of pull force and the bond width is about 1.5 to 1.7 times the diameter of the bonding wire.

6.6 Relationships between the impact force, ultrasonic amplitude ratio and the bond quality

With the piezoelectric PVDF sensor sandwiched between the driver and the concentrator horn, the bonding time, bonding force and ultrasonic power set at 25 ms, 27 gf and 3.1 $V_{p\text{-}p}$, respectively, the sensor output is recorded and stored by the computer. Bond width measurement, pull test and shear test are performed on these samples [50]. Correlations between the sensor output and the bond quality are then deduced.

The following figures show the sensor outputs from the top side (TS) electrode and from the left hand side (LHS) electrode. The corresponding SEM micrographs of the bonds after the shear test are also shown.

Fig. 6.7 shows the sensor profile for a typical good bond. The signal is observed at the fundamental frequency (62.5 kHz). At about 10 ms, the ultrasonic amplitude increases to a peak value V_p (at 15 ms) and then decreases to a steady value V_s. The SEM micrograph (fig. 6.8) shows that the "footprint" has a large weld area and 36.5 gf shear force is required to remove the bond.

Fig. 6.9 indicates an average bond which has a weaker adhesion to the bond pad. The sensor output is quite similar to the profile of a good bond except that peak amplitude tends to decrease slowly to a steady value in fig. 6.9a. Fig. 6.9b shows the force signal of an average bond. The "footprint" of an average bond has a relatively smaller welded area (fig. 6.10). The shear force is 27 gf.

Profiles from a poor bond are shown in figs. 6.11a & 6.11b. The ultrasonic amplitude profile does not show a distinguish peak followed by a steady value similar to that shown in fig. 6.8a. Besides, the impact signal is quite large in fig. 6.11b. The "footprint" clearly reveals that the welded area only cover the perimeter of the bond and no weld is formed in the center of the bond (fig. 6.12). The shear force is 16.5 gf.

In the missing wire condition, the sensor output is shown in fig. 6.13. The left (LHS) sensor gives an ultrasonic amplitude profile which contains no peak value at the initial interval and increases slowly to a steady value. The top (TS) sensor is relatively sensitive to the impact signal. A sharp impact force amplitude peak is observed.

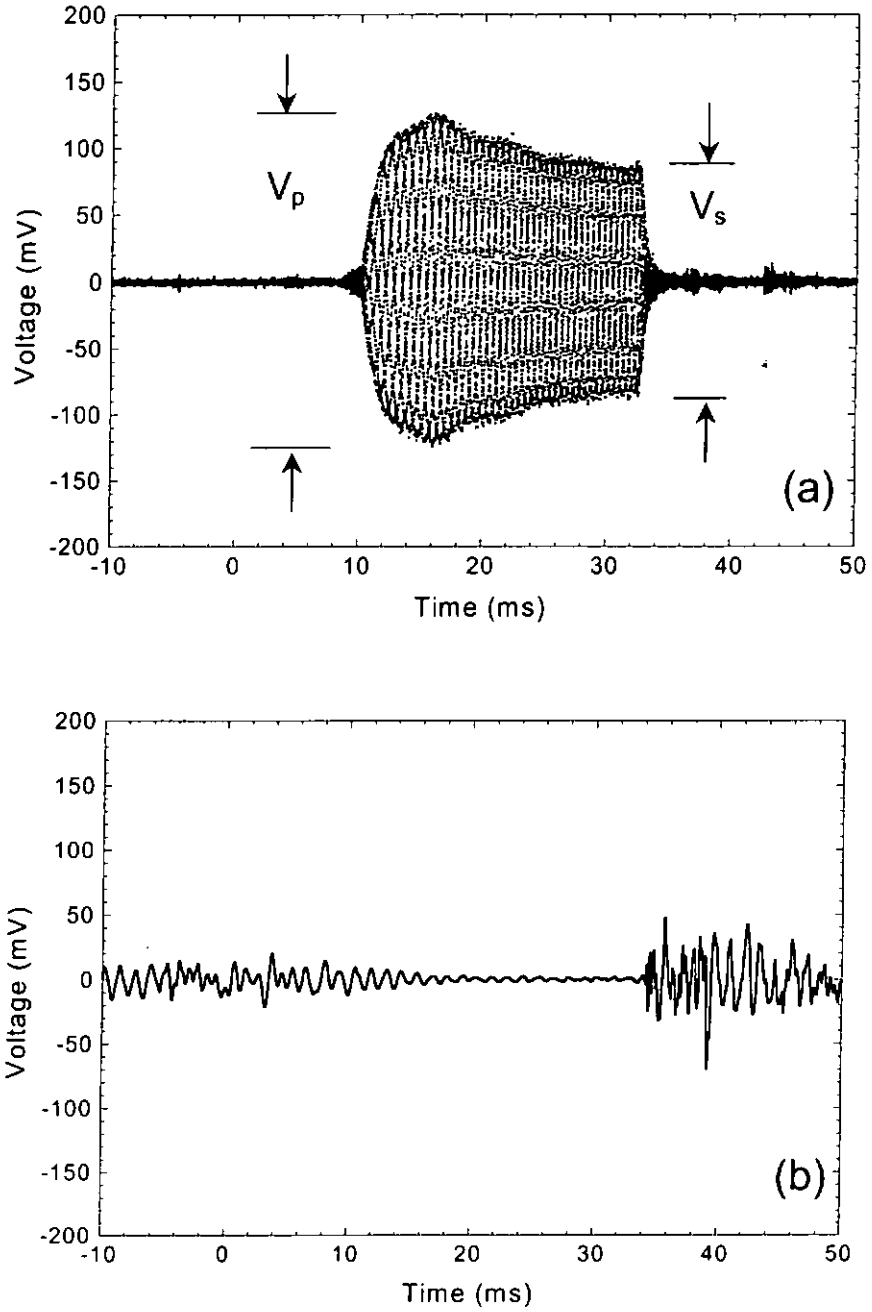

Fig. 6.7 Sensor output profiles for a good bond (a) from the left sensor using a high pass filter with 62 kHz cut-off frequency and (b) from the top sensor using a low pass filter with 1 kHz cut-off frequency. The fundamental frequency is 62.5 kHz.

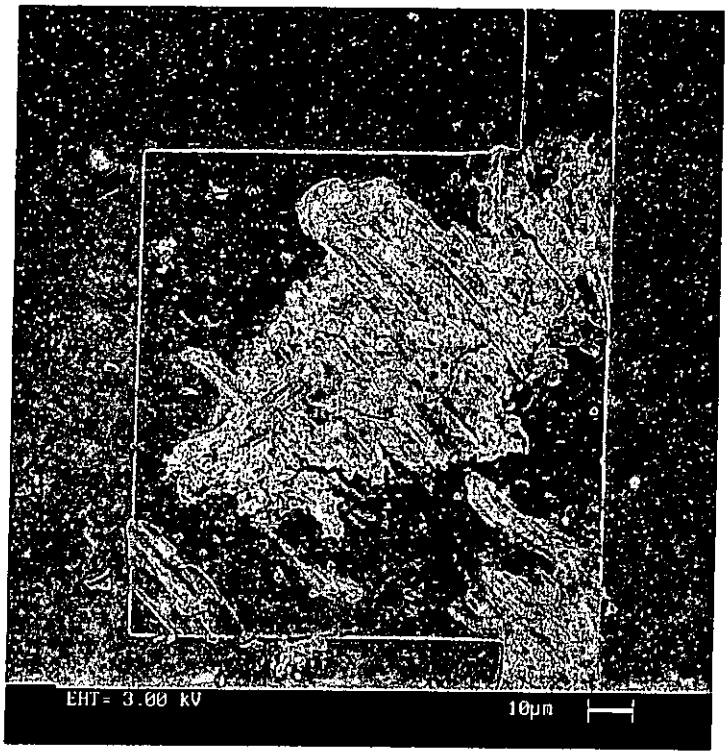

Fig. 6.8 The SEM micrograph of a typical good bond. The shear force is 36.5 gf.

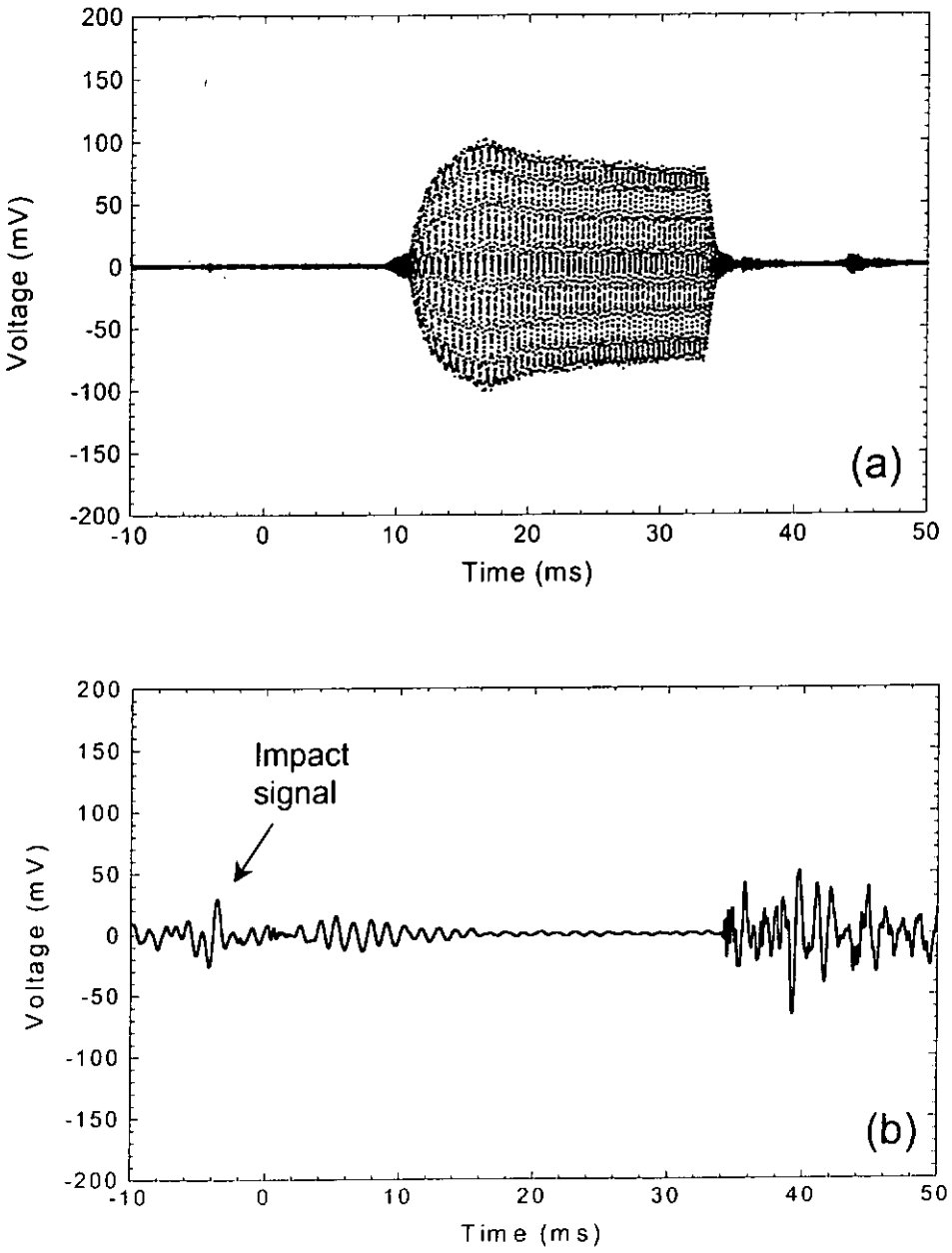

Fig. 6.9 Sensor output profiles for an average bond (a) from the left sensor using a high pass filter with 62 kHz cut-off frequency and (b) from the top sensor using a low pass filter with 1 kHz cut-off frequency. The fundamental frequency is 62.5 kHz.

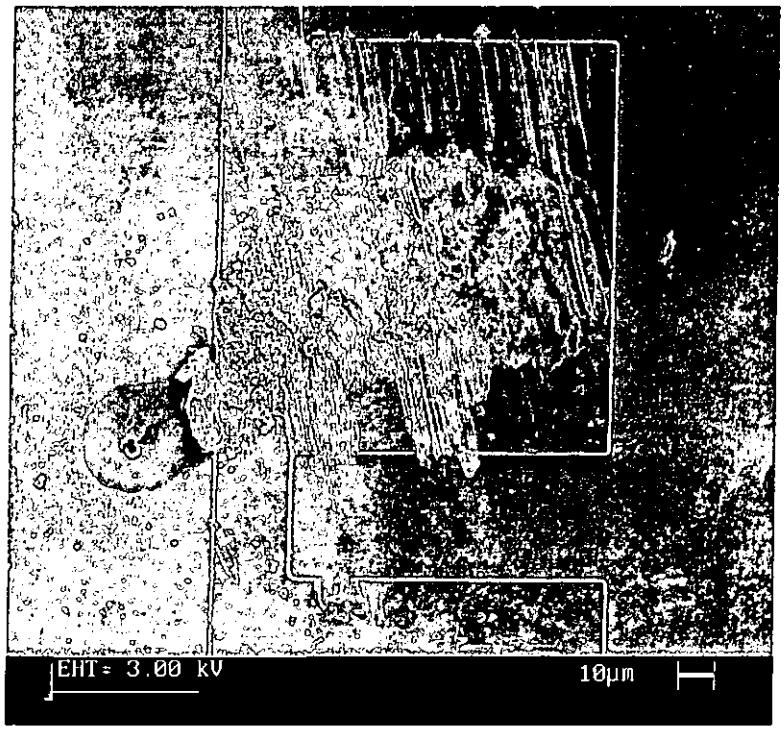

Fig. 6.10 The SEM micrograph of a typical average bond. The shear force is 27 gf.

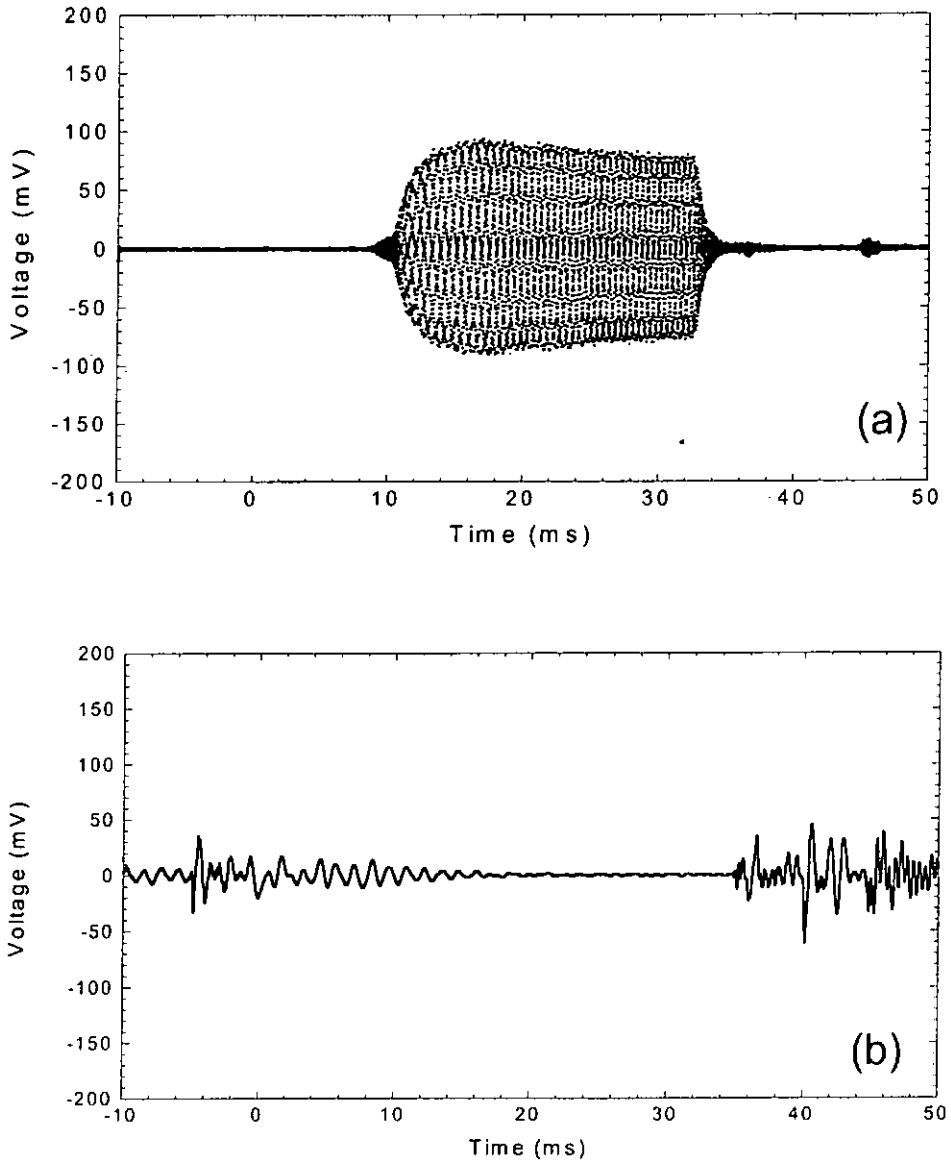

Fig. 6.11 Sensor output profiles for a poor bond (a) from the left sensor using a high pass filter with 62 kHz cut-off frequecy and (b) from the top sensor using a low pass filter with 1 kHz cut-off frequency. The fundamental frequency is 62.5 kHz.

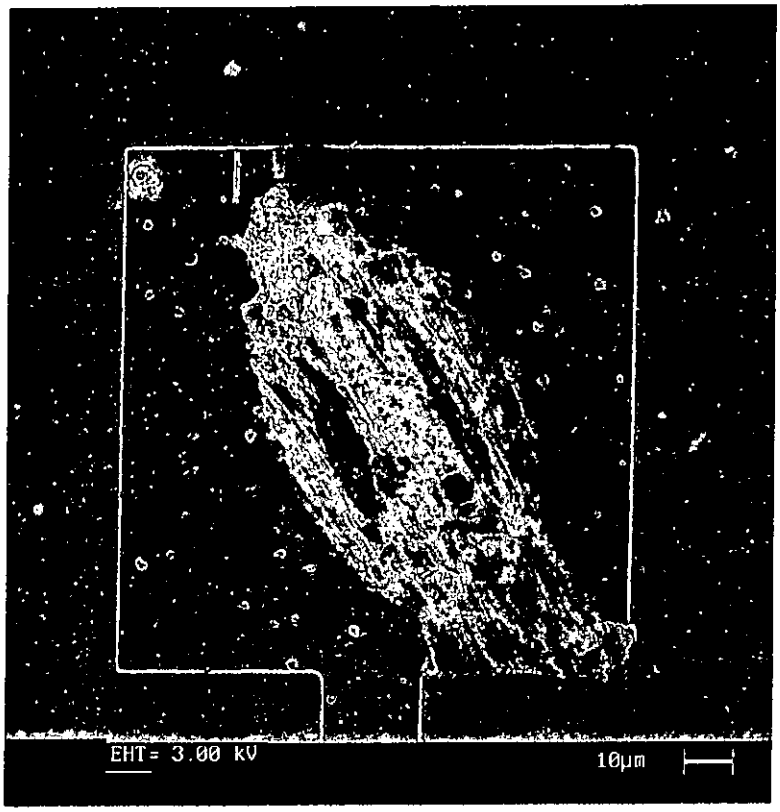

Fig. 6.12 The SEM micrograph of a typical poor bond. The shear force is 16.5 gf.

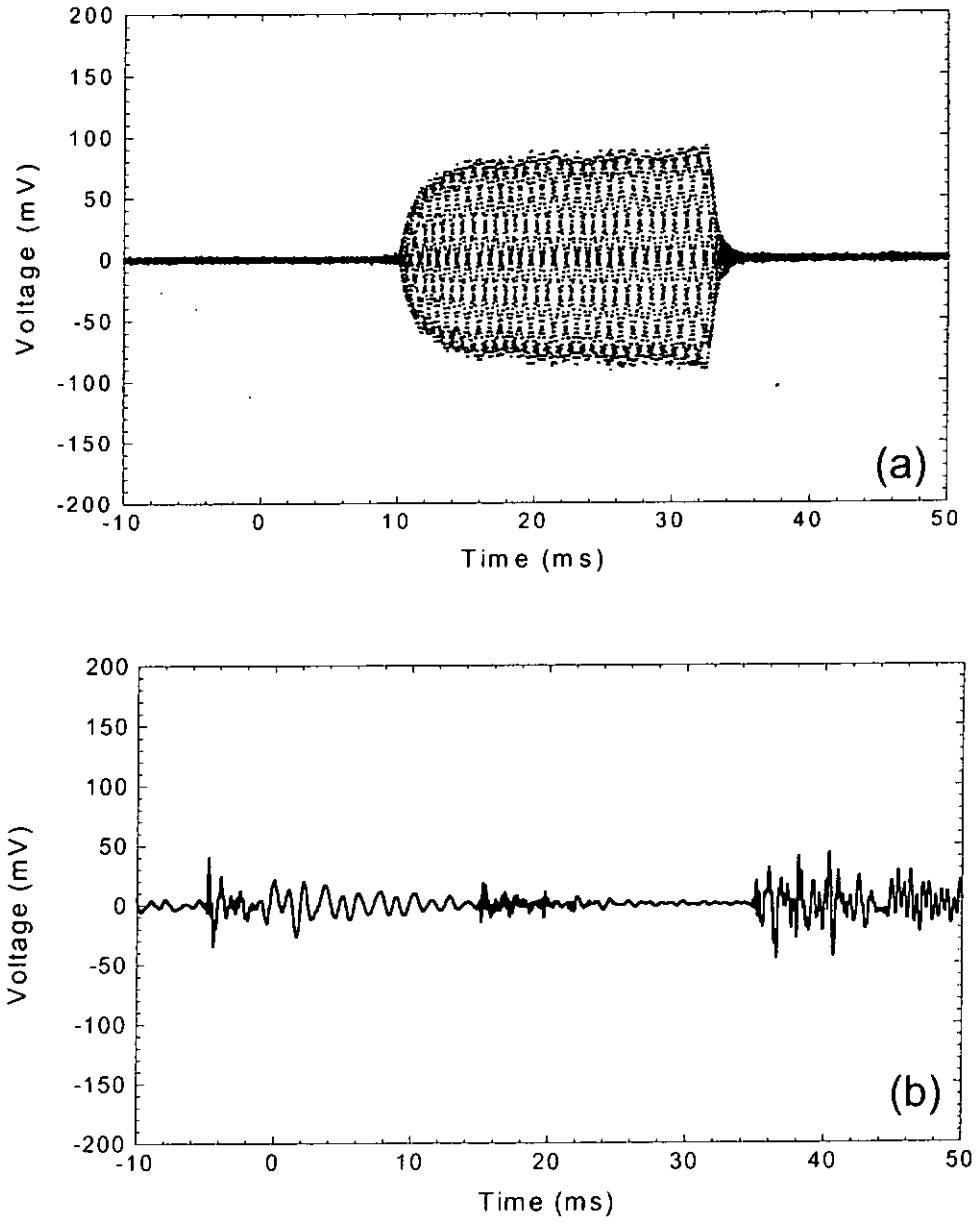

Fig. 6.13 Sensor output profiles for a missing wire bond (a) from the left sensor using a high pass filter with 62 kHz cut-off frequency and (b) from the top sensor using a low pass filter with 1 kHz cut-off frequency. The fundamental frequency is 62.5 kHz.

300 bonds were made under the same bonding conditions (25 ms bonding time , 27 gf bonding force, 3.1 of ultrasonic power setting) to find the relationship between the impact force, shear force and the ratio of ultrasonic amplitude. The result is shown in fig. 6.14. The x, y, z-axis represents shear force, impact force and ratio of ultrasonic amplitude (V_s/V_p), respectively. The solid sphere represents the experimental data in a 3-D plot. Solid square represents the projection of the solid sphere on the 2-D plane (figs. 6.15 & 6.16). It indicates that the shear force has values around 30-40 gf, the impact force is around 50-80 gf and the ratio of ultrasonic amplitude for good bonds (V_s / V_p, see fig. 6.7) is 0.55-0.7, respectively. In addition, it shows the higher the shear force, the lower the V_s / V_p ratio and the lower the impact force.

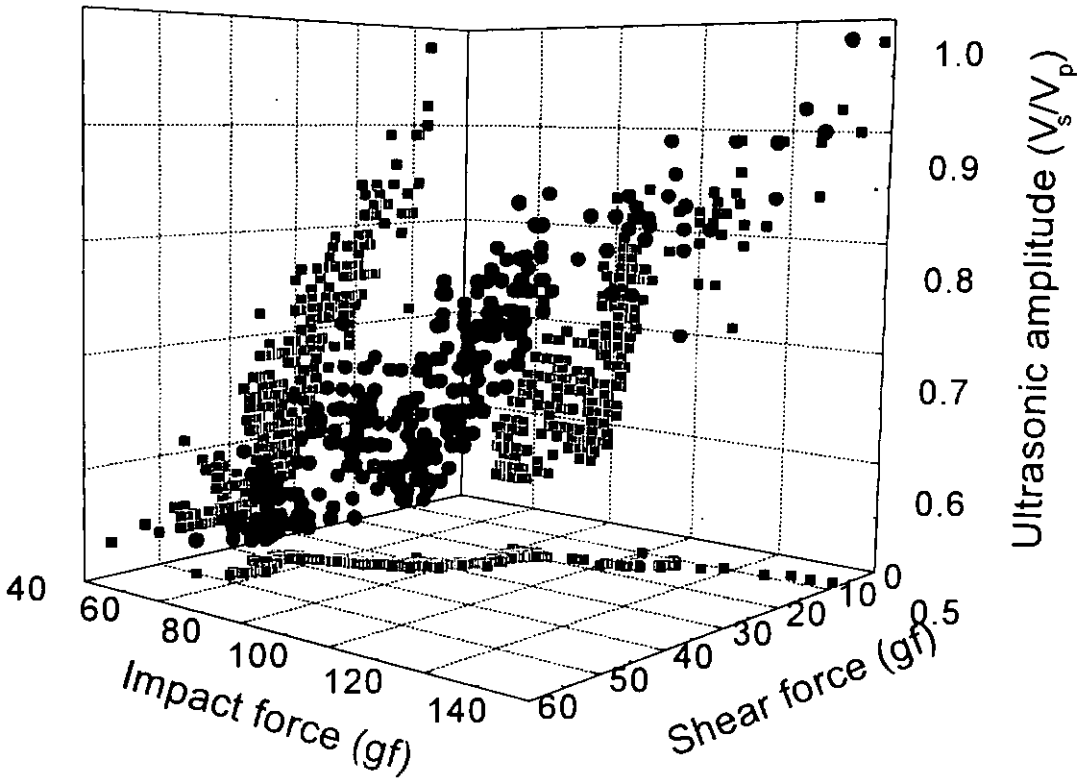

Fig. 6.14 3-D graph of the correlations between the shear force, impact force and the ratio of ultrasonic amplitude. Solid sphere represents the experimental data in each bond. Solid square represents the projections of the solid spheres.

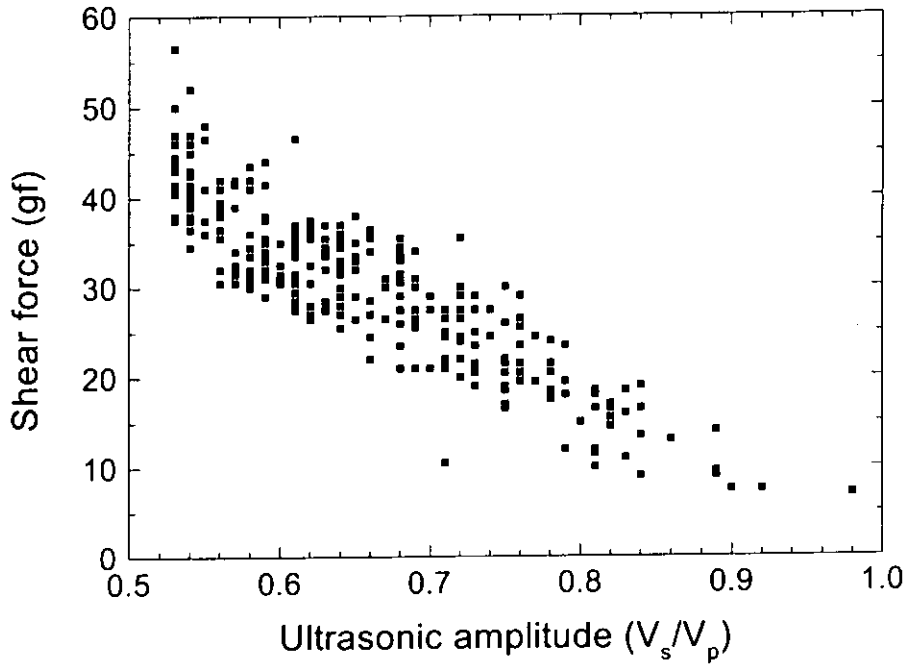

Fig. 6.15 The projection of solid spheres in fig.6.14 on the plane of the shear force (gf) and the ultrasonic amplitude (ratio).

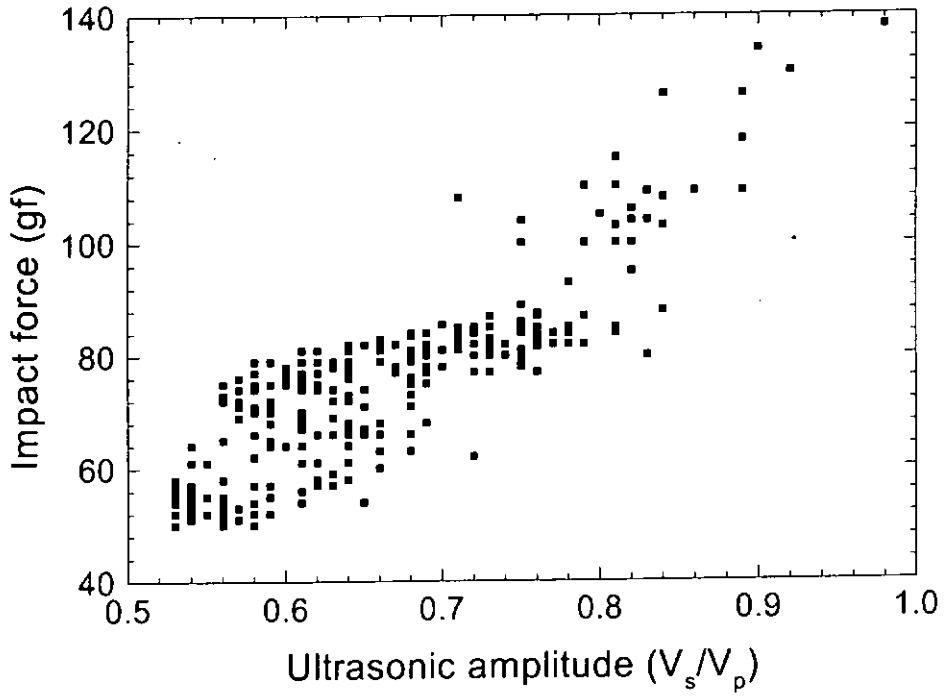

Fig. 6.16 The projection of solid spheres in fig.6.14 on the plane of the impact force (gf) and the ultrasonic amplitude (ratio).

Chapter 7

Conclusion and future development

In this study, an innovative method for monitoring the bonding parameters during the ultrasonic wire bonding process is described. Based on the present work, an US Patent has been filed. The following points are noted:

(1) Choosing PVDF as the sensor materials is better than using PZT ceramics and the 0-3 composite because its insertion does not affect the characteristic of the transducer. It is also easy to fabricate.

(2) The sensor is sandwiched between the piezoelectric driver and the concentrator horn and becomes an integral part of the ultrasonic wedge transducer.

(3) In general, there are two pairs of electrodes in each type of electrode pattern. The top and bottom electrodes are aligned in a direction parallel to the bonding tool. The left and right electrodes are positioned horizontally and are transverse to the bonding tool. The two pairs of electrodes can be used to sense different bonding parameters. The vertical pair is more sensitive to the bonding force as they are more sensitive to the bending moment experienced by

the transducer when the bonding tool contacts the wire to be bonded and the bonding pad. The horizontal pair is more sensitive to the ultrasonic amplitude and the duration of the ultrasonic burst.

(4) A low-pass filter is connected to the top and bottom electrode pair of the sensor and a high-pass filter is connected to the left and right electrode pair of the sensor. The low frequency output signals from the top and bottom sensors represent the mechanical vibrations of the transducer. The high frequency output signals from the left and right sensors represent the ultrasonic amplitudes.

(5) A back-to-back calibration method is used to find the sensitivity of a PZT sensor installed underneath the chip carrier. By comparison, the sensitivity of the PVDF sensor sandwiched between the driver and the horn can be obtained.

(6) Some wire bond testings are proposed that help to evaluate the bond quality. The correlation of sensor output signals and the bond quality could be found. For a good bond, the ratio of ultrasonic amplitude Vs/V_p (see fig. 6.8) of the sensor signals lies between 0.55-0.7. When the ratio is about 0.8, the bond has an averaged strength. When the ratio is above 0.9, the bond has poor strength.

(7) Impact force of the ultrasonic wedge transducer can be obtained during the bonding process using the top and bottom parts of the sensor. The largest value of impact force is obtained when the transducer is operated without a bonding wire.

Suggestions for future work are as follow:

(1) The sensor output signals can be used in real-time monitoring of the bonding process. A computer can be used to store a range of acceptable values for each bonding parameter and the measured bonding parameters are compared with these ranges. When the measured parameters differ from the acceptable ranges, a controlled feedback signal may be generated to bring them back to the required range.

(2) To study different types of electrode patterns or sensor materials that may be used to detect other bonding parameters. For example, pyroelectric materials can be used to sense the change in temperature.

(3) Work is in progress in fabricating a new piezoelectric driver with a sensor incorporated for real-time feedback control, i.e. a smart piezoelectric driver. Details of the work will be reported in the future.

Appendix A

Piezoelectric theory

The piezoelectric effect was discovered by Pierre and Jacques Curie in the 1880's. Piezoelectricity is a property exhibited by certain classes of crystalline materials that lack a center of symmetry. When mechanical pressure is applied to one of these materials, the crystalline structure produces a voltage proportional to the pressure. Conversely, when an electric field is applied to one of these materials, the crystalline structure changes shape, producing dimensional changes in the materials. Piezoelectric properties occur naturally in some single crystal materials and can be induced in other polycrystalline materials.

Some crystalline materials have unit cells that do not have a center of symmetry, and consequently their unit cells contain a small electric dipole. Above the Curie temperature, the crystal structure is a centro-symmetric cubic structure that has no net electric dipole moment and no piezoelectric effect. Below the Curie temperature, the crystal structure changes to a non-centro-symmetric structure and creates a small electric dipole moment.

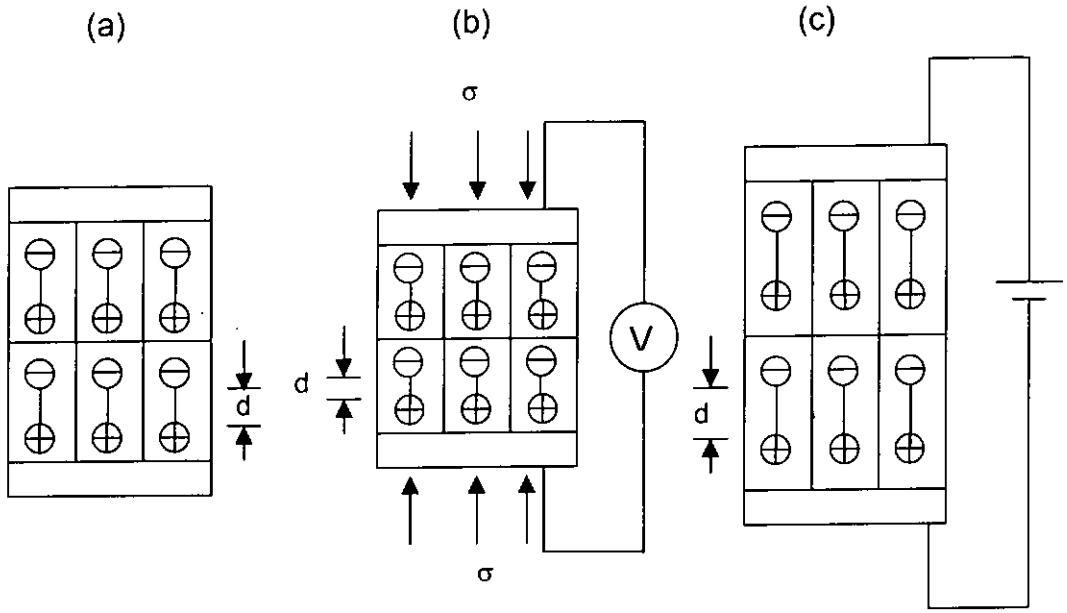

Fig. A.1 (a) Undeformed piezoelectric materials; (b) Compression stresses on material cause a voltage difference and (c) applied electric field across the end of the material causes mechanical deformation. [51]

Fig.A.1 shows the schematic illustration of the piezoelectric effect. A sample of ferroelectric ceramic which has a resultant dipole moment due to the alignment of many small unit dipoles (fig. A.1a). There will be an excess of positive charges at one end and negative charges at the other end in the direction of the polarization. When a compression is applied to the sample, the distance between the unit dipoles (fig. A.1b) is reduced resulting in a reduction in overall dipole moment per unit volume. Thus, the voltage difference between the two electrodes of the sample changes if they are insulated from each other.

If an electrical field is applied across the two electrodes of the sample, the charge density at each end of the sample will be changed (Fig. A.1c) This change in charge density will cause the sample to change its dimensions in the direction of the applied field [51].

Appendix B

Materials properties

B.1 Electromechanical properties of commercial piezoelectric ceramics

The typical electromechanical property values of lead zirconate titanate (PZT) materials [52].

	PZT-4	PZT-5H	PZT-7A	PZT-8
$\varepsilon^T_{33}/\varepsilon_0$	1300	3400	425	1000
tan δ	0.004	0.02	0.025	0.002
k_{33}	0.675	0.75	0.670	0.640
k_t	0.57	0.5	0.52	0.51
d_{33} ($\times 10^{-12}$ m/V)	315	593	153	225
g_{33} ($\times 10^{-3}$ Vm/N)	24.6	19.7	41	25.4
s^E_{33} ($\times 10^{-12}$ m^2/N)	12.3	16.5	10.7	11.5
s^D_{33} ($\times 10^{-12}$ m^2/N)	7.9	8.99	7.9	8.5
C^D_{33} (G Pa)	159	157	175	161
υ^D_{33}(m/s)	4600	4560	4800	4600
N_{3t}(Hz m)	2000	2000	2100	2070
ρ (kg/m^3)	7500	7500	7700	7600

Table B1. Typical properties values of lead zirconate titanate (PZT) materials

B2 Mechanical properties of metals

The mechanical properties of metals are shown in table B2.

	347 stainless steel	6061T6 Aluminum alloy	7075T6 Aluminum alloy	Tungsten Carbide
Young' Modulus E (G Pa)	196	70.0	72.8	534
Density ρ (kg/cm^3)	7910	2700	2800	13800
Longitudinal Wave Velocity (m/s)	5000	5092	5099	6240
Poisson's ratio ν	0.300	0.355	0.355	0.220
Shear Modulus S (G Pa)	75.7	26.0	27.0	219

Table B2. The mechanical properties of metallic materials.

B3. Sensor materials

Typical piezoelectric materials parameters of the PZT ceramic, PVDF and PZT/P(VDF-TrFE) composites (with 0.5 volume fraction of ceramics) are given in the following table.

	PZT	PVDF	PZT/P(VDF-TrFE)
Piezoelectric constant d_{33} (pC/N)	420	18	23
Electromechanical coupling coefficient k_t	0.5	0.24	0.08
Density ρ (kg/m^3)	7500	1780	5240
Relative permittivity $\varepsilon^T_{33}/\varepsilon_0$	3250	20	120

Table B3 Properties of sensor materials.

References

[1] L. A. A. Warnes, *Electronic materials,* Basingstoke, Hampshire Macmillan, pp. 292 (1990)

[2] Operation manual of AB-500B computerized semi-automatic aluminum wire wedge bonder, ASM Assembly Automation Ltd., Hong Kong (1995)

[3] G. Harman., *Wire bonding in microelectronic materials, processes, reliability and yield.* McGraw-Hill, New York, pp. 290 (1997)

[4] F. Farassat, 'Wire bonding process control'. *Semiconductor fabtech*, pp. 319-324 (1998)

[5] H. A. Schafft, "Testing and fabrication of wire-bond electrical connections — A comprehensive survey". *National Bureau of standards (NIST) Tech.* Note 72+6, pp. 1-129 (1972)

[6] R. Rodwell; D. A. Worrall, "Quality control in ultrasonic wire bonding". *Hybrid circuits*, no.7 pp. 67-71 (1985)

[7] MIL-STD-883B, " *Test methods and procedures for microelectronics, Method 2001.1, Bond strength*", Department of Defense, Washington DC, 1977.

[8] BS 9450:1975, " *Specification for custom-built integrated circuits of assessed quality: Generic data and methods of test*". British Standards Institution, London, (1975)

[9] L. G. Wright, "Impedance measuring network". *US Patent 3636456* (1972)

[10] O.E. Gibson, W. J. Gleeson, L. D Burkholder,. and B. K. Benton, " Bond signature analyzer". *US Patent 4998664*, (1991)

[11] L. Ingle, and J. Koontz, "Directly bonded interconnect method and adaptive feedback bond signature analysis system". *Proceeding 1993 international conference on multichip modules*, pp. 384-390 (1993)

[12] J. Jensen, and D.Bradner, "Monitoring ultrasonic wire bonders with a dynamic signal analyzer". *Solid state technology*, Vol. 33, pp. 53-55, 1990.

[13] T. E. Salzer, and C. T.Martin, "Monitoring and control means for evaluating the performance of vibratory-type devices". *US Patent 3794236* (1974)

[14] T. E. Salzer, "Method and apparatus for ultrasonic bonding". *US Patent 4373653* (1983)

[15] P. M. Uthe, "Method and apparatus for ultrasonic weld quality analysis employing plural analysis signals". *US Patent 3693158* (1972)

[16] P. M. Uthe, "Ultrasonic wire bonding quality monitor and method". *US Patent 4815001* (1989)

[17] M. McBrearty, M. Negin; A, Zielenski; M. Weilerstein.,, " Real time non-destructive evaluation in ultrasonic wire bonder". *Proceedings IEEE ultrasonic symposium*, Vol. 2, pp. 861-865 (1983)

[18] M. McBrearty, M. Negin, A. Zielenski and M. Weilerstein " Apparatus for detecting missing wires". *US Patent 4558596* (1985)

[19] J. L. Landes, "Ultrasonic bond energy monitor". *US Patent 4341574*, (1982)

[20] M. J. Hight, R. V. Winkle and J. R. Dale, " Ultrasonic bonding apparatus". *US Patent 4040558* (1977)

[21] K. Ulrich von Raben, "Monitoring bond parameters during the bonding process". *US Patent 4854494* (1987)

[22] K. Ulrich von Raben., "Controlling relevant bonding parameters of modern bonders". *Proceedings of the 38th electronics components conference 1988*, pp. 558-563 (1988.)

[23] K. Ulrich von Raben, "Apparatus for measuring bonding parameters". *US Patent 4806193* (1989)

[24] R.Pufall. "Automatic process control of wire bonding". *Proceedings 43rd Electronic components and technology conference*, pp. 159-162 (1993)

[25] P.Langevin, *British Patent 145691* (1921)

[26] J. Blitz, *Ultrasonics methods and applications*, Butterworths, London, (1971)

[27] T.F.Hueter, R. H. Bolt, *Sonics*, techniques for the use of sound and ultrasound in engineering and science. Wiley, New York, pp. 456 (1955)

[28] *Guide to dynamic measurements of piezoelectric ceramics with high electromechanical coupling*, International electromechanical commission (IEC) standard 483 (1976)

[29] S. Lin; F. Zhang, "Study of vibrational characteristics for piezoelectric sandwich ultrasonic transducers". *Ultrasonics*, Vol. 32, no. 1, pp. 39-42 (1994)

[30] S. Lin, " Study on the multifrequency Langevin ultrasonic transducer". *Ultrasonics*, Vol. 33, no.6, pp. 445-448 (1995)

[31] S. Lin, "Sandwiched piezoelectric ultrasonic transducers of longitudinal – torsional compound vibrational modes". *IEEE transactions on ultrasonic, ferroelectrics, and frequency control*, Vol. 44, no. 6, pp. 1189-1197 (1997)

[32] B. Athikom, K. Hari, R. D. Ponnekanti, " Optimizing the performance of piezoelectric drivers that use stepped horn". *Journal of acoustical society of america*, Vol. 90, no. 3, pp. 1223-1229 (1991)

[33] Z. Yan, Z. Lin, "Optimum design for sandwich transducer – by analyzing effects of structure and materials parameters of transducer on its performance". *Acta acustica*, Vol. 20, no. 1, pp. 18-25 (1995)

[34] K. Graff, *Wave motion in elastic solids*, Oxford university press, London, (1975)

[35] S. W. Or, "*Performance study of the ultrasonic wire bonder used in microelectronic packaging*". MPhil. thesis, The Hong Kong Polytechnic University, Hong Kong (1997)

[36] W. D. Callister, Jr, *An introduction Materials science and engineering*, John Wiley & Sons, Inc, New York, pp. 811 (1994)

[37] D. R. Askeland, *The science and engineering of materials,* Chapman & Hall, London, pp.880 (1993)

[38] T. Ikeda, *Fundamentals of piezoelectricity*, Oxford, New York, pp. 263 (1990)

[39] H. Kawai, "The piezoelectricity of poly (vinylidene fluoride)". *Japanese Journal of applied physics*, Vol. 8, pp. 975-976 (1969)

[40] P. K. L. Ng, "Lead zirconate titanate (PZT) / piezoelectric copolymer P(VDF-TrFE) composites". MPhil. thesis, The Hong Kong Polytechnic University, Hong Kong (1998)

[41] Vibration transducer calibration system—Type 9610, Brüel & Kjær.

[42]. C. L. Nachtigal, *Instrumentation and control fundamentals and applications*, John Wiley & Sons, Inc., New York, pp. 890 (1990)

[43] S. S. Chiu, H. L. W. Chan, S. W. Or, Y. M. Cheung, C. H. Yuen, P. C. K. Liu, " Sensor for ultrasonic wire bonding process control", to be published in *Ferroelectrics*

[44] *F 459 Standard test methods for measuring pull strength of microelectronic wire bonds*, Annual book of ASTM standards, Vol. 10.04, pp175-177 (1995)

[45] G. G. Harman; C. A. Cannon, "The microelectronic wire bond pull test – How to use it, How to abuse it". *IEEE transactions on components,*

hybrids, and manufacturing technology, Vol. 1, no.3, pp. 203-210 (1978)

[46] P. Lall; D. Barker; M.I Pecht., "Development of an alternative wire bond test technique". *1992 IEEE/CHMT international electronics manufacturing technology symposium*, pp. 283-287 (1992)

[47] S. Prasad; A. Saboui., "An improve wire bond pull test". *Solid state technology*, pp 39-41 (1991)

[48] F 1269 Test methods for destructive shear testing of ball bonds, Annual book of ASTM standards, Vol. 10.04, pp.406-413 (1995)

[49] W. Shimada, T. Kondo, H. Sakane, T. Banjo, K. Nakagawa, " Thermo-compression bonding of Au-Al system in semiconductor IC assembly process", *Proceeding international conference on soldering, brazing and welding in electronics*, pp. 127-132 (1976)

[50] S. W. Or, H. L. W. Chan, V. C. Lo, C. W. Yuen, "Ultrasonic wire bond quality monitoring using piezoelectric sensor", *Sensors and actuators A Physics*, Vol. 65, pp. 69-75 (1998)

[51] L. H. Van, *Elements of materials science and engineering*, Addison-Wesley, pp. 598 (1989)

[52] Piezoelectric ceramics data book for designers, Morgan Matroc Ltd., U.S.A., pp. 26.

List of publications

[1] S. S. Chiu, H. L. W. Chan, S. W. Or, Y. M. Cheung, C. W. Yuen, P. C. K. Liu, " Sensor for ultrasonic wire bonding process control", *Ferroelectrics*, Vol. 232, pp. 211-216 (1999).

[2] H. L. W. Chan, S. S. Chiu, S. W. Or, Y. M. Cheung, "Piezoelectric sensor for measuring bonding parameters", *United State Patent* pending.

[3] H. L. W. Chan, S. S. Chiu, S. W. Or, Y. M. Cheung, P. C. K. Liu, "Piezoelectric sensor for measuring bonding parameters", to be submitted to *IEEE Transactions on Ultrasonic, Ferroelectrics and Frequency Control.*

[4] S. S. Chiu, H. L. W. Chan, S. W. Or, Y. M. Cheung, C. W. Yuen, P. C. K. Liu, " Effect of electrode pattern on output from sensor for wire bonding process control", to be submitted *Ferroelectrics*.